The Effect of High Altitude Environments on the Damage Structure Evolution during Fatigue Fracture of Legacy Aerospace Aluminum Alloy 7075-T651

A Dissertation

Presented to:

The Faculty of the School of engineering and Applied Science

University of Virginia

In Partial Fulfillment

Of the Requirements for the Degree of

Doctor of Philosophy in Materials Science and Engineering

Prepared by:

Adam W. Thompson

May 2022

APPROVAL SHEET

This

Dissertation

is submitted in partial fulfillment of the requirements for the degree of

Doctor of Philosophy in Materials Science and Engineering

Author: Adam W. Thompson

This Dissertation has been read and approved by the examining committee

Advisor: Dr. James T. Burns

Committee Chair: Dr. James M. Fitz-Gerald

Committee Member: Dr. Sean R. Agnew

Committee Member: Dr. Robert G. Kelly

Committee Member: Dr. Devin K. Harris

Accepted for the School of Engineering and Applied Science

Jennifer L. West, School of Engineering and Applied Science

May 2022

Summary

Many aircraft structural components are frequently made from 7xxx series aluminum alloys (Al-Zn-Mg-Cu), which can suffer from fatigue. It has been reported that 80% of flight times were spent at a "cruising altitude" (above 30,000 ft), where 17% of significant load peaks occurred and 42% of such significant events occur at "high altitude" (above 10,000 ft). Orders of magnitude reduction in the fatigue crack growth rates (da/dN) occur during fatigue testing in high altitude environments (e.g. low temperature and low partial pressure of water vapor (P_{H2O})) pertinent to high altitude flight. Critically, despite a constant exposure parameter (P_{H2O}/frequency), differences in da/dN are observed between tests at 23°C and low temperature environments (below -30°C). Several hypotheses have been proposed to explain the apparent temperature dependence: surface reaction rates between the water vapor and aluminum, hydrogen diffusion, hydrogen-dislocation interaction, and dislocation or damage structure evolution. Each of these hypotheses will be examined in turn. It is also necessary to evaluate the efficacy of current testing protocols on rigorously capturing environmental crack growth data, including the existence of the threshold transition regime (TTR).

To address these knowledge gaps the following approaches were employed. An evaluation of alternate testing protocols in an attempt to avoid the complicating TTR behavior. Use of various testing protocols to develop a more complete mechanistic understanding of the temperature dependent fatigue behavior of AA7075-T651 despite a constant exposure parameter (P_{H2O}/f). The development of a systematic and multi-scale set of characterization techniques (EBSD, HR-EBSD, FIB, TEM, and PED) to evaluate the local crack wake damage structure to gain insights into the high altitude environmental cracking processes.

The results indicate low temperatures found in high altitude environments have a strong influence on the fatigue behavior. Not only does temperature influence the driving force threshold for the transition from a slip band cracking (SBC) mechanism to a flat transgranular cracking mechanism, but also lessens the impact water has on the fatigue behavior, insinuating low water vapor levels may not need to be taken into consideration for aerospace applications in high altitude environments. Furthermore, the multi-length scale characterization protocol revealed the majority of the fatigue damage structure was localized to the first ≈ 500 nm of depth from the crack wake surface, which the development of said structure has a similar appearance to Beilby layers. The

definition of the layer lessened with a decrease in driving force and temperature. The presence of hydrogen appeared to cause an elimination of high dislocation density and precipitates within the layer, but again lessened with smaller driving forces. Additionally, the presence of hydrogen precipitated the first ≈ 100 nm of depth to form a recrystallization layer, appearing at both high and low driving forces, but was unable to form at low temperatures. The TTR event observed with fatigue cracking of AA7075-T651 in low water environments was determined to be an intrinsic response which cannot be eliminated by a reduction of sample thickness or a change in the loading protocol.

Table of Contents

Table of Figures

the same P_{H2O}/f. The subsequent crack growth rate was recorded for each segment and the reported value was plotted to determine the relative difference between the data points.

List of Tables

Chapter 1 – Introduction to the High Altitude Fatigue Problem

1.1. Introduction

For the aerospace industry, both commercial and military, aluminum has been an important structural material in the development of weight-efficient, high performance airframes since the 1930s.[1] Aluminum is used in larger quantities when compared to other major aerospace materials such as magnesium, titanium, steel and composites.[1] It is estimated that 60 to 80% of the airframe weight on commercial aircraft and 40 to 60% on military aircraft are aluminum alloys. Despite the growing use of alternate materials, aluminum alloys are likely to remain an important structural material due to their moderate cost, ease of fabrication, high strength to weight ratio, ductility, fracture toughness and the range of material properties available by mechanical and thermal treatments.[1] There are many types of aluminum alloys used by the aerospace industry, although aircraft structural components are often made with the 7xxx series alloys (Al-Zn-Mg-Cu).[1] Conventional 7xxx series alloys generally have higher strength than other aluminum alloys, making them better for structures carrying heavier loads such as upper wing surfaces, spars, stringers, pressure bulkheads, and fuselage frames.[1] While these systems have better strength properties, they still suffer from fatigue, which is the primary failure mode for aerospace applications.[1–3]

It is estimated that fatigue causes over half of all metal component failures and is responsible for more damage than the combined effects of corrosion, creep, wear, overloading and all other failure sources to aircraft.[1] Unlike other failure mechanisms fatigue occurs in components that are subjected to repeated fluctuating loads that do not exceed the magnitude required for yield or fracture under normal monotonic loading conditions.[7] These repeated fluctuations or load cycles cause cumulative plastic damage around regions of stress (strain) raisers where the local stresses are elevated. This cumulative damage will cause the initiation and subsequent propagation of a crack or cracks into the regions of plastic damage accumulation.[7] The total number of cycles to failure or total fatigue life of a component is composed of two processes: fatigue crack initiation life, which is the number of load cycles required to initiate a fatigue crack, and fatigue crack propagation life, which is the number of load cycles required to propagate a critical crack size to cause failure to occur in the component. Understanding the fatigue life of components is a critical safety issue which pushed the development and introduction of the damage tolerance criterion.

This life management paradigm exploits the capability of an aircraft component to contain cracks and other damage below a critical size without suffering catastrophic failure.[1] The United States Air Force pioneered the damage tolerant design philosophy which required the acceptance of cracks in the aircraft and planned to manage them by the combination of design and inspection.[1] Today, many aircraft components such as fixed leading edges, fuselage skins, fuselage frames, fuselage stringers, upper and lower spars, upper and lower wing skins and stringers, and both upper and lower horizontal stabilizers are all required to factor in fatigue into the design requirements. Despite these efforts, recent teardowns of airframe structures have found that fatigue is still the primary failure mechanism in structural components.[1,8,9]

1.1.1. Reported Fatigue Data

The "safe-life" paradigm of fatigue management is a traditional approach that is still applied today by some airframe structural management communities. This empirically based approach uses the results from the laboratory testing which subject smooth or notched specimens to repeated sinusoidal fluctuating loads to generate stress (or strain) amplitude versus the number of cycles to failure, which are known as S-N curves.[10] The main issue with S-N curves is obtaining total fatigue life behavior using small laboratory specimens complicates the use of the results to predict the behavior of actual engineered components that have different sizes, shapes, and surface finishes.[7,10] Furthermore, the total life data does not delineate between the initiation and propagation phases of fatigue damage progression. Additionally, S-N curves neglect to give insights into the physical phenomena and mechanisms that govern the fatigue process.[10] To gain a better understanding of the fatigue phenomenon studies generally focus their experiments on fatigue crack initiation or fatigue crack propagation processes separately.[10]

Understanding the mechanisms that govern a materials resistance is a high priority the fatigue community. Initiation is known to be strongly dependent on a complex interaction of surface roughness, residual stress, environment, and local microstructure. Due to this complexity, the size scale of the initiation process, and the inherent variability of these factors for an engineering component, engineering prognosis approaches generally focus on modeling and predicting crack growth rather than initiation.[3] For example, damage tolerant approaches to fatigue life management of aircraft components (e.g. fuselage skins, upper and lower spars, upper and lower

wing skins as well as upper stringers and both upper and lower horizontal stabilizers) all are based on the fracture mechanics-based predictions of crack propagation.[1]

1.1.2. Fatigue Crack Propagation

Fatigue crack propagation is generally characterized using a linear elastic fracture mechanics approach, which uses the concept of similitude. Specifically the crack tip driving force is described by a loading parameter known as the stress intensity range (ΔK); the development of this approach applied several assumptions the most relevant being that there is only small scale yield local to the crack tip with the rest of the component remaining elastic.[10–12] Fatigue propagation data is most commonly presented in a log-log plot of the rate of fatigue crack growth per cycle of load fluctuation, da/dN, and the change in ΔK which typically plot a characteristic sigmoidal shape. Much work has been done looking at relevant microstructure and loading conditions impacting fatigue for 7xxx series aluminum alloys.[13–22]

1.1.3. Microstructure

7xxx series aluminum alloys are a precipitate hardened alloy, where the strengthening precipitates, which start from a super saturated matrix material and precipitate out as an agglomerate of solute atoms known as Guinier-Preston (GP) zones, grow naturally or artificially (heat solution treatment) to coherent, soluble metastable precipitates typically 1 to 5 nm in diameter.[23] Other second phase particles relevant to the mechanical and electrochemical properties of the alloys are dispersoids and constituent particles. Dispersoids are generally semi-coherent and form during solidification or ingot preheats and typically are less than 1 μm in diameter with little to no solubility in the matrix aluminum alloy.[23] Constituents are generally incoherent and are insoluble intermetallic particles, which are mostly composed of impurities elements forming during the solidification process to sizes ranging from 1 to 30 μm.[23] The exact chemistries of these 2nd phase particles are dependent on the elements which make up the alloys.[23] The compositions for AA7075 can be found in Table 1. As shown previously the microstructural features have been shown to influence fatigue where the major factors to considered for the relationship between microstructure and fatigue crack propagation are: slip character, slip length, crack path and crack extension forces, morphology and properties of constituents in multiphase alloys and environment.[22]

Table 1 - Typical elemental composition for the aluminum alloy 7075-T651 used for this study. "m" denotes the maximum amount of these elements that can be in the alloy.

Zn	Mg	Cu	Cr	Fe	Si	Al
5.60%	2.50%	1.60%	0.23%	0.40%[m]	0.40%[m]	Balance

1.1.4. Microstructural factors on fatigue behavior

Generally, the microstructural influence on fatigue can be summarized by its impact on slip reversibility (slip character and length) or its tendency to induce extrinsic toughening mechanisms (crack path, crack extension forces and morphology) creating such things as a tortuous path for crack extension and/or crack closure.[22,24] Slip character is often characterized as wavy or planar; AA7075-T651 exhibits wavy slip typically because of its high stacking fault energy and the non-shearable nature of the precipitates formed in the material. Wavy slip is considered to be the closest approximation to homogeneous deformation as the slip is not localized to specific crystallographic planes making slip reversibility more difficult due to debris forming processes like cross-slip.[22,25] Grain boundaries are also an obstacle to slip as smaller grain sizes create more obstacles for dislocation movement, thus decreasing the slip reversibility resulting in an increased dislocation density and an increase in the fatigue crack growth rates.[26] These obstacles to slip reversibility such as dislocation debris, grain boundaries and precipitates lead to a reduction in slip length, which gives rise to the most pronounced effects on fatigue crack growth rates especially in the near-threshold regime.[22,25,27] The importance of these obstacles can be seen in a study by Charkrabortty, which suggests the plastic strain ahead of a crack tip does not decrease monotonically with distance from the crack tip like LEFM predicts, but instead would be more uniform within a zone that is dependent on microstructure, which for most materials the zone would be the equivalent to the distance between major deformation barriers.[28] This model consequently predicts an increase in fatigue crack propagation resistance as the slip length increases as each deformation zone would decrease as slip length increases.[28] Similarly, the work of Davidson and Lankford concluded that dispersoids, more specifically the mean free path of slip through the dispersoids was the microstructural element of most importance to the growth rate of fatigue in AA7075-T651.[29] However, dispersoid particles have a primary role to control grain

growth and prevent recrystallization from occurring in the material, which means the impact from dispersoids are more likely to be closely related to the grain size.[29,30] Additionally, a study done by Bucci et al. found on average over aging materials decreased the fatigue crack growth rate by a factor of two at the intermediate or Paris regime ΔK values, but in the low or near threshold region ΔK values there was a ten times increase in fatigue crack growth rates.[30] Using slip length alone as a predictor of fatigue propagation behavior parameters like ΔK_{th} has its controversies as a review done by Starke and Williams showed literature at the time came to several different conclusions and some of these conclusions directly contradicted each other despite the researchers using similar testing and materials for the experiments performed.[22]

Another important factor on fatigue behavior is the extrinsic mechanisms which affect the crack path, where geometric mechanisms such as crack deflection can be observed on the fractured surface created by the propagating crack where striations can appear.[31,32] The density of the striations depends on the crack growth rate of the propagating crack controlled by the degree of strain localization, where homogeneous deformation creates a relatively flat and straight crack resulting in higher crack growth rates and non-homogeneous deformation create a facet or crystallographic style crack resulting in slower crack growth rates.[33] Crack deflection causes lower crack growth rates to occur despite being subjected to the same effective stress intensity (assuming effective stress intensity fails to take the deflection of the crack into account) because of the mixed mode displacement resulting in the fractured surfaces making premature contact, known as roughness induced closure, which effectively reduces the effective stress intensity.[34,35] Roughness is not the only cause of closure, crack wake oxides and plasticity in the crack wake can also induce closure.[32]

It has been postulated that local to a fatigue crack tip the strain is significantly high enough to alter the crack path via strain induced dynamic recrystallization and strain induced dissolution of strengthening precipitates at ambient temperatures.[36] The study done by Bai et al., reported a decrease in Cu-Mg co-clusters (the strengthening precipitates in this aluminum alloy used in the study) near the crack tip after cyclic deformation occurred, which the authors concluded was due to repeated shearing of dislocations emanating from the crack tip disrupting the co-clusters leading to a partial dissolution to smaller sizes than what is required for precipitate nucleation to occur.[36] This causes the remains of the precipitate to diffuse back into the matrix material leaving behind

nano-scaled, and highly misoriented grains separated by high-angle boundaries attributed to the dynamic recrystallization process.[36] Other studies demonstrate heavy plastic deformation can refine grains to the sub-micrometer or nanometer scale in metals and alloys causing a deformed surface layer which contains ultra-fine grains, known as "Beilby layers".[37,38] These Beilby layers are commonly found on the surface of mechanically polished metals formed by the high levels of plastic strain occurring at these surfaces.[37,38] Additionally, constituent particles can impact crack path but are generally thought to have more impact on fatigue crack initiation than propagation, due to the fact they occupy a low volume fraction of the material, their incoherency with the matrix material and brittle nature.[13,39–41] Where constituent particles potentially effect fatigue propagation is in the unstable crack growth regime or high ΔK values where it has been experimentally shown that increasing the volume fraction of constituent particles will decrease the toughness of the material effectively lowering the K_{IC} value.[42] Few studies have looked specifically at constituent particles and their role in the fatigue propagation process overall, but studies that did report crack propagation deviates toward and grows through constituent particles that appeared to be cracked or debonded from the aluminum matrix effectively speeding up the crack growth rates.[43,44] As stated previously constituent particles occupy a low volume fraction of the material and therefore are unlikely to have a significant impact on fatigue propagation. While microstructural effects are important studies have shown the environmental factors can often dominate and/or alter the other factors which impact fatigue.[45–48]

1.1.5. Environmental impact on fatigue behavior

It is well known that the fatigue crack growth behavior of aluminum is affected by the loading environment, particularly for the near-threshold region and Paris regime of fatigue. Many studies have shown fatigue testing done on aluminum alloys under vacuum, or dry air (extremely low amounts of water vapor), have resulted in significantly slower crack growth rates than the growth rates in moist or corrosive environments,[5,29,49–56] as well as impacting the fracture morpohology.[5,52,53,57] Various mechanisms such as adsorption, chemisorption, hydrogen embrittlement and rewelding of the fractured surfaces due to the degree of friction have all been proposed as the cause of the changes observed.[52,53,58,59] It is generally agreed the results observed from fatigue cracking of aluminum alloys in a corrosive environment are most consistent with a hydrogen embrittlement mechanism for fatigue. However, such effects are not exclusive to

corrosive environments as this phenomena has also been observed environments with a non-negligible water content.[22,45,48,59–65] Commonly, the severity of the moist environment is described using the exposure parameter, P_{H2O}/f, which quantifies the product of water vapor pressure and the time available for surface reaction.[48,62] The hydrogen embrittlement process starts with the mass transport of water vapor to the crack tip, where it is postulated that the reaction of water vapor with the fresh aluminum surfaces at the crack tip produce atomic hydrogen enabling the hydrogen-assisted cracking of aluminum alloys.[48] The reactions required for this are shown in equation [1], where X is the degree of hydration and equation [2][66]:

$$2Al_{(s)} + (3 + X)H_2O_{(g)} \rightarrow Al_2O_3 + X(H_2O)_{(s)} + 3H_{2(g)} \qquad [1]$$

$$H_2O + e^- \rightarrow (OH)^- + H \qquad [2]$$
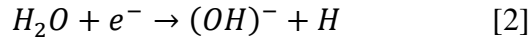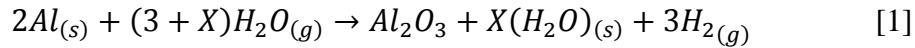
The overall reaction of equation [1] shows the production of hydrogen gas, but an intermediate step is the formation of atomic H with can either be adsorbed or can recombine to form H_2 gas.[66] The reaction in equation [2] must occur three times in order to support aluminum oxidation to Al(III), as indicated in equation [1].[66] It is this atomic hydrogen that is adsorbed into the aluminum alloy where it will diffuse between interstitial lattice sites, but can get trapped in other lower potential energy sites such as solute atom clusters, free surfaces, sites between the first few atomic layers beneath the surface, mono-vacancies and vacancy clusters, dislocation cores, strain fields, grain boundaries, precipitate/matrix interfaces, strain fields around a precipitate, inclusion/matrix interfaces, voids, and internal cracks.[67] Typically this hydrogen will diffuse and concentrate ahead of notches and cracks due to the hydrostatic stresses that will cause an expansion of the crystal lattice.[67] Hydrogen will diffuse at a given rate, which depends primarily on the crystal structure and complexity of the microstructure through the crystal lattice in response to gradients in hydrogen concentration, temperature, and hydrostatic stress fields. However, hydrogen occupying dislocation cores or other trap sites caused by dislocations can be transported faster by mobile dislocations than lattice diffusion.[67] Exactly what the mechanisms are for hydrogen embrittlement in aluminum alloys are still debated as a number of mechanisms have been proposed; a consensus is building around a primary and interacting role of HEDE and HELP.

1) **Hydrogen-Enhanced Decohesion (HEDE):** This mechanism involves a charge transfer weakening the interatomic bonds of the alloy allowing for separation or decohesion of the atoms to occur in preference to slip when a critical crack-tip opening displacement is

7

achieved.[67] Decohesion events can occur at crack tips with adsorbed atomic hydrogen, where dislocation-shielding effects result in a tensile stress maximum or where there areas of maximum hydrostatic stress and particle-matrix interfaces ahead of the crack tip.[67] Evidence for this mechanism is difficult to obtain directly but it is believed, citing the fact that field-ion microscopy using hydrogen gas makes field evaporation easier as direct evidence that hydrogen weakens interatomic bonds of surface atoms giving credence to the HEDE mechanism. Additionally, transmission electron microscopy (TEM) analysis of brittle intergranular fracture showed evidence of segregated impurities at the grain boundaries and atomistic calculations have shown impurities like hydrogen can weaken interatomic bonds, thus hydrogen segregated to grain boundaries or other interfaces could result in decohesion.[67,68]

2) **Hydrogen-Enhanced Localized Plasticity (HELP):** This mechanism involves solute hydrogen facilitating dislocation activity via a hydrogen "shielding" concept where dislocations are shielded from the full force of repulsive interactions between dislocations and obstacles due to hydrogen being segregated to the stress fields of dislocations as well as other elastic obstacles.[67,69] The stress field associated with the defect must be modified increasing the stress field in some directions, while decreasing stress fields in other directions consequently decreasing the interaction energy of the dislocation with obstacles that would impeded its motion effectively allowing dislocations with hydrogen attached to move at lower stress levels than what would be normally required in certain directions as well as decreasing the equilibrium separation distance.[67,69] Dragging hydrogen with the dislocation naturally limits the dislocation's ability to cross-slip and increases slip planarity within the material.[67,69] Evidence for support of this mechanism have been directly observed via *in-situ* TEM experiments where upon the introduction to hydrogen dislocations that were stationary started to move, and those that were already in motion started to move at higher velocities.[67,69] Additionally, the rates of dislocation generation from dislocation sources increased, and the spacing of dislocations in pile-ups decreased as well as the extent of cross-slip.[67,69] It should be noted that there is controversy in these observations being direct evidence for the HELP mechanism occurring as these observations have been used to explain an adsorption-induced dislocation emission

mechanism or a combination with the proposed HELP mechanism.[67] Furthermore, compelling hypotheses on how this phenomenon would individually lead to enhanced cracking kinetics is elusive.

3) **Adsorption-Induced Dislocation Emission (AIDE):** This mechanism involves the nucleation of dislocations facilitated by the adsorption of hydrogen which weakens the interatomic bonds creating the nucleation and growth of micro-voids or nano-voids ahead of the crack tip at 2nd phase particles or slip band intersections.[67] The crack growth rate is then enhanced by the coalescence of cracks with voids occurring at a lower strain than what is required without the presence of hydrogen.[67] Evidence to support this mechanism are found by observations made with materials that have a low hydrogen diffusivity and crack velocity ratios (less than 10^{-8} cm), displaying signs of embrittlement despite the velocity of the crack growth being high enough that diffusion of hydrogen or transportation of hydrogen via dislocations in front of the crack was considered unlikely to have occurred.[67]

4) **Hydrogen-Enhanced Strain-Induced Vacancies (HESIV):** This mechanism involves the hydrogen-vacancy complex contributing to fracture by assuming a strain induced increase in the absorption capacity of hydrogen accelerates the formation of strain-induced vacancies and stabilizes vacancy clusters facilitating void initiation and growth reducing the crack growth resistance.[68,70] Evidence to support this mechanism are found via TEM observations displaying lattice expansion near the crack wake surface as well as the development of an amorphous layer less than 1 μm deep adjacent to the fracture surface, which along with micro-void formation is postulated to be a direct consequence of having high density of vacancies due to the lattice instability created by the vacancies.[70]

1.1.6. High-altitude environmental impact on fatigue behavior

A study by De Jonge and Spiekhout examined 2,496 flights and found that 80% of the flight times were spent at a "cruising altitude" (above 30,000 ft) which was found to be where 17% of the significant load peaks (larger than 0.3 g) occurred for the transport aircraft wing. However, when all "high altitude" (above 10,000 ft) environments are considered the significant load peaks

that occurred increased to 42%.[4] A high altitude environment has two components that make it distinguishable from a normal laboratory environment (1) lower partial pressure of water vapor and (2) a significant decrease in temperature. This is shown in Table 2, which lists the total pressure and temperature for each of the corresponding altitudes.[71,72] When only the difference in water vapor pressure of the bulk environment is considered the differences observed in fatigue crack growth behavior correlate well with the change in bulk water vapor that limits the hydrogen generation and uptake at the crack tip thus limiting the effects of the hydrogen embrittlement process.[48,59,61–63,65]

Additionally, important for aerospace applications is the change in temperature and understanding how it effects fatigue behavior in aluminum alloys. Initial studies to gain insights into how low temperatures effect fatigue investigated the pure metals of copper, silver, gold, aluminum, magnesium, zinc, iron and cadmium between room temperature and 4.2 K. It was shown that fatigue life increases as the temperature decreases for all of the metals which had a face-centered cubic (f.c.c) crystal structure, where zinc, a hexagonal close-packed (h.c.p) crystal structured material and iron a body-centered cubic (b.c.c.) crystal structured material underwent a brittle fracture at 90K.[73,74] This anomaly is attributed to h.c.p. and b.c.c. having lower symmetry and less slip systems than f.c.c. materials effectively causing a transition in these materials from ductile to brittle at these low temperatures.[74,75] Originally this increase in fatigue life was attributed to a higher static strength, but an unambiguous relationship between the increase in fatigue life and the increase in ultimate strength where the majority of the metals tested had this relationship max out around 100 K was not found, indicating low temperature fatigue fracture is determined by different factors.[74] More investigations into the temperature dependence on the fatigue life found similar results for those metals exhibiting a planar slip character, but a temperature independence for copper, which exhibited a wavy slip character.[75] It should be noted that these findings tested the copper sample in dry air and when the dry air was swapped for vacuum the temperature dependence on the fatigue life appeared similar to that observed in the planar slip metals. This suggests that the original results were ambiguous as the effects from temperature were not fully decoupled from other effects of the environment.[75]

Issues with decoupling temperature from other environmental effects are not limited to this study alone as a majority of the studies into the effect of temperature on fatigue life usually involve

immersing the specimens in some type of coolant, such as liquid nitrogen, hydrogen or helium and comparing these data with experiments ran at room temperature in laboratory air attributing any observed differences to temperature alone, thus neglecting the coupled effects from environment.[75] A study reviewed by Verkin et al. showed that the fatigue life of copper is dependent on the oxygen content in the environment and when fatigue testing was done in vacuum it resulted in the fatigue life being 1.5 times greater at low temperatures compared to the fatigue life at room temperature.[75] With the effects of both low water vapor pressure and low temperature coupled in a high-altitude environment a further change in the fatigue crack growth rate in aluminum alloys is observed.[6,76] The observed changes are postulated to be due to temperature impacting the kinetics of the surface reaction, hydrogen uptake, diffusion rate of hydrogen, the nature of the local dislocation structure evolution, and/or the hydrogen-dislocation interaction.[6,77,78]

A study of the effect of temperature on dislocation structure development during fatigue were done using copper and the results suggested a decrease in temperature will affect the dislocation structure of f.c.c. materials during fatigue. Specifically, there was a possible reduction of cross-slip at these lower temperatures, because the character of the deformation was unchanged from its original variety determined by the stacking fault energy of the material.[79] Other materials indicated a change in the dislocation structure developed during fatigue with one being a study by Liaw et al. where the authors fatigued polycrystalline aluminum near room temperature (298K) and 77K. TEM observations of the dislocation substructure showed a large cellular structure with high dislocation density within the cell walls at 298K and observed a homogeneous distribution of dislocation tangles at 77K.[77] Another study by Polák and Klesnil where the authors fatigued low carbon steel near room temperature and observed a cellular dislocation structure via TEM for all temperatures of 298K, 253K, 213K, 168K and 113K, but did observe a trend of "smeared" cells or less defined cellular structure, which had an inverse relationship with temperature with the 113K fatigue experiment resulting in the most smeared or least defined cellular structures.[80] A study done examining dislocation structure development in fatigued metals at the crack wake surface was unable to examine the first 50 nm of depth due to sample preparation damage,[54] which means a possible area of interest as pointed out in the review done by Verkin et al. could have been missed.[75] The basis for this claim by Verkin et al. is displayed in the study done using fatigued b.c.c. molybdenum at a temperature below the ductile-brittle transition temperature of the material. In this study, observations of a dislocation structure only occurred within the subsurface layer of

a depth of about 15 μm which was defined as an area where the dislocation density was higher than the rest of the material examined by an order of magnitude suggesting a localization to the crack wake surface.[75] Lower temperatures have also have an impact on fatigue crack growth rates, particularly f.c.c. metals where they have displayed a decrease in the fatigue crack growth rate as well as an increase in the ΔK_{th} with a decrease in temperature.[75] The reason for the change in the threshold stress intensity value is centered around the importance of plastic zone size.[25] Using basic continuum mechanics the direct role temperature plays in the size of the plastic zone can be seen in the equation used to calculate the radius of the plastic zone:

$$5) \quad h = \frac{1}{2\pi}\left(\frac{\Delta K}{\sigma_{YS}}\right)^2 \qquad \text{for plane stress} \qquad [3]$$

$$6) \quad h = \frac{1}{2\pi}\left(\frac{\Delta K}{C\sigma_{YS}}\right)^2 \qquad \text{for plane strain} \qquad [4]$$

Where C is a constant estimated to be about 1.7 and σ_{YS} is the yield strength of the material.[11] It is known that yield strength is a materials property that has an inverse relationship with temperature, thus lowering the temperature will increase the yield strength, thus causing a decrease in the size of the plastic zone at a given ΔK.[75] It is postulated that the transition from the near-threshold region to the Paris region occurs once the size of the plastic zone is about the same size as the grain diameter of the material at room temperature, thus fatigue at lower temperatures will require a higher ΔK to achieve the minimum plastic zone size required for this transition to occur.[75,81] Interestingly, in some annealed alloys, where the size of the plastic zone was smaller than the grain size, the fatigue crack propagation rate is still slower at lower temperatures when compared to room temperature data, which the authors of the study attributed to a possible lower rate of strain accumulation from a decrease in the thermal activation of dislocations.[75]

Table 2 - Changes in temperature and absolute pressure with a rise in altitude given ground conditions shown at 0 m.

Altitude (m)	Temperature (°C)	Absolute Pressure (10^4 N/m^2)
0	15.0	10.13
2000	2.00	7.95
4000	-10.98	6.17
6000	-23.96	4.72
8000	-36.94	3.57
10000	-49.90	2.65
15000	-56.50	1.21
20000	-56.50	0.55
30000	-46.64	0.12

1.2. Knowledge Gaps

The discussed work in the previous sections has established some major factors relating the microstructure of a material to its ability to resist fatigue propagation. Specifically, literature established the best microstructure for resisting fatigue propagation are those with planar slip character, distances between dislocation obstacles larger than the size of the plastic zone maximizing the slip length, the smallest volume fraction possible of constituent particles, and lead to a tortuous path for the propagating crack. Determining how best to mitigate fatigue propagation in a high-altitude environment as well as the exact role the environment plays are still up for debate. The previous sections established the deleterious effects the environment can have on aerospace components, which suffer from fatigue in not only a corrosive environment, but also in environments with non-negligible amount of water vapor content. The behavior is known to occur in the commonly used 7xxx series aluminum alloys via hydrogen embrittlement. The first step to mitigating fatigue propagation in high-altitude environments is to understand what the mechanisms are that control the process, however there is no consensus in the literature for what the exact

mechanisms are that govern the environment assisted fatigue cracking. All proposed mechanisms follow the same basic premise of water vapor entering the mouth of the crack and ending up at the crack tip. At which point surface reactions between the water vapor and the freshly exposed aluminum occurs allowing for an adsorption and absorption of atomic hydrogen into the aluminum. Then one of the previously discussed mechanisms or combinations of these mechanisms occur resulting in enhanced crack growth rates due to the hydrogen embrittlement process. The study by de Jonge et al. displayed the importance to not only consider the levels of water vapor in the environment, as increases in altitude led to decreases in water vapor pressure, but also justify the consideration of a change in temperature.[4]

It is easy to deduce that fatigue done in an environment at room temperature with less water vapor would have the exact same mechanisms at play as a moist environment at room temperature. Observed differences in the crack growth rates can be attributed to a relative decrease in bulk water available from the environment resulting in a reduction of hydrogen produced at the crack tip. It is less obvious to what exactly is happening mechanistically if this same low water vapor environment were to occur with a significant decrease in the temperature. For such conditions studies show further changes occurring to the crack kinetics due to this low temperature that is relevant to a high-altitude environment.[6,76] Particularly the study done by Burns et al. demonstrates the addition of lower temperatures in the low water vapor pressure environment will lead to an even further reduction in the crack growth rates.[6] A consensus to what exactly is leading to this further reduction in crack growth rates has yet to be determined. However it is postulated to be one or a combination of the following: 1) The surface reaction between the water vapor and aluminum is occurring at a slower reaction rate due to the decrease in temperature, 2) If the mechanism of hydrogen embrittlement relies on a diffusion step for the hydrogen then a reduction of the hydrogen diffusion rate in the aluminum could occur at the lower temperatures, 3) The hydrogen-dislocation interaction could be temperature dependent and the lower temperature could be aiding by slowing down the homogenization of slip resulting in higher stresses required for propagation, or 4) The evolution of the dislocation or damage structure could be dependent on the temperature itself, which would occur regardless of the hydrogen being there or not.

While studies to examine the crack wake or crack tip for the damage structure evolution have been done, examining the effects from a high-altitude environment on the damage structure

evolution has been limited. As it relates to cold temperatures the review done by Verkin et al. summarized the current literature at the time as having no experimental data available on the dislocation structure of the low temperature plastic zone, but some indirect data indicates some changes do occur and these changes appeared to be smaller in f.c.c metals and alloys compared to b.c.c. and h.c.p. materials.[75] Work by Grosskreutz and Shaw attempted to correlate some of the indirect evidence observed from the growth striations on the fracture surface to the dislocation structure in the subsurface, but found no correlation between them in observations made on dislocation structure of aerospace aluminum alloys 2024-T4 and 7075-T6.[82] They concluded from TEM observations made from inside the estimated plastic zone for a fatigued and uncycled specimen of AA7075-T651, that the striations were a function of macroscopic plastic strains accompanied by a blunting and resharpening of the crack tip and the plastic strain near the crack tip is accommodated by the generation of additional dislocations rather than by the motion of dislocations already present.[82] Additionally, no additional sub-grain or cell structure was introduced by fatigue, but instead the density of dislocations was increased and evenly distributed.[82] Alternatively, this lack of a difference between the deformed and as received AA7075-T6 could be due to the fact that the damage structure formed from the fatigue process in this aluminum alloy is more localized to the crack wake surface than the estimated plastic zone size. As such a significant portion of the damage structure is missed due to the sample preparation method used as it lacked the control and precision required to obtaining information from the crack wake surface.

Advancements in the technology used to prepare TEM samples (such as dual-beam focused ion beam (DB-FIB)) has enabled the selection of specific regions to be examined via TEM by using techniques such as the "H-bar method" and the "lift-out" method allowing for more precision in the characterization of fatigue damage.[83] These methods, in particular the "lift-out" method, have been used to examine the environmental effects on fatigue. This was done by Ro et al. where Al-Cu-Mg alloys were fatigued in a vacuum environment and a moist environment and the results suggested lowered plastic strain accumulation from the moist environment relative to the vacuum environment. However the authors acknowledged that the results near the crack wake surface may have been compromised by FIB damage via ion bombardment and implantation during the sample preparation process.[54] The first step in the preparation of FIB lift-out samples for TEM begins with the application of a protective layer over the area of interest, which is done using a chemical vapor

deposition (CVD) process performed with the Ga^+ ion beam. This results in the deposition of a protective barrier coating (usually amorphous platinum), but this step is known to impart damage to the substrate.[83] It was proposed by Martin that the use of a low beam current to build up an initial protection layer before the normal deposition process would alleviate this concern, however a systematic study of this method was not performed.[84]

Additionally, other issues arise when making comparative samples for fatigue damage analysis using FIB lift-out. First, the orientation of the grain boundary relative to the loading axis is generally not controlled. Bay et al. demonstrated the dislocation structure development resulting from an fatigue or fracture is dependent on the relative orientation of slip planes to the loading axis.[85] Second, the size of a FIB lift-out sample is relatively small where the typical sampling area is around 50 μm^2 or less, which can limit broad conclusions and statistically significant investigations into the mechanisms involved in the damage process during fatigue. Due to this and the crystallographic nature of the damage structure from fatigue, coupling FIB/TEM with other diffraction-based characterization methods such as electron backscattered diffraction (EBSD) is attractive as the sampling area is around $100 - 10,000$ um^2 and provides a spatial resolution is about 75 nm.[86,87] The utility of SEM-based EBSD as a technique has been demonstrated in a few studies done by Gupta et al. where the effects on high-altitude environments or moist environments were examined for AA7050-T7451, AA7075-T651, and AA2024-T351. While the benefits of using EBSD are the significant size of the sample area and generally a lack of sample preparation damage, some small scale features near the crack wake surface could be missed due to insufficient resolution offered by this technique.[64,88,89] To address this, Gupta et al. introduced a novel characterization method utilizing FIB to prepare the initiation site of a fatigue crack for EBSD analysis. This approach could be expanded to build the necessary novel multiscale characterization technique that is required to gain more insights into the effects of high-altitude environments on fatigue[88]

1.3. Research Goals

The overarching goal of this study is to increase the understanding of the phenomenon of environmentally assisted cracking that occurs in high-altitude environments on the aerospace alloy AA7075-T651, to enable the incorporation of these environmental effects into next generation LEFM life prediction approaches. This understanding would also inform new component designs

or new alloy development to mitigate the fatigue damage that has consistently plagued the aerospace industry. In order to achieve this overarching goal, there are multiple components to the goal that need to be completed:

- Research goal #1: An evaluation of alternative testing protocols designed to avoid the complicating TTR behavior observed in fatigue within low water environments.
    - By a comparison of fatigue behavior utilizing different C(T) specimen net thicknesses.
    - By a comparison of fatigue behavior utilizing a K-rise loading protocol and the standard K-shed loading protocol.
- Research goal #2: Additional targeted fatigue experiments designed to aid the determination of the mechanistic processes governing crack growth kinetics in low temperature environments using a UHV environment at various temperatures below 23°C using the standard protocol.
- Research goal #3: Develop a novel multi-scale characterization method using EBSD, HR-EBSD, and FIB/TEM to examine the local damage structure of a fatigue fractured specimen to gain insights into the mechanisms of fatigue cracking in high altitude environments.
- Research goal #4: Apply the developed multi-scale characterization method to further inform the mechanisms at play in high altitude environments on the targeted fatigue experiments
- Research goal #5: Use all the results from this dissertation to address previously mentioned questions about what could be responsible for the reduction in crack growth kinetics in high altitude environments:
    - Slower surface reaction between the water molecules and aluminum needed to generate atomic hydrogen?
    - Significantly slower diffusion rate of atomic hydrogen?
        - Addressed by additional fatigue experiments utilizing a constant ΔK and different frequencies
    - A temperature dependent evolution of the damage structure independent of hydrogen?
    - A temperature dependent hydrogen-damage structure interaction?

1.4. Dissertation Overview

The following dissertation is organized into five chapters, which can be divided into four main research objectives. First, addressing research goal #1, Chapter 2 describes a study utilizing AA7075-T651 aluminum to evaluate the impact sample thickness and loading protocol have on

the fatigue behavior, particularly related to the phenomenon known as the threshold transition regime (TTR).[45,75] This TTR phenomenon is a known outcome from AA7075-T651 occurring with fatigue in low water vapor environments associated with high altitude environments. By evaluating the relative effect of the previously mentioned parameters (sample thickness, loading protocol) through targeted fatigue experiments, this study will aim to inform if the complications caused by the TTR behavior can be eliminated or mitigated for the purpose of enabling straightforward application for LEFM models.

The second objective, presented in Chapter 3, describes a series of fatigue experiments completed in low temperature, ultra high vacuum (UHV) environments addressing research goal #2. Common practices for achieving low temperature make isolating the variable of temperature very difficult as the created environments generally include low levels of water vapor or ice formation on surfaces, both of which have been shown to have an impact on fatigue behavior in AA7075-T651.[75] Understanding the low temperature effects independent of hydrogen provides valuable insights into the impact of high altitude environments on fatigue.

The third objective, presented in Chapter 4 and 5, addresses research goals #3, and 4, by first providing an overview of the creation of a novel multi-scale characterization protocol utilizing EBSD, HR-EBSD, FIB, and TEM, to characterize the near-crack deformation created by fatigue to address the questions which motivated this research. The discussed characterization protocol will be applied to previously fatigued samples to gain insights and understanding of the damage structure evolution within low water vapor and low temperature environments.

Finally, the last objective will address research goal #5, presented in Chapters 3 and 5, where the results of the studies described in these chapters will begin to answer the questions posed by research goal #5 about what is responsible for the reduction in crack growth kinetics in high altitude environments. In addition, constant ΔK fatigue segments utilizing low temperature, constant P_{H2O}/f and different frequencies will be executed to address the question of temperature dependent hydrogen diffusion possibly being responsible for the fatigue behavior in high altitude environments.

Each chapter begins with a brief summary of the chapter, followed by a succinct background section which ends with the objectives of the particular study described in the chapter. An overview of the experimental methods are also provided, followed by the results and further

discussion of relevant takeaways from the results. Each chapter is then concluded with a summary of the main conclusions and a brief section outlining possible future research pertinent to the work described in the chapter.

1.5. References

1. Mouritz, A. P. *Introduction to Aerospace Materials*. (Woodhead Publishing, 2012).

2. Howard, R., Bogh, N. & MacKenzie, D. S. Heat Treating Processes and Equipment. in *Handbook of Aluminum* (eds. Totten, G. E. & MacKenzie, D. S.) 881–970 (Marcel Dekker, Inc., 2003).

3. Pook, L. *Metal Fatigue What It Is, Why It Matters*. (Springer, 2007).

4. Barsom, J. & Rolfe, S. *Fracture & Fatigue Control in Structures*. (Prentice-Hall, Inc., 1987).

5. Findlay, S. J. & Harrison, N. D. Why aircraft fail. *Mater. Today* **5**, 18–25 (2002).

6. Shoales, G. A., Fawaz, S. A. & Walters, M. R. Compilation of Damage Findings From Multiple Recent Teardown Analysis Programs. in *Bridging the Gap between Theory and Operational Practice* 187–207 (2009). doi:https://doi.org/10.1007/978-90-481-2746-7_11.

7. Gdoutos, E. . *Fracture Mechanics: An Introduction*. (Kluwer Academic Publishers, 1993).

8. Ewalds, H. L. & Wanhill, R. J. H. *Fracture Mechanics*. (E. Arnold, 1984).

9. Anderson, T. L. *Fracture Mechanics: Fundamentals and Applications*. (CRC Press, 1995).

10. Sanders, R. E. & Starke, E. A. The effect of intermediate thermomechanical treatments on the fatigue properties of a 7050 aluminum alloy. *Metall. Trans. A* **9**, 1087–1100 (1978).

11. Wei, L., Pan, Q., Wang, Y., Feng, L. & Huang, H. Characterization of fracture and fatigue behavior of 7050 aluminum alloy ultra-thick plate. *J. Mater. Eng. Perform.* **22**, 2665–2672 (2013).

12. Lütjering, G., Albrecht, J., Sauer, C. & Krull, T. The influence of soft, precipitate-free zones at grain boundaries in Ti and Al alloys on their fatigue and fracture behavior. *Mater. Sci. Eng. A* **468–470**, 201–209 (2007).

13. Chen, J. Z., Zhen, L., Yang, S. J. & Dai, S. L. Effects of precipitates on fatigue crack growth rate of AA 7055 aluminum alloy. *Trans. Nonferrous Met. Soc. China (English Ed.* **20**, 2209–2214 (2010).

14. Deschapelles, J. B. & Rice, R. C. Improved Fatigue Resistance of 7050 Thick Plate Aluminum Through Minimization of Microporosity. *Am. Soc. Test. Mater.* **ASTM STP 1**, (1998).

15. Desmukh, M. N., Pandey, R. K. & Mukhopadhyay, A. K. Effect of aging treatments on the kinetics of fatigue crack growth in 7010 aluminum alloy. *Mater. Sci. Eng. A* **435–436**, 318–326 (2006).

16. Wang, Y. L., Pan, Q. L., Wei, L. L., Li, B. & Wang, Y. Effect of retrogression and reaging treatment on the microstructure and fatigue crack growth behavior of 7050 aluminum alloy

thick plate. *Mater. Des.* **55**, 857–863 (2014).

17.   Newman, J. C., Anagnostou, E. L. & Rusk, D. Fatigue and crack-growth analyses on 7075-T651 aluminum alloy coupons under constant- and variable-amplitude loading. *Int. J. Fatigue* **62**, 133–143 (2014).

18.   Forth, S. C., Newman Jr., J. C. & Forman, R. G. On generating fatigue crack growth thresholds. *Int. J. Fatigue* **25**, 9–15 (2003).

19.   Starke Jr., E. A. & Williams, J. C. Microstructure and the Fracture Mechanics of Fatigue Crack Propagation. in *Perspectives and Directions (20th Symposium)* (eds. Wei, R. P. & Gangloff, R. P.) 184–205 (American Society for Testing and Materials, 1989).

20.   Tiryakioglu, M. & Staley, J. Effect of Alloying Additions in Aluminum Alloys. in *Handbook of Aluminum* (eds. Totten, G. & MacKenzie, D.) 120–130 (Marcel Dekker, Inc., 2003).

21.   Bucci, R. J. & Starke Jr., E. A. Selecting aluminum alloys to resist failure by fracture mechanisms. *ASM Handb. Fatigue Fract.* **19**, 771–812 (1996).

22.   Hornbogen, E. & Gahr, K. H. Zum. Microstructure and fatigue crack growth in a γ-Fe-Ni-Al alloy. *Acta Metall.* (1976) doi:10.1016/0001-6160(76)90104-8.

23.   Lindigkeit, J., Terlinde, G., Gysler, A. & Lütjering, G. The effect of grain size on the fatigue crack propagation behavior of age-hardened alloys in inert and corrosive environment. *Acta Metall.* (1979) doi:10.1016/0001-6160(79)90086-5.

24.   Robinson, J. L. & Beevers, C. J. The effects of load ratio, interstitial content, and grain size on low-stress fatigue crack propagation in α-titanium. *Metall. Sci. J.* **7**, 153–159 (1973).

25.   Chakrabortty, S. B. A Model Relating Low Cycle Fatigue Properties and Microstructure to Fatigue Crack Propagation Rates. *Fatigue Fract. Eng. Mater. Struct.* **2**, (1979).

26.   Davidson, D. . & Lankford, J. The Effects of Aluminum Alloy Microstructure on Fatigue Crack Growth. *Mater. Sci. Eng.* **74**, 189–199 (1985).

27.   Telesman, J. *Review of the Effects of Microstructure on Fatigue in Aluminum Alloys*. (1984).

28.   Laird, C. Mechanisms and Theories of Fatigue. *Am. Soc. Met.* 149–203 (1979).

29.   Pippan, R. & Hohenwarter, A. Fatigue crack closure: a review of the physical phenomena. *Fatigue Fract. Eng. Mater. Struct.* **40**, 471–495 (2017).

30.   Lin, F. S. & Starke, E. A. The effect of copper content and degree of recrystallization on the fatigue resistance of 7XXX-type aluminum alloys II. Fatigue crack propagation. *Mater. Sci. Eng.* **43**, 65–76 (1980).

31.   Suresh, S. Fatigue crack deflection and fracture surface contact: Micromechanical models. *Metall. Trans. A* **16**, 249–260 (1985).

32.   Minakawa, K. & McEvily, A. J. On Crack Closure in the Near-Threshold Region. *Acta Metall.* **15**, 633–636 (1981).

33.   Bai, S., Liu, Z., Zhou, X., Gu, Y. & Yu, D. Strain-induced dissolution of Cu-Mg co-clusters and dynamic recrystallization near a fatigue crack tip of an underaged Al-Cu-Mg alloy during cyclic loading at ambient temperature. *Scr. Mater.* **64**, 1133–1136 (2011).

34. Wang, S.-S. *et al.* Microstructure evolution in abrasion-induced surface layer on Al-Zn-Mg-Cu alloy. *Mater. Charact.* **98**, 18–25 (2014).

35. Scamans, G. M. *et al.* The ubiquitous Beilby layer on aluminum surfaces. *Surf. Interface Anal.* **42**, 175–179 (2010).

36. Weiland, H. *et al.* Microstructural aspects of crack nucleation during cyclic loading of AA7075-T651. *Eng. Fract. Mech.* (2009) doi:10.1016/j.engfracmech.2008.11.012.

37. Payne, J., Welsh, G., Christ, R. J., Nardiello, J. & Papazian, J. M. Observations of fatigue crack initiation in 7075-T651. *Int. J. Fatigue* (2010) doi:10.1016/j.ijfatigue.2009.06.003.

38. Harlow, D. G., Wang, M. Z. & Wei, R. P. Statistical analysis of constituent particles in 7075-T6 aluminum alloy. *Metall. Mater. Trans. A Phys. Metall. Mater. Sci.* **37**, 3367–3373 (2006).

39. Hahn, G. T. & Rosenfield, A. R. Metallurgical factors affecting fracture toughness of aluminum alloys. *Metall. Trans. A* **6**, 653–668 (1975).

40. Harlow, D. G., Nardiello, J. & Payne, J. The effect of constituent particles in aluminum alloys on fatigue damage evolution: Statistical observations. *Int. J. Fatigue* (2010) doi:10.1016/j.ijfatigue.2009.02.036.

41. DeBartolo, E. A. & Hillberry, B. M. Effects of constituent particle clusters on fatigue behavior of 2024-T3 aluminum alloy. *Int. J. Fatigue* **20**, 727–735 (1998).

42. Gangloff, R. P. Environment sensitive fatigue crack tip processes and propagation in aerospace aluminum alloys. *Fatigue* **2**, 3401–3433 (2002).

43. Hénaff, G., Odemer, G. & Tonneau-Morel, A. Environmentally-assisted fatigue crack growth mechanisms in advanced materials for aerospace applications. *Int. J. Fatigue* **29**, 1927–1940 (2007).

44. Holroyd, N. J. H. & Hardie, D. Corrosion Fatigue of 7000 Series Aluminum Alloys. *Am. Soc. Test. Mater.* 534–547.

45. Burns, J. T. *et al.* Effect of water vapor pressure on fatigue crack growth in Al − Zn − Cu − Mg over wide-range stress intensity factor loading. *Eng. Fract. Mech.* **137**, 34–55 (2015).

46. Sanders, T. H. & Stanley, J. T. Review of Fatigue and Fracture Research on High-Strength Aluminum Alloys. *Am. Soc. Met.* 467–522 (1979).

47. Chanani, G. R. *Fundamental Investigation of Fatigue Crack Growth Retardation in Aluminum Alloys.* (1976).

48. Truckner, W. G., Staley, J. T., Bucci, R. J. & Thakker, A. B. *Effect of Microstructure on Fatigue Crack Growth of High-Strength Aluminum Alloys.* (1976).

49. Lynch, S. P. Mechanisms of Fatigue and Environmentally Assisted Fatigue. *ASTM Int.* **675**, 174–213 (1979).

50. Nix, K. J. & Flower, H. M. The micromechanisms of fatigue crack growth in a commercial Al-Zn-Mg-Cu alloy. *Acta Metall.* **30**, 1549–1559 (1982).

51. Burns, J. T. *et al.* Effect of water vapor pressure on fatigue crack growth in Al-Zn-Cu-Mg over wide-range stress intensity factor loading. *Eng. Fract. Mech.* **137**, 34–55 (2014).

52.   Ro, Y., Agnew, S. R. & Gangloff, R. P. Effect of environment on fatigue crack wake dislocation structure in Al-Cu-Mg. *Metall. Mater. Trans. A Phys. Metall. Mater. Sci.* **43**, 2275–2292 (2012).

53.   Piascik, R. S. & Gangloff, R. . Environmental fatigue of an Al-Li-Cu alloy: part I. Intrinsic crack propagation kinetics in hydrogenous environments. *Metall. Trans. A* **22**, 2415–2428 (1991).

54.   Gingell, A. D. B. & King, J. E. The effect of Frequency and Microstructure on Corrosion Fatigue Crack Propagation in High Strength Aluminum Alloys. *Acta Metall.* **45**, 3855–3870 (1996).

55.   Staley, J. T. Aluminum Alloy and Process Developments for Aerospace. *Met. Eng. Q.* **16**, 52–57 (1976).

56.   Gangloff, R. P. *Corrosion fatigue crack propagation in metals*. (1990).

57.   Bonakdar, A., Wang, F., Williams, J. J. & Chawla, N. Environmental Effects on Fatigue Crack Growth in 7075 Aluminum Alloy. *Metall. Mater. Trans. A* **43A**, 2799–2809 (2011).

58.   Wei, R. P. & Gao, M. Reconsideration of the Superposition Model for Environmentally Assisted Fatigue Crack Growth. *Scr. Metall.* **17**, 959–962 (1983).

59.   Pao, P. S., Gao, M. & Wei, R. P. Environmentally assisted fatigue-crack growth in 7075 and 7050 aluminum alloys. *Scr. Metall.* **19**, 265–270 (1985).

60.   Ruiz, J. & Elices, M. Effect of water vapour pressure and frequency on fatigue behaviour in 7017-t651 aluminium alloy plate. *Acta Mater.* **45**, 281–293 (1997).

61.   Davidson, D. L. & Lankford, J. The Effects of Water Vapor on Fatigue Crack Tip Mechanics in 7075-T651 Aluminum Alloy. *Fatigue Fract. Eng. Mater. Struct.* **6**, 241–256 (1983).

62.   Gupta, V. K., Gangloff, R. P. & Agnew, S. R. Diffraction characterization of microstructure scale fatigue crack growth in a modern Al-Zn-Mg-Cu alloy. *Int. J. Fatigue* **42**, 131–146 (2012).

63.   Ro, Y. J., Agnew, S. R., Bray, G. H. & Gangloff, R. P. Environment-exposure-dependent fatigue crack growth kinetics for Al-Cu-Mg/Li. *Mater. Sci. Eng. A* **468–470**, 88–97 (2007).

64.   Young Jr., G. A. & Scully, J. R. The Effects of Test Temperature, Temper, and Alloyed Copper on the Hydrogen-Controlled Crack Growth Rate of an Al-Zn-Mg-(Cu) Alloy. *Metall. Mater. Trans. A* **33A**, 1167–1181 (2002).

65.   Lynch, S. Hydrogen embrittlement phenomena and mechanisms. *Corros. Rev.* **30**, 105–123 (2012).

66.   Li, X. *et al.* Review of Hydrogen Embrittlement in Metals : Hydrogen Diffusion , Hydrogen Characterization , Hydrogen Embrittlement Mechanism and Prevention. *Acta Metall. Sin. (English Lett.* (2020) doi:10.1007/s40195-020-01039-7.

67.   Robertson, I. A. N. M. *et al.* Hydrogen Embrittlement Understood. *Metall. Mater. Trans. A* **46**, 2015–2323 (2015).

68.   Nagumo, M. Hydrogen related failure of steels - a new aspect. *Mater. Sci. Technol.* **20**, 940–

950 (2004).

69.   de Jonge, J. B. & Spiekhout, D. J. Use of AIDS Recorded Data for Assesing Service Load Experience. in *Service Fatigue Loads Monitoring, Simulation, and Analysis* 48–66 (1979).

70.   DeHoff, R. *Thermodynamics in Materials Science*. (CRC Press, 2006).

71.   Adminstration, N. O. and A. A. (NOAA), (NASA), N. A. and S. A. & (USAF), U. S. A. F. *U.S. Standard Atmosphere, 1976*. (1976).

72.   Verkin, B. I., Grinberg, N. M., Serdyuk, V. A. & Yakovenko, L. F. Low temperature fatigue fracture of metals and alloys. *Mater. Sci. Eng.* **58**, 145–168 (1983).

73.   McCammon, R. D. & Rosenberg, H. M. The fatigue and ultimate tensile strengths of metals between 4.2 and 293° K. *R. Soc.* **242**, (1957).

74.   Verkin, B. I., Grinberg, N. M., Serdyuk, V. A. & Yakovenko, L. F. Low Temperature Fatigue Fracture of Metals and Alloys. *Mater. Sci. Eng.* **58**, 145–168 (1983).

75.   Burns, J. T., Jones, J. J., Thompson, A. W. & Warner-Locke, J. S. Fatigue crack propagation of aerospace aluminum alloy 7075-T651 in high altitude environments. *Int. J. Fatigue* **106**, 196–207 (2018).

76.   Meng, X., Lin, Z. & Wang, F. Investigation on corrosion fatigue crack growth rate in 7075 aluminum alloy. *Mater. Des.* **51**, 683–687 (2013).

77.   Liaw, P. K., Fine, M. E., Kiritani, M. & Ono, S. The Effect of Temperature on the Fatigue Crack Propagation Rate in Aluminum. *Scr. Metall.* **11**, 1151–1155 (1977).

78.   Feltner, C. E. Dislocation arrangements in aluminum deformed by repeated tensile stresses. *Acta Metall.* **11**, 817–828 (1963).

79.   Basinski, Z. S., Korbel, A. S. & Basinski, S. J. The Temperature Dependence of the Saturation Stress and Dislocation Substructure in Fatigued Copper Single Crystals. *Acta Metall.* **28**, 191–207 (1980).

80.   Polak, J. & Klesnil, M. The Dynamics of Cyclic Plastic Deformation and Fatigue Life of Low Carbon Steel at Low Temperature. *Mater. Sci. Eng.* **26**, 157–166 (1976).

81.   Hahn, G. T., Hoagland, R. G. & Rosenfield, A. R. Local yielding attending fatigue crack growth. *Metall. Trans.* **3**, 1189–1202 (1972).

82.   Grosskreutz, J. C. & Shaw, G. G. Microstructures at the Tips of Growing Fatigue Cracks in Aluminum Alloys. *Am. Soc. Test. Mater.* **ASTM STP 4**, 226–240 (1967).

83.   Brandon, D. & Kaplan, W. D. *Microstructural Characterization of Materials*. (John Wiley & Sons, Inc., 2008).

84.   Martin, M. L. A New Approach to Discovering the Fundamental Mechanisms of Hydrogen Failure. (University of Illinois at Urbana-Champaign, 2013).

85.   Bay, B., Hansen, N. & Kuhlmann-Wilsdorf, D. Microstructural evolution in rolled aluminum. *Mater. Sci. Eng. A* **158**, 139–146 (1992).

86.   Ruggles, T. J., Rampton, T. M., Khosravani, A. & Fullwood, D. T. Ultramicroscopy The effect of length scale on the determination of geometrically necessary dislocations via EBSD continuum dislocation microscopy. *Ultramicroscopy* **164**, 1–10 (2016).

87. Wilkinson, A. J., Meaden, G. & Dingley, D. J. High-resolution elastic strain measurement from electron backscatter diffraction patterns : New levels of sensitivity. **106**, 307–313 (2006).

88. Gupta, V. K. & Agnew, S. R. Fatigue crack surface crystallography near crack initiating particle clusters in precipitation hardened legacy and modern Al-Zn-Mg-Cu alloys. *Int. J. Fatigue* **33**, 1159–1174 (2011).

89. Gupta, V. K. & Agnew, S. R. Measuring the effect of environment on fatigue crack-wake plasticity in aluminum alloy 2024 using electron backscatter diffraction. *Mater. Sci. Eng. A* **494**, 36–46 (2008).

90. E647-15e1 Standard Test Method for Measurement of Fatigue Crack Growth Rates. *ASTM Int.* 1–49 (2015) doi:10.1520/E0647-15E01.2.

91. Newman Jr., J., Schneider, J., Daniel, A. & McKnight, D. Compression pre-cracking to generate near threshold fatigue-crack-growth rates in two aluminum alloys. *Int. J. Fatigue* **27**, 1432–1440 (2005).

Chapter 2 – Evaluation of experimental loading protocol for fatigue

2.1. Overview

In order to ensure the safe operation of aircraft, it is critical that the fatigue behavior be well-characterized to inform inspection requirements, maintenance decisions, and operational constraints. Linear elastic fracture mechanics (LEFM) is often used to assess the fatigue behavior of a material because of the ability to directly transfer laboratory-measured fatigue crack propagation data to actual engineered components via a concept of similitude. The LEFM approach is the basis for damage tolerance analysis software such as AFGROW that is commonly used in the aerospace industry to predict the life of engineered components within aircraft subjected to fatigue. However, similitude can be difficult to maintain when modifications in specimen-induced artifacts, geometry-related phenomena and environment occur, thus rendering some laboratory data not appropriate for use in the damage tolerant design assessments.

Literature establishes that the fatigue crack growth behavior of Al alloys is highly sensitive to the water vapor within the environment and it is widely accepted that this is attributed to the hydrogen embrittlement mechanism.[1–9] Commonly, the severity of the water vapor in the environment is defined using the exposure parameter, P_{H2O}/f, which quantifies the product of the partial pressure of water vapor and the time available for the water vapor to react with the fresh surface created by the cracking process.[3,7] High altitude environments are notably distinguishable from normal laboratory environments by having a lower P_{H2O} and these significant differences in P_{H2O} are important as studies have shown fatigue testing on aluminum alloys in a vacuum, dry air or low humidity environment results in significantly slower fatigue crack growth rates when compared to those tested in moist or high humidity environments.[3,10–18,19]

Commonly, fatigue crack growth rate experiments testing in the threshold and/or near-threshold regime are run using a "load-shedding" protocol, because it allows data collection for crack growth rates below 10^{-8} m/cycle.[20,21] Recent studies generating fatigue data in low P_{H2O} environments observed a unique crack growth behavior at intermediate stress intensity (ΔK) levels.[3,16,22,23] While using the standard decreasing ΔK testing protocol as described in ASTM-E647, this unique behavior features an observed "false" threshold, which is followed by a sudden "spike" (sometimes multiple) in the fatigue crack growth rate (da/dN), which is further followed by a steady decrease in da/dN leading to a second environmental threshold value.[3,16,23]

Microscopy-based evaluations of the region revealed this region revealed that the onset of the reduction in growth rates correspond to a systematic change in the fracture morphology from a flat transgranular morphology to a rough slip band cracking morphology (SBC). Subsequently, an irregular crack front develops.[3] This crack growth behavior was termed the threshold transition regime (TTR). This behavior is speculatively attributed to the roughness created by the changing crack wake morphology affecting the molecular transport of water vapor from the bulk environment to the crack tip.[3,16] This speculation suggests fatigue crack growth rates may be dependent on the specimen geometry (specimen thickness) and therefore potentially negating the similitude of the fracture mechanics required for implementation into LEFM-based models. However, there remains a possibility of this behavior being related to the loading protocol, in this case a decreasing ΔK protocol which was not rigorously examined and therefore remains a possible source of negation of similitude of the fracture mechanics.

The objective of this study is to evaluate the impact a reduction of specimen thickness and a change in loading protocol have on the fatigue crack growth behavior, specifically the TTR behavior of the legacy aerospace alloy AA7075-T651. To evaluate the specimen thickness reduction, fatigue crack propagation experiments using a constant decreasing driving force protocol were conducted using three different net specimen thicknesses at five water vapor pressures ranging from ~10^{-9} Pa to 26680 Pa. To evaluate the change in loading protocol a series of experiments were executed using a compression pre-crack to enable a rising driving force loading protocol. The implications and results of these findings on testing of materials in representative environments is discussed and interpreted in the context of fracture mechanics similitude.

2.2. Experimental Methods

2.2.1. Materials

All experiments were conducted on AA7075-T651 procured in the form of a 50.8-mm thick plate. This material heat was previously utilized in an interdisciplinary multiscale airframe fatigue prognosis study to simulate the alloy composition typical of AA7075 used in older aircraft.[24] Specifically, while this alloy meets the current elemental specification for AA7075, it contains an elevated iron and silicon content relative to what is typically observed in modern AA7075 heats.[25] Mechanical properties and the elemental composition for the tested material heat are listed in

Tables 3 and 1, respectively; a detailed microstructural analysis is presented elsewhere.[26,27] Compact tension [C(T)] specimens with a width (W) of 50.8 ± 0.51 mm were extracted from the plate in the L-T orientation (loading axis parallel to the rolling direction of the plate, crack growth occurring in the transverse direction), such that the C(T) specimen mid-thickness was located at a depth of ≈8.5 mm from the plate surface (*i.e.*, S/6 location, where S is the plate thickness). The specimen thickness (B) was varied in this study as follows. For specimens designated as "thick", B was 7.62 mm ± 0.51 mm, while specimens designated as "medium" had the same B but were side-grooved such that the net thickness (B_N) was 5.74 ± 0.25 mm. Finally, specimens designated as "thin" were manufactured with B = 5.74 ± 0.25 mm and B_N = 4.92 ± 0.25 mm. The majority of specimens were machined with a starter notch depth (a_0) of 12.7 ± 0.51 mm ahead of the load line, while a small number had a_0 = 10.7 ± 0.51 mm.

Table 3 - Select mechanical properties for the material AA7075-T651 used in this study.

σ_{ys} (MPa)	K_{IC} (MPa√m)	E (GPa)	Average Grain Size (mm)		
508 (L)	33 (L-T)	≈72	1-2 (L)	0.05-0.074 (T)	0.08-0.019 (S)

2.2.2. Fatigue crack growth experiments (ΔK-shed protocol)

Fatigue crack growth experiments were performed using a decreasing stress intensity factor range (ΔK) protocol (ΔK-shed) conducted in accordance with ASTM Standard E647.[28] The crack length was actively calculated throughout each experiment *via* the specimen compliance determined from the crack mouth opening displacement measured by an attached clip gage. All specimens were fatigue precracked in laboratory air using a constant amplitude loading protocol with a stress ratio (R) of 0.1 and frequency (*f*) of 5 Hz, such that K_{MAX} value reached 10 MPa√m after 1 mm of crack propagation (typical maximum load was ~3.4 kN). Each ΔK-shed experiment was conducted at f = 20 Hz and R of 0.5, with ΔK decreasing as a function of crack length (a) according to $\Delta K = \Delta K_o e^{C(a-a_o)}$, where the initial ΔK ($\Delta K_o$) was 10 MPa√m, initial crack length (a_o) corresponded to the final crack length recorded at the end of the pre-crack protocol, and the K-gradient (C) was -0.08 mm^{-1}.[29] Testing was stopped when either da/dN was consistently less than 1.0 x 10^{-7} mm/cycle, ΔK reached 2 MPa√m, or the R^2 value for a linear fit to the measured compliance fell below 0.8. Crack growth rates were calculated using the 7-point (n = 3) incremental polynomial method described in ASTM E647[29] and the effective ΔK was determined

using the adjusted compliance ratio (ACR) method outlined by the studies done by Donald et al.[30,31]

2.2.3. Fatigue crack growth experiments (ΔK-rise protocol)

Fatigue crack growth experiments conducted under a rising ΔK protocol were performed following the methodology similar to that employed by Newman and coworkers.[32] First, each specimen was cyclically loaded at R = 0.1 and f = 1 Hz using a constant amplitude protocol (maximum load of 3 kN) to obtain initial compliance ratio and dimensionless compliance (EvB/P) values. Then, each specimen was precracked using a compression-compression fixed amplitude loading protocol with R = 10, f = 5 Hz, and a minimum load of -4.5 kN for a fixed cycle count of ~2.5x10^6 cycles, as suggested by Newman.[32] To prevent contact between the top and bottom clevises during compression loading, a small block of AA7075 with dimensions 12.77 mm x 7.31 mm x 10.20 mm (L x W x H) was glued to the top of the C(T) specimen, centered on the load line. After completion of this compression pre-cracking step, typical clip gage-indicated crack extension was ~0.2 mm. The rising ΔK protocol was then performed under fixed amplitude loading at R = 0.5 and f = 20 Hz such that K_{max} increased from 4 to 32 MPa√m. As with the ΔK-shed testing, crack growth rates were calculated using the 7-point (n = 3) incremental polynomial method and the effective ΔK was determined using the adjusted compliance ratio (ACR) method.[28,30,31]

2.2.4. Environmental control

All experiments were conducted at room temperature utilizing various environments defined by the partial pressure of water (P_{H2O}). The water used for all of the experiments was Type I deionized water, which is defined by ASTM D1193.[33] The environments used for this study were 2668 Pa, 38 Pa, 0.54 Pa, 0.0675 Pa and less than 1.33 x 10^{-6} Pa, which the last was designated as an ultra-high vacuum (UHV) environment. All experiments conducted at P_{H2O} ≤ 38 Pa were performed using a mechanical load frame integrated into a Cu gasket-sealed stainless steel vacuum chamber, described in detail elsewhere.[34] Prior to the introduction of water vapor to achieve the P_{H2O} of interest, the chamber was first evacuated to a pressure less than 1.33 x 10^{-6} Pa using a series of vacuum pumps. For environments of 38 Pa > P_{H2O} > 1.33 x 10^{-6} Pa, water vapor was introduced from a sealed glass flask *via* a calibrated leak valve, with the P_{H2O} of interest dynamically maintained by balancing the water vapor input and the evacuated output using a turbo-

molecular pump. The pressure inside the chamber was monitored throughout the duration of the experiments using a HPS series 937A high vacuum multi-sensor system with series 423 I-MAG cold cathode sensors and type 722A absolute pressure transducers to ensure the pressure was maintained within 1% of the of the target pressure. Experiments conducted at $P_{H2O} > 38$ Pa utilized an acrylic environmental cell clamped to the C(T) specimen and then sealed with vacuum grease, thereby isolating the Mode I crack path in the environment of interest. Nitrogen gas was bubbled through Type I deionized water to humidify the gas and then pump the humidified gas into the sealed environmental cell, with the gas flow occurring parallel to the crack front (*i.e.,* through the notch and crack wake area). The temperature and RH within the cell were continuously monitored to ensure that the targeted environmental condition had a RH > 95% and was maintained throughout the experiment.

2.3. Results

2.3.1. The effect of specimen thickness on the fatigue crack growth behavior

Commonly, the bulk environment for fatigue of aluminum is defined using a water exposure parameter (P_{H2O}/f), which factors the partial water vapor pressure in the bulk environment and the frequency of the cyclic loading. Previous studies examining fatigue crack growth behavior at 23°C using a K-shed protocol for a variety of different water exposures indicated AA7075-T651 undergoing fatigue in a "low exposure" environment had insufficient amounts of water vapor in the bulk environment to facilitate environmental assisted cracking (EAC).[3,16] In this study, fatigue in a "low exposure" environment, a $P_{H2O} < 1.33$ x 10^{-6} Pa or UHV, yielded results consistent with mechanically driven cracking behavior shown in Figure 1, which was similar to results seen in similarly "low exposure" environments examined in the previous studies.[3,16] The growth kinetics as well as the fractography of the fracture surfaces for the three different specimen thicknesses examined were fundamentally similar in behavior and appearance with all three specimens yielding a threshold value (ΔK_{th}) around 5 MPa√m.

Fatigue using a "high exposure" environments with a P_{H2O}/f of 133.4 Pa·s and 1.9 Pa·s yielded results shown in Figures 2 and 3 that are consistent with EAC in this material, which is overall faster crack growth rates, specifically accelerated crack growth rates in the intermediate and near-threshold ΔK value ranges as well as a significant decrease in the ΔK_{th}. The growth kinetics as well as the fractography of the fracture surface for the three different specimen

thicknesses examined and shown in Figures 2 and 3 respectively were fundamentally similar in behavior and appearance. These results were consistent with the comparative results in "high exposure" environments examined in the previous studies where "high exposure" environments at 23°C using a K-shed protocol was shown to have a sufficient amount of water vapor in the bulk environment to initiate EAC controlled cracking governed by the reaction rate of water and aluminum producing atomic hydrogen and the diffusion rate of atomic hydrogen to the processing zone.[3,16]

In contrast, fatigue cracking using a K-shed protocol at 23°C in the "intermediate exposure" environments with P_{H2O}/f values of 0.027 Pa·s and 0.003375 Pa·s seen in Figures 4 and 5, resulted in an anomaly in the fatigue crack growth behavior occurring in the Paris regime. This anomaly presented with a similar crack behavior and cracking rates found in the "low exposure" environment at intermediate ΔK values, but a false threshold appears at a ΔK value similar to the observed ΔK_{th} for this material in a UHV environment. The false threshold minimum crack growth rate is subsequently followed by a sharp increase in the crack growth rate as the driving force decreases before once again exhibiting behavior that can be more commonly associated with EAC around a ΔK of < 3 MPa√m. This same phenomenon was observed in previous studies and was termed the threshold transition regime (TTR), with the behavior being attributed to an uneven advancing crack front. This irregularity is caused by the surface roughness morphology limiting the water supply at the crack tip near the center width of the C(T) specimen, slowing the crack growth rate relative to the edges of the specimen where there is enhanced access to the bulk environment.[3,16] The TTR event was observed to occur for all specimens exposed to an "intermediate exposure" environment at a ΔK value between 5 and 6 MPa√m, while the data from the 0.003375 Pa·s environment had evidence of a second TTR event occurring at a ΔK value around 3 MPa√m. These results were consistent with the comparative results in "intermediate exposure" environments examined in the previous studies.[3,16] The growth kinetics as well as the fractography of the fracture surface for the different specimen thicknesses examined and displayed in Figures 4 and 5 were fundamentally similar in behavior and appearance.

Similarly, fatigue cracking using the K-rise protocol at 23°C in the "intermediate exposure" a P_{H2O}/f value of 0.027 Pa·s seen in Figure 6, resulted in a similar anomaly in the fatigue crack growth behavior that occurred in the Paris regime as was observed using the K-shed protocol for

two of the thickness of C(T) specimens used in this study. The growth kinetics as well as the fractography of the fracture surfaces for the two different specimen thicknesses examined were fundamentally similar in behavior and appearance with both specimens displaying a TTR region in the ΔK range of 4 to 9 MPa√m.
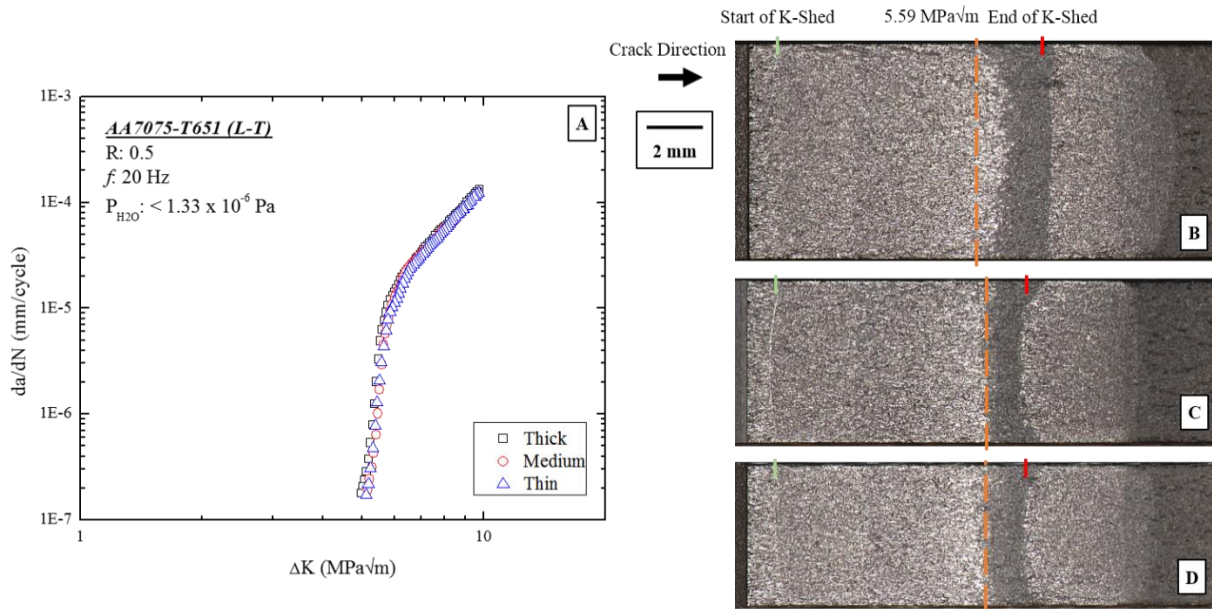
Figure 1 - (a) Fatigue crack growth rate versus ΔK relationships measured for AA7075-T651 (L-T) as a function of net section thickness using a decreasing ΔK protocol, where C = -0.08 1/mm, f = 20 Hz, and a water vapor pressure of <1 x 10-6 Pa (UHV). Overview micrographs for the thick, medium, and thin specimens are shown in (b), (c), and (d), respectively, with crack growth occurring from left to right. The orange line represents the location for the onset of the SBC mechanism with the corresponding driving force.
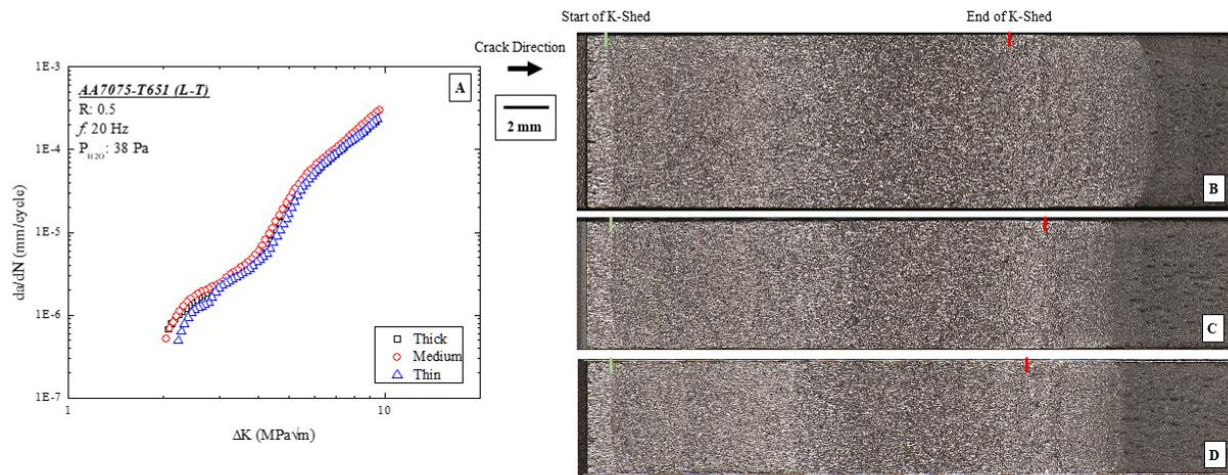
Figure 2 - (a) Fatigue crack growth rate versus ΔK relationships measured for AA7075-T651 (L-T) as a function of net section thickness using a decreasing ΔK protocol, where C = -0.08 1/mm, f = 20 Hz, and a

water vapor pressure of 38 Pa. Overview micrographs for the thick, medium, and thin specimens are shown in (b), (c), and (d), respectively, with crack growth occurring from left to right.
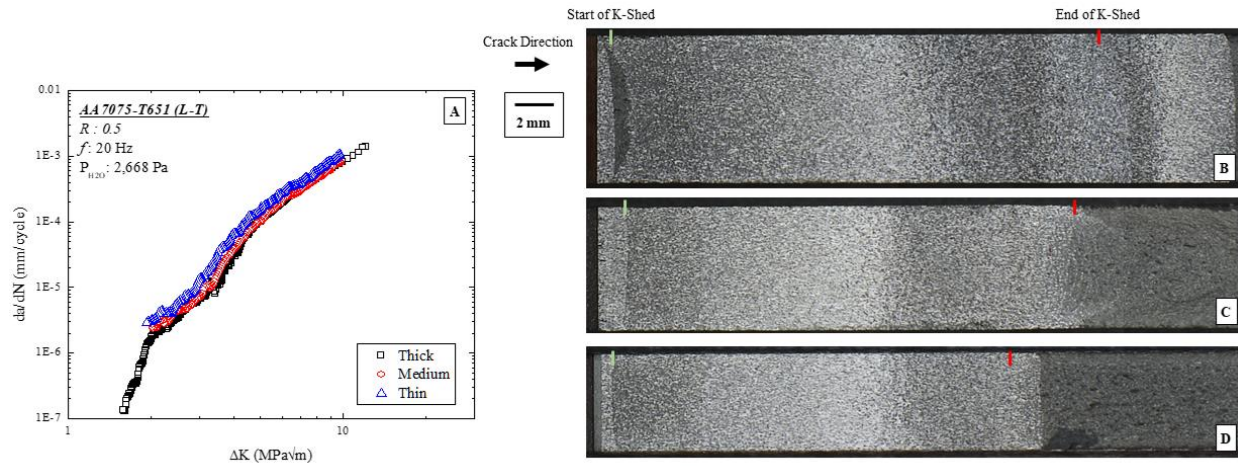
Figure 3 - (a) Fatigue crack growth rate versus ΔK relationships measured for AA7075-T651 (L-T) as a function of net section thickness using a decreasing ΔK protocol, where C = -0.08 1/mm, f = 20 Hz, and a water vapor pressure of 2,668 Pa. Overview micrographs for the thick, medium, and thin specimens are shown in (b), (c), and (d), respectively, with crack growth occurring from left to right.
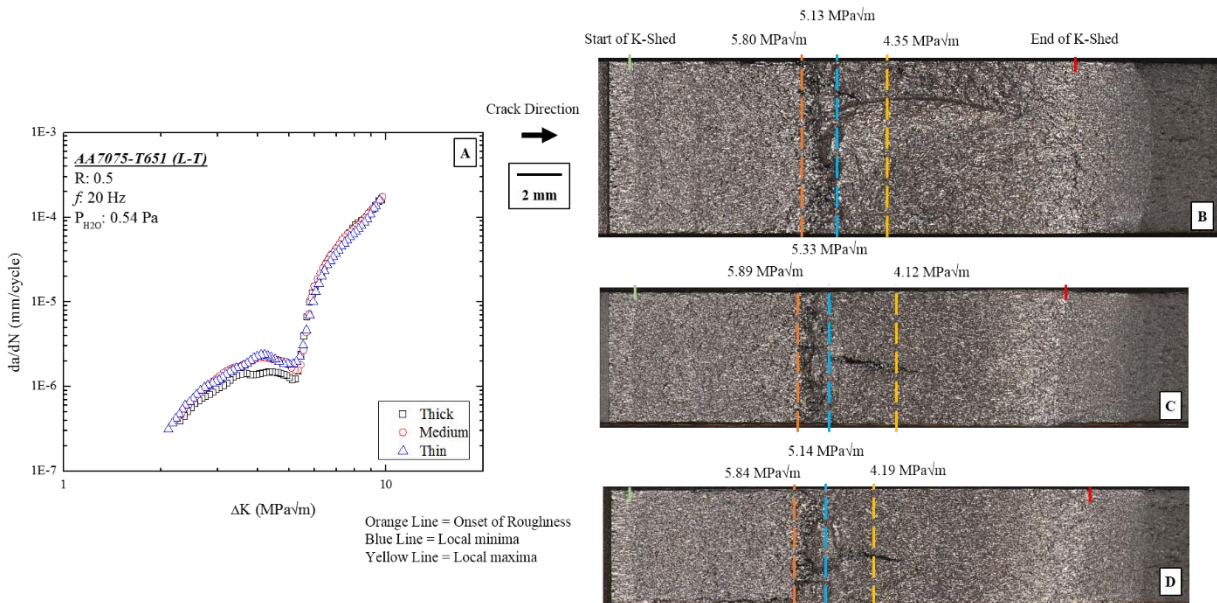
Figure 4 - (a) Fatigue crack growth rate versus ΔK relationships measured for AA7075-T651 (L-T) as a function of net section thickness using a decreasing ΔK protocol, where C = -0.08 1/mm, f = 20 Hz, and a water vapor pressure of 0.54 Pa. Overview micrographs for the thick, medium, and thin specimens are shown in (b), (c), and (d), respectively, with crack growth occurring from left to right. The orange line represents the onset of roughness as visually observed on the fractured surface. The blue line represents the first local minima or the low point of the "false threshold". The yellow line represents the first local maxima after the "false threshold" or the "spike".
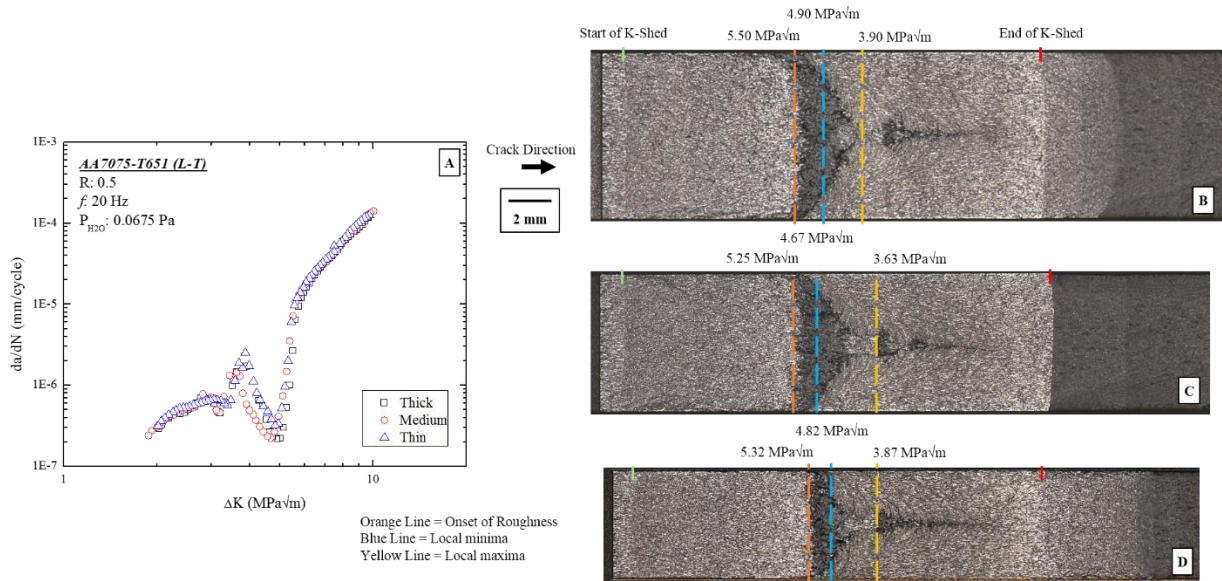
Figure 5 - (a) Fatigue crack growth rate versus ΔK relationships measured for AA7075-T651 (L-T) as a function of net section thickness using a decreasing ΔK protocol, where C = -0.08 1/mm, f = 20 Hz, and a water vapor pressure of 0.0675 Pa. Overview micrographs for the thick, medium, and thin specimens are shown in (b), (c), and (d), respectively, with crack growth occurring from left to right. The orange line represents the onset of roughness as visually observed on the fractured surface. The blue line represents the first local minima or the low point of the "false threshold". The yellow line represents the first local maxima after the "false threshold" or the "spike".

Figure 6 - (a) Fatigue crack growth rate versus ΔK relationships measured for AA7075-T651 (L-T) as a function of net section thickness using a rising ΔK protocol, using a constant load of ## KN, f = 20 Hz, and a water vapor pressure of 0.0675 Pa. Overview micrographs for the thick and medium specimens are shown in (b) and (c) respectively, with crack growth occurring from left to right. The orange line represents the onset of roughness as visually observed on the fractured surface.

2.3.2. Effect of K-rise loading protocol on the fatigue crack growth behavior

The relationship between the fatigue crack growth rate and the measured driving force using K-shed and K-rise testing protocols was done in environments with exposure parameter values of 0.03375, 0.027, and 1.9 Pa·s. The results for the K-shed and K-rise testing protocols in the 1.9 Pa·s environment is shown in Figure 7, where two general observations can be made. First, the overall behavior of the crack kinetics was similar between the two protocols except the K-shed protocol yielding higher crack growth rates for ΔK values greater than 5 MPa√m. Second, the fractography of the two testing protocols were fundamentally the same with features being similar to what is expected for a specimen undergoing EAC in a "high exposure" environment.

The results of the K-shed and K-rise testing protocols in the 0.027 Pa·s environment are shown in Figure 8, where three general observations can be made. First, the overall behavior of the crack kinetics was different between the two protocols with the K-rise protocol again yielding slightly higher crack growth rates in the near threshold region between 2 and 3 MPa√m and for ΔK values greater than 5 MPa√m. Second, TTR events were observed using both testing protocols occurring in the ΔK values between 5 and 8 MPa√m with the TTR event associated with the K-shed protocol reaching a lower minimum crack growth rate during the TTR event. Third, while the fractography for both specimens show evidence of a TTR event occurring with the middle of the specimen cracking at a slower rate than the edges during the phenomena, but the nature of these TTR events appear different between the two protocols.

The TTR event occurring with the K-shed protocol started with a clear mechanism change to a rougher crystallographic type fracture that happens across the entire width of the specimen. At some point the rougher crystallographic fracture reverts back to a flat transgranular fracture mode, which appears to begin at the edges of the specimen and advances at an angle toward the center of the specimen. In the center of the specimen after the rough crystallographic cracking area, displays evidence of ductile fracture. In contrast, the clear mechanism change to a rougher crystallographic type fracture appears first in the center of the specimen and forms periodic bands, which form on larger areas of the specimen width as the crack advanced and ductile fracture occurring in-between the bands.

In Figure 9, the results for the K-shed and K-rise testing protocols in a 0.003375 Pa·s environment are displayed and similar general observations can be made as the 0.027 Pa·s

environment specimens. The results of the K-shed and K-rise protocols in the 0.003375 Pa·s environment are displayed in Figure 9, where three general observations can be made. First, the overall behavior of the crack kinetics was slightly different between the two protocols with the K-shed protocol yielding a slightly higher crack growth rate for most of the reported driving forces. Second, multiple TTR events were observed for both testing protocols occurring in the ΔK values between 3 and 6 MPa√m with the first TTR event associated with the K-shed protocol reaching a lower minimum crack growth rate than what was observed in any of the TTR events associated with the K-rise protocol. Third, the TTR events had similar characteristics as was described for the 0.027 Pa·s specimens except the features are more pronounced. These previously discussed characteristics of the TTR events can be observed in Figure 10, where scanning electron microscope (SEM) images showing select areas of the specimen tested using the K-rise protocol in the 0.003375 Pa·s environment, which further displays the changes in cracking mechanism occurring during the fatigue crack advancement across the specimen. From Figure 10, the roughness of the crack wake surface can be seen, with the rougher surfaces being indicative of slower cracking mechanisms. These areas of crystallographic cracking are generally preceded and flanked by a flat transgranular cracking, and proceeded by ductile fracture both of which are indicative of a faster cracking mechanisms.
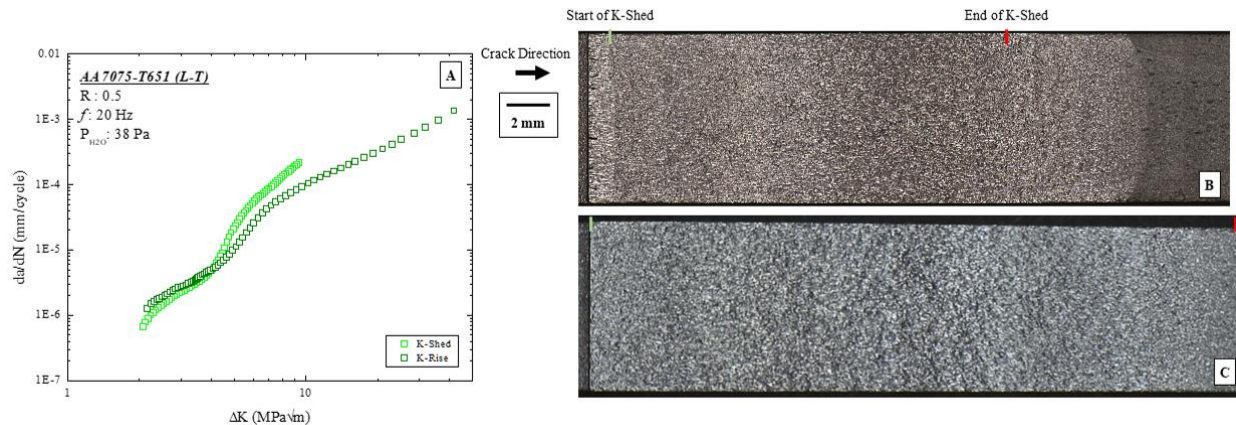
Figure 7 - (a) Fatigue crack growth rate versus ΔK relationships measured for AA7075-T651 (L-T) as a function of loading protocol (K-shed vs K-rise) using the same BNET, where f = 20 Hz and a water vapor pressure of 38 Pa. The K-shed protocol used a C = -0.08 1/m and the K-rise protocol using a constant load. Overview micrographs for the K-shed protocol and the K-rise protocol specimens are shown in (b) and (c) respectively, with crack growth occurring from left to right.
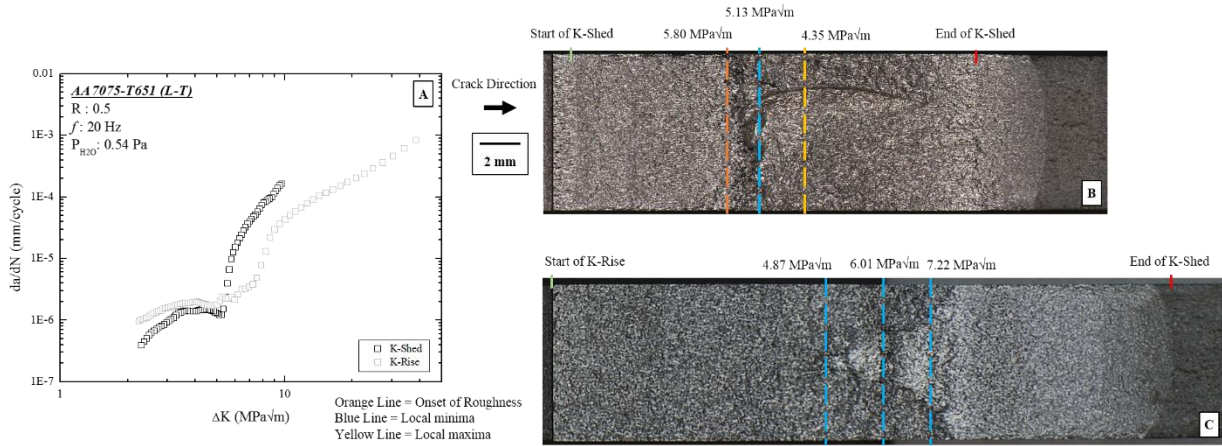
Figure 8 - (a) Fatigue crack growth rate versus ΔK relationships measured for AA7075-T651 (L-T) as a function of loading protocol (K-shed vs K-rise) using the same B_{NET}, where f = 20 Hz and a water vapor pressure of 0.54 Pa. The K-shed protocol used a C = -0.08 1/mm and the K-rise protocol using a constant load. Overview micrographs for the K-shed protocol and the K-rise protocol specimens are shown in (b) and (c) respectively, with crack growth occurring from left to right. For the K-shed specimen, the orange line represents the onset of roughness as visually observed on the fractured surface. The blue line represents the first local minima or the low point of the "false threshold". The yellow line represents the first local maxima after the "false threshold" or the "spike". For the K-rise specimen the blue lines represent each of the local maxima before the "false threshold" minima.
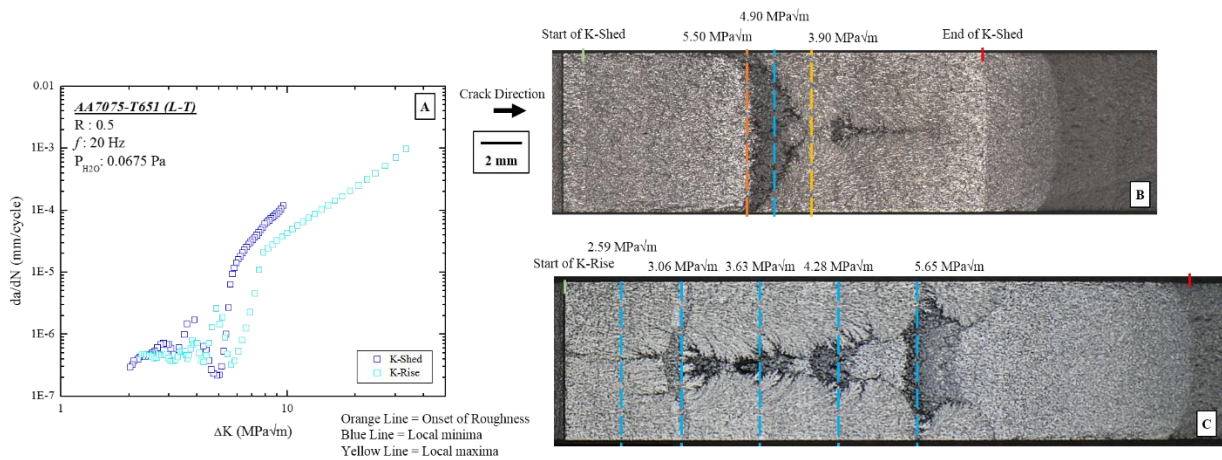
Figure 9 - (a) Fatigue crack growth rate versus ΔK relationships measured for AA7075-T651 (L-T) as a function of loading protocol (K-shed vs K-rise) using the same B_{NET}, where f = 20 Hz and a water vapor pressure of 0.0675 Pa. The K-shed protocol used a C = -0.08 1/mm and the K-rise protocol using a constant load. Overview micrographs for the K-shed protocol and the K-rise protocol specimens are shown in (b) and (c) respectively, with crack growth occurring from left to right. For the K-shed specimen, the orange line represents the onset of roughness as visually observed on the fractured surface. The blue line represents the first local minima or the low point of the "false threshold". The yellow line represents the first local maxima after the "false threshold" or the "spike". For the K-rise specimen the blue lines represent each of the local maxima before the "false threshold" minima.
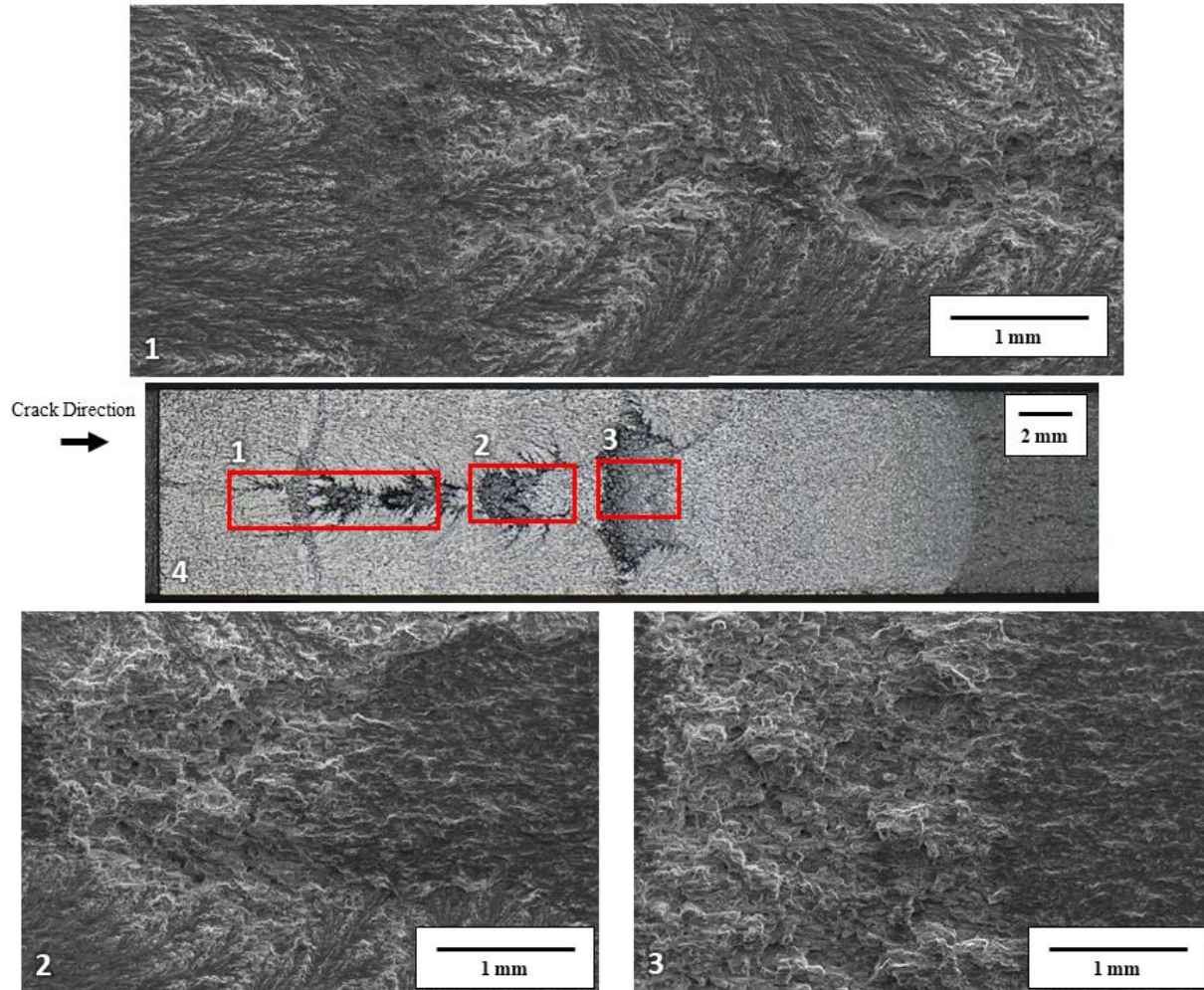
Figure 10 - (1) An SEM image showing the changes in cracking mechanisms, particularly from a flat transgranular mechanism to a rougher crystallographic mechanism happening in the first and second TTR event using the K-rise protocol in a 0.003375 Pa·s environment. (2) An SEM image showing the changes in the cracking mechanism from a rough crystallographic type to a ductile type fracture occurring in the third TTR event using the K-rise protocol in a 0.003375 Pa·s environment. (3) An SEM image of the final TTR event occurring with the K-rise protocol in a 0.003375 Pa·s environment displaying the mechanism change from a rough crystallographic type to a flat transgranular type.

2.4. Discussion

The presented fatigue crack growth rate versus applied stress intensity factor range relationships (Figures 1-6) demonstrates that variations in specimen thickness ranging from 7.62 ± 0.51 mm to 4.92 ± 0.25 mm do not tangibly modify the fatigue crack behavior of AA7075-T651 across several environments with a variety of partial water vapor pressures spanning $< 1.33 \times 10^{-6}$ to 2,668 Pa. These observations are consistent with the strong similarities observed in the fracture morphology for each of the specimens as a function of P_{H2O}/f. Conversely, a comparison of two

different loading protocols with one using a shedding load resulting in a decreasing ΔK, and the other using a constant load yielding a rising ΔK (Figures 7-9), revealed a slight difference due to a change in loading protocol on the fatigue crack behavior of AA7075-T651. Based on these results, the following section will: (1) discuss the interactions of the fracture surface and water vapor due to the transport distance and the nature of the roughness created by the perspective loading protocol, (2) the cracking mechanisms responsible for the TTR effect and (3) the implications of the study for the generation of crack growth rate data use in LEFM modeling.

2.4.1. Fracture surface analysis of variable thickness K-shed tests

For intermediate exposure environments the water vapor at the crack tip is hypothesized to be limited by the molecular flow (Knudsen diffusion) of water from the bulk environment to the crack tip, where flow to the crack tip depends on a number of factors.[3] One of the factors affecting the molecular flow of water vapor molecules from the bulk environment to the crack tip is impedance caused by interactions with the crack walls. Specifically, the chance for an interaction event increases with increasing distance between the bulk environment and the crack tip as well as increasing magnitude of crack wake surface roughness.[3] These TTR events are postulated to be a product of the self-perpetuating process of increasing crack wake surface roughness due to the starvation of water to the center of the specimen at the crack tip, further perpetuating the changing of the flat transgranular cracking to a rougher faceted slip band cracking (SBC).[3] Thus if the transport distance was the limiting factor for the TTR event phenomena then decreasing the thickness of the specimen would decrease the area of crack wake surface and subsequently the impedance to the molecular flow between the crack center and the bulk environment.

The results of this study shown in Figure 1, first indicate in the absence of environment (UHV) the significant changes in the geometry of the specimen are adequately accounted for by the K-solution provided in ASTM E647 for C(T) specimens.[29] Furthermore, significant reduction in thickness to specimens exposed to intermediate exposure environments exhibited little to no change to the character of the TTR event in both the fatigue growth kinetics and the corresponding fractured surface for each of the specimens as shown in Figures 4-6. These lack of differences in the TTR event despite large changes in transport distance, suggests the continuation of cracking below the vacuum threshold level is from the formation of the two new semi-elliptical crack fronts beginning on the edges of the specimen, where full exposure to the bulk environment occurs.

2.4.2. Fracture surface analysis for the K-rise testing

Previous work done by Burns et al. examined different shed loading protocols, that utilized either a constant R or a constant K_{max} and the impact they had on the TTR events occurring in intermediate exposure environments.[3] The Burns et al. study demonstrated that the R-ratio impacted the ΔK value and P_{H2O}/f at which the TTR occurred however all protocols examined had a TTR event phenomena.[3] In each case the onset of the TTR corresponded with the onset of rougher cracking morphology typically seen with SBC.[3] It was postulated testing utilizing a rising ΔK protocol could create a different crack wake fracture surface morphology, which may affect the impedances such as crack closure and surface roughness to the water vapor molecular flow from the bulk environment to the center of the crack tip.[3]

An examination of the fracture surfaces of the K-shed specimens exhibited a change in cracking mechanism to a crystallographic type fracture that appears across the entire width of the specimen. In contrast, the change to a crystallographic type fracture in the K-rise specimens appears first in the center of the sample and is flanked by the same flat transgranular cracking that proceeded it. These differences suggests the onset of the change in crack mechanism is strongly influenced by the driving force given an intermediate exposure environment or lower. If the loading history is the limiting factor for the TTR event phenomena then changing the loading protocol from a K-shed to a K-rise would affect the extent of the area covered by SBC and thus could be influenced by how the crack growth rate changes as the crack proceeds out of the roughened area. Particularly, an acceleration of crack growth rate in the intermediate driving force range could potentially lessen the severity or outright eliminate the TTR event from occurring.

Figures 8 and 9 show the impact a change in loading protocol had on the crack kinetics and more specifically the TTR event. However, the results of this study provide evidence suggesting the loading protocol impacts how the TTR event begins, but does not significantly change the nature of the TTR event, thus the loading protocol does not govern the nature of this phenomena observed in the fatigue crack growth behavior. An examination of the fracture surfaces yields a probable crack progression, which is shown in Figure 11 for the two different loading protocols used in this study. As previously described, both protocols precede the TTR event with a straight crack front, observed at position 1, but the onset of surface roughness occurs in the center of the specimen first for the K-rise protocol and on the edges of the specimen for the K-shed protocol as

observed at position 2. This study has demonstrated the appearance of surface roughness correlates with a slower cracking mechanism causing the affected areas of the crack front to slow down relative to the areas cracking with a flat transgranular cracking mechanism. After a relatively short distance of crack growth seen with position 3 the edges of the specimen utilizing the K-shed protocol transition back to a flat transgranular cracking mechanism causing these portions of the crack front to grower faster creating an uneven crack front, similarly to what was observed with the K-rise protocol. Eventually, the driving force at the center of the crack for the K-rise protocol becomes high enough that the remaining attached ligament of material undergoes a rapid failure mechanism. This is confirmed by the SEM images shown in Figure 10 and is the cause for the "spikes" observed in the crack growth kinetics, thus beyond position 3 the characteristics of the TTR event are similar between the two different loading protocols.

The results of this study provide evidence to suggest the loading protocol, whether it be a rising or shedding, impacts how the TTR event begins, but does not significantly change the nature of the TTR event, thus the loading protocol does not govern the nature of the fatigue crack growth behavior. Instead, the data suggests the existence of a specific combination of driving force range (3-6 MPa√m) and bulk water pressure environment range (intermediate exposure or lower) for which the SBC mechanism is preferred.
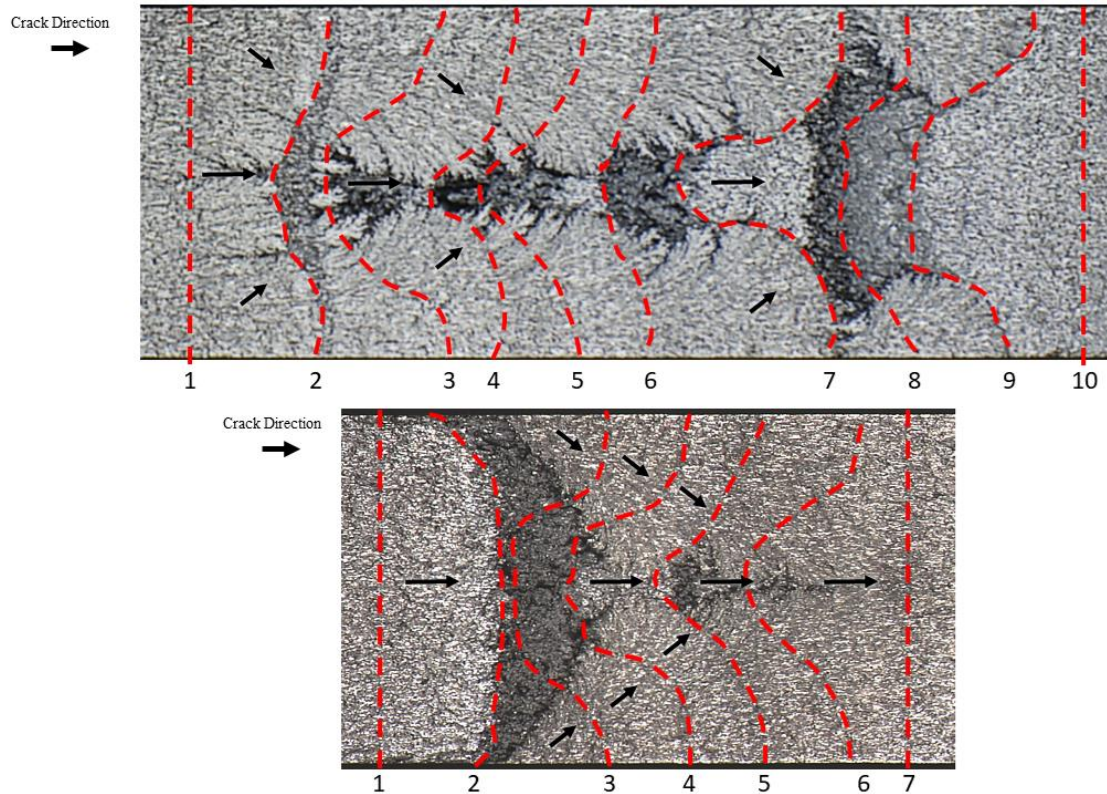
Figure 11 - An illustration of the crack front progression overlaid on the fractography for both the K-rise (top) and K-shed (bottom) protocol for the 0.003375 Pa·s environmental condition.

2.4.3. Transition of cracking mechanism to SBC

The data from this study strongly suggest a correlation of the TTR phenomena and the SBC mechanism, therefore it is necessary to understand why this cracking mechanism occurs. The results of the UHV data shown in Figure 1 of this study suggests SBC is an intrinsic mechanism for cracking at threshold and the near-threshold regime, which could be explained by how materials accommodate fatigue damage via the emission of additional dislocations or a cleavage-like fracture at the crack tip. At threshold, dislocations near the crack tip move a distance away, which is dependent on the applied driving force, on a given slip system toward some barrier of movement, likely to be a precipitate. Initially, the emission of dislocations is predicted by a Peierls-type analysis previously done, which indicates the activation energy for dislocation emission is substantially lower than a cleavage-type rupture of the slip plane.[35] Further cycling and consequently the emission of additional dislocations push previously created dislocations on the slip planes closer to the barriers, where at low driving forces like those found at and near threshold, have insufficient amounts of energy to move dislocations passed the barriers via by-pass or shear.[35]

Therefore, as the accumulation of dislocations becomes significantly high, the dislocation pile-up creates an instability between the barrier and dislocations resulting in the release of back stress allowing for the crack tip to step forward via a cleavage-type cracking mechanism to a new quasi-equilibrium position.[36] In contrast, at sufficiently high driving forces found beyond the near-threshold regime, the dislocations have the energy necessary to move passed the barrier via by-pass or shear rather than accumulate near the crack tip allowing for further damage accumulation via emission.[35] The appearance of a flat transgranular cracking mechanism at the higher driving force regions of the UHV specimens indicates the existence of a threshold value for this non-crystallographic type cracking.

Experimental results of fatigue experiments in high exposure environments displayed in Figures 2 and 3 indicate no SBC type mechanism for all driving force values suggesting sufficient amounts of hydrogen may increase the ability for dislocations to move away from the crack tip, thus overcoming movement barriers. The notion of hydrogen increasing the proclivity of cross-slip was observed in a study by Harris et al., which did provide evidence suggesting such in a peak-aged nickel alloy charged with hydrogen.[37] However, more examples of literature suggest hydrogen increases the planarization of slip potentially indicating a potential increased propensity for shear rather than by-pass may be possible.[38–43] The results of fatigue experiments in the intermediate exposure environments exhibited in Figures 4-6, indicated a hydrogen-enabled transgranular cracking occurring below the threshold driving force value found at UHV for this material similar to what was observed in the high exposure environment experiments. The sub-threshold cracking may also suggest hydrogen is decreasing the activation energy for dislocation emission from the crack tip, thus allowing for the continued accumulation of damage below threshold enabling further crack advancement. However, without the additional enhancement of the ability of dislocations to overcome movement barriers the accumulation of dislocations near the crack tip would eventually lead to a likely cleavage-like fracture.[35]

2.4.4. Implications to the application of growth rate data for LEFM modeling

The results of this study clearly demonstrate the TTR phenomena is an intrinsic material response to an intermediate driving force while exposed to an intermediate or low exposure environment as a reduction of specimen thickness and a change in the loading protocol had little to no impact on the phenomena. This fact creates complications to the use of growth rate data in

LEFM modeling as the resulting transitions in cracking mechanism create uneven crack fronts, which challenge the notion of similitude between laboratory testing and engineering applications. To accurately apply the growth rates associated with this phenomenon for LEFM modeling would require a better understanding of two fronts; 1) An more accurate account of the differences in driving force across the entire length of the crack front than given with the traditional K solution due as these minor differences lead to the uneven crack front observed and 2) Develop a better understanding of the molecular flow of water molecules from the bulk environment to the crack tip to more accurately depict the exposure environment as illustrated by a Zhang et al. study.[44] Alternatively, a conservative approach of a linearly extrapolating data over the TTR event, thus providing an approximation of crack growth data that not only maintains similitude, but can be used in LEFM models.

2.5. Conclusions

The influence of molecular transport distance and the loading protocol on the fatigue crack growth behavior of a legacy aerospace alloy AA7075-T651 at multiple simulated service environments was systematically examined, providing many insights into the fatigue cracking behavior of AA7075-T651 in high altitude environments:

1. The mass transport distance due to the thickness of the sample was found to have a minimal to no impact on the fatigue cracking behavior.

2. The TTR events occurring during fatigue cracking in the intermediate water environments were observed using both a K-shed and a K-rise testing protocol thus these events are not a product of the testing history.

3. The data suggests the observed cracking behavior is due to the intrinsic properties of the material rather than an artifact of testing protocol or specimen geometry.

2.6. Suggestions for future study

Experiments from this study completed in an UHV environment indicates the mechanics driven cracking mechanisms at play in AA7075-T651. In the near-threshold regime and intermediate driving forces an SBC type cracking mechanism is dominate, while at high driving forces a flat transgranular type cracking is the dominate mechanism. This behavior can be explained by the higher driving forces promoting activities such as cross-slip and therefore by-

pass of the precipitates by dislocations that enable transgranular cracking. This change in mechanism is highly sensitive to the driving force when fatigue is occurring in an intermediate exposure or lower environment and is the catalyst for the TTR event. Therefore identifying the ΔK across the entire crack front via a mechanics driven analysis would allow for a better understanding of the evolution of the irregular crack front, which is needed for any application to LEFM modeling. Additionally, there remains a need to understand the mechanism for how specific parameters are affecting the environment that interacts with the crack tip. Work toward this end was previously described with the study done by Zhang et al., which describes the initial attempts to model the effects of surface roughness, R-ratio, loading frequency, crack opening displacement and specimen thickness has on the crack tip water vapor pressure.[44] Within "intermediate exposure" environments, the fatigue crack behavior is similar to what is observed with the UHV environment, however at the vacuum threshold driving force value an additional transition in cracking mechanism occurs to the flat transgranular mechanism similar to what was observed at high driving force values. The exact mechanisms to why this additional change in cracking mechanism occurs isn't fully understood. To attempt to understand this process characterization utilizing the protocol described in chapter 4 examining the sub-crack surface of the sub-threshold cracking region could provide insights into what the cracking behavior is in this region. Developing this further understanding would lead to more informed research on how to prevent or mitigate the fatigue damage in low P_{H2O} environments.

2.7. Acknowledgements

2.8. References

1.   Starke Jr., E. A. & Williams, J. C. Microstructure and the Fracture Mechanics of Fatigue Crack Propagation. in *Perspectives and Directions (20th Symposium)* (eds. Wei, R. P. &

Gangloff, R. P.) 184–205 (American Society for Testing and Materials, 1989).

2.   Gangloff, R. P. Environment sensitive fatigue crack tip processes and propagation in aerospace aluminum alloys. *Fatigue* **2**, 3401–3433 (2002).

3.   Burns, J. T. *et al.* Effect of water vapor pressure on fatigue crack growth in Al – Zn – Cu – Mg over wide-range stress intensity factor loading. *Eng. Fract. Mech.* **137**, 34–55 (2015).

4.   Bonakdar, A., Wang, F., Williams, J. J. & Chawla, N. Environmental Effects on Fatigue Crack Growth in 7075 Aluminum Alloy. *Metall. Mater. Trans. A* **43A**, 2799–2809 (2011).

5.   Wei, R. P. & Gao, M. Reconsideration of the Superposition Model for Environmentally Assisted Fatigue Crack Growth. *Scr. Metall.* **17**, 959–962 (1983).

6.   Pao, P. S., Gao, M. & Wei, R. P. Environmentally assisted fatigue-crack growth in 7075 and 7050 aluminum alloys. *Scr. Metall.* **19**, 265–270 (1985).

7.   Ruiz, J. & Elices, M. Effect of water vapour pressure and frequency on fatigue behaviour in 7017-t651 aluminium alloy plate. *Acta Mater.* **45**, 281–293 (1997).

8.   Davidson, D. L. & Lankford, J. The Effects of Water Vapor on Fatigue Crack Tip Mechanics in 7075-T651 Aluminum Alloy. *Fatigue Fract. Eng. Mater. Struct.* **6**, 241–256 (1983).

9.   Gupta, V. K., Gangloff, R. P. & Agnew, S. R. Diffraction characterization of microstructure scale fatigue crack growth in a modern Al-Zn-Mg-Cu alloy. *Int. J. Fatigue* **42**, 131–146 (2012).

10.   Davidson, D. . & Lankford, J. The Effects of Aluminum Alloy Microstructure on Fatigue Crack Growth. *Mater. Sci. Eng.* **74**, 189–199 (1985).

11.   Sanders, T. H. & Stanley, J. T. Review of Fatigue and Fracture Research on High-Strength Aluminum Alloys. *Am. Soc. Met.* 467–522 (1979).

12.   Chanani, G. R. *Fundamental Investigation of Fatigue Crack Growth Retardation in Aluminum Alloys*. (1976).

13.   Truckner, W. G., Staley, J. T., Bucci, R. J. & Thakker, A. B. *Effect of Microstructure on Fatigue Crack Growth of High-Strength Aluminum Alloys*. (1976).

14. Lynch, S. P. Mechanisms of Fatigue and Environmentally Assisted Fatigue. *ASTM Int.* **675**, 174–213 (1979).

15. Nix, K. J. & Flower, H. M. The micromechanisms of fatigue crack growth in a commercial Al-Zn-Mg-Cu alloy. *Acta Metall.* **30**, 1549–1559 (1982).

16. Burns, J. T., Jones, J. J., Thompson, A. W. & Warner-Locke, J. S. Fatigue crack propagation of aerospace aluminum alloy 7075-T651 in high altitude environments. *Int. J. Fatigue* **106**, 196–207 (2018).

17. Ro, Y., Agnew, S. R. & Gangloff, R. P. Effect of environment on fatigue crack wake dislocation structure in Al-Cu-Mg. *Metall. Mater. Trans. A Phys. Metall. Mater. Sci.* **43**, 2275–2292 (2012).

18. Piascik, R. S. & Gangloff, R. . Environmental fatigue of an Al-Li-Cu alloy: part I. Intrinsic crack propagation kinetics in hydrogenous environments. *Metall. Trans. A* **22**, 2415–2428 (1991).

19. Adminstration, N. O. and A. A. (NOAA), (NASA), N. A. and S. A. & (USAF), U. S. A. F. *U.S. Standard Atmosphere, 1976*. (1976).

20. Saxena, A. & Muhlstein, C. Fatigue Crack Growth Testing. in *ASM Handbook: Fatigue and Fracture, Volume 19* 168–184 (1996). doi:https://doi.org/10.31399/asm.hb.v19.a0002360.

21. McEvily, A. J. Fatigue Crack Tresholds. in *ASM Handbook: Fatigue and Fracture, Volume 19* 134–152 (1996). doi:https://doi.org/10.31399/asm.hb.v19.a0002357.

22. Jones, J. L., Mcmurtrey, M. D., Brown, L. B. & Burns, J. T. The e ff ect of crack wake roughness on the environmentally assisted fatigue behavior of an aerospace Al-alloy in low moisture environments. *Eng. Fract. Mech.* **199**, 343–357 (2018).

23. Brown, L. B., Jones, J. L., Warner, J. S. & Burns, J. T. Effect of low temperature , low water vapor pressure environments on the fatigue behavior of an Al-Li aerospace alloy. *Int. J. Fatigue* **148**, 106215 (2021).

24. Papazian, J. *et al.* DARPA/NCG structural integrity prognosis system. *DARPA* **HR0011-04**, (2009).

25. B209-14 Standard Specification for Aluminum and Aluminum-Alloy Sheet and Plate.

ASTM Int. (2014) doi:https://doi.org/10.1520/B0209-14.

26. Burns, J. T., Larsen, J. M. & Gangloff, R. P. Driving forces for localized corrosion-to-fatigue crack transition in Al-Zn-Mg-Cu. *Fatigue Fract. Eng. Mater. Struct.* **34**, 745–773 (2011).

27. Payne, J., Welsh, G., Christ, R. J., Nardiello, J. & Papazian, J. M. Observations of fatigue crack initiation in 7075-T651. *Int. J. Fatigue* (2010) doi:10.1016/j.ijfatigue.2009.06.003.

28. E647-15e1 Standard Test Method for Measurement of Fatigue Crack Growth Rates. *ASTM Int.* 1–49 (2015) doi:10.1520/E0647-15E01.2.

29. E647-15e1. Standard Test Method for Measurement of Fatigue Crack Growth Rates. *ASTM B. Stand.* 1–49 (2016) doi:10.1520/E0647-15E01.2.

30. Donald, J. K. Introducing the compliance ratio concept for determining effective stress intensity. *Int. J. Fatigue* **19**, 191–195 (1997).

31. Donald, J. K., Bray, G. H. & Ralph, W. an Evaluation of the Adjusted Compliance Ratio Technique. 674–695 (1999).

32. Newman, J., Schneider, J., Daniel, A. & McKnight, D. Compression pre-cracking to generate near threshold fatigue-crack-growth rates in two aluminum alloys. *Int. J. Fatigue* **27**, 1432–1440 (2005).

33. Standard Specification for Reagent Water 1. *ASTM Int.* **i**, 1–6 (2019).

34. Li, D., Gangloff, R. P., Bray, G. H., Glazov, M. V. & Rioja, R. J. Aging dependent intrinsic fatigue crack propagation in AA2024. in *Materials Solutions Conference* 105–118 (2001).

35. Shastry, V. & Anderson, P. M. Interaction between emission and cleavage at crack tips. *Philos. Mag. A* **75**, 771–789 (1997).

36. Gerberich, W. W., Davidson, D. L., Chen, X. F. & Lee, C. S. Dislocation dynamics of crack-tip processes-frequency observations and theoretical modeling. *Eng. Fract. Mech.* **28**, 505–518 (1987).

37. Harris, Z. D., Bhattacharyya, J. J., Ronevich, J. A., Agnew, S. R. & Burns, J. T. The combined effects of hydrogen and aging condition on the deformation and fracture behavior of a precipitation-hardened nickel-base superalloy. *Acta Mater.* **186**, 616–630 (2020).

38.   Ferreira, P. J., Robertson, I. M. & Birnbaum, H. K. Hydrogen effects on the character of dislocaitons in high-purity aluminum. *Acta Mater.* **47**, 2991–2998 (1999).

39.   Wen, M., Fukuyama, S. & Yokogawa, K. Hydrogen-affected cross-slip process in fcc nickel. *Phys. Rev. B* **69**, (2004).

40.   Robertson, I. M. The effect of hydrogen on dislocation dynamics. *Eng. Fract. Mech.* **68**, 671–692 (2001).

41.   Robertson, I. M. *et al.* Hydrogen Embrittlement Understood. *Metall. Mater. Trans. B* (2015) doi:10.1007/s11663-015-0325-y.

42.   Lynch, S. Hydrogen embrittlement phenomena and mechanisms. *Corros. Rev.* **30**, 105–123 (2012).

43.   Delafosse, D. Hydrogen effects on the plasticity of face centered cubic (fcc) crystals. in *Gaseous Hydrogen Embrittlement of Materials in Energy Technologies* 247–285 (2012). doi:https://doi.org/10.1533/9780857095374.2.247.

44.   Zhang, W. *et al.* CFD analysis of microchannel flows for applications in environmental structure cracking. *AIAA Scitech 2020 Forum* **1**, 1–11 (2020).

Chapter 3 – Effect of low temperature on fatigue in an UHV environment

3.1. Overview

Studies focused on the effects of low temperature on fatigue behavior of aluminum alloys have been performed,[1,2,11–15,3–10] specifically with 7xxx series aluminum alloys (or equivalent),[1,2,19,4,6,10,12,13,16–18] where generally a decrease in crack growth rates or an increase in fatigue life correlating with a decrease in temperature is observed, but various explanations have been given for the observed change in behavior. Particularly, a number of studies note at higher driving forces the fatigue crack growth rates were either higher or the same at low temperatures as compared to complementary experiments conducted around room temperature.[1,4,10,12,16–18,20] A few studies attributed this change in fatigue behavior to a change in the mechanical properties of the material,[21] with some suggesting specifically a reduction in fracture toughness[1,3,5,10] and an increase in yield strength or resistance to plastic deformation.[3–5,16] Additionally, the work by Cox et al. and Magda observed a change in the fracture mechanism from a ductile type fracture to a quasi-cleavage type occurring at temperatures below -28°C.[4,10] Explicitly, the Magda study observed a change in fracture mechanism that came with secondary crack formation between some of the facets with the formation of the secondary cracking found around inclusions and the fine precipitates found in this material, but the mechanism for the secondary cracks was not clear.[4] Additional studies with observations of fracture mechanism changes in low temperatures have attributed the mechanism change as the reason for the fatigue behavior differences.[12,18,20] Similarly, the work by Ostash et al. and Pettit et al. also observed a quasi-cleavage type fracture, with the Pettit et al. study observing this type of fracture at temperatures of -7°C and below.[18,20] Distinctly, the Pettit et al. work postulated this quasi-cleavage fracture indicated the onset of an intergranular failure mode believed to become dominate at the lower temperatures.[18]

One common issue obfuscating the results from these low temperature studies is how the low temperatures are achieved. Generally, low temperatures are achieved by introducing liquid nitrogen vapors to an environmental chamber where the fatigue cracking will occur without expelling existing water vapor within the chamber. Low temperatures achieved utilizing liquid nitrogen vapors without removing the pre-existing environment within the chamber contains non-negligible amounts of water vapor. This pre-existing water vapor forms ice on surfaces within the chamber, which from the Clausius-Clapeyron relationship (specifically the Goff-Gratch equation

used for temperatures ranging from -100°C to 0°C) the partial pressure of water vapor above the ice formed at these temperatures has been shown to be significant and can influence the fatigue behavior in aluminum alloys.[22–24] This exact issue was acknowledged by the authors of the Cox et al. and Moreto et al. studies and in the case of the Moreto et al. the reduction of the partial pressure of water vapor was cited as the major factor for the observed difference in the fatigue crack growth rates between the low temperature and room temperature experiments.[10,16]

Furthermore, an observed rougher crack wake surface in the near threshold region with specimens fatigue cracked in low temperature environments have been reported in other materials leading to the hypothesis of crack closure being responsible for or at least contributing to the changes in crack growth behavior observed, but often closure was observed in studies utilizing a small stress ratio, R < 0.5 making it difficult to discern if the observed changes are the change change in cracking mechanism or a testing artifact.[4,25–27] The study by Liaw et al. concluded low temperature fatigue crack growth rates to be insensitive to R, but this was not the case for the study conducted by Esaklul et al. where an observed change in the fracture mechanism to cyclic cleavage was observed to decrease crack growth rates even at high R values where closure effects would be minimal.[25,26]

The objective of this study is to isolate and assess the influence of low temperatures, specifically in the range of temperatures experienced by aircraft at high altitudes on the fatigue crack growth behavior of the aerospace alloy AA7075-T651. Fatigue crack propagation experiments using a constant decreasing driving force protocol as described in the ASTM E647 standard with an UHV environment and each specimen cooled to a pre-determined temperature ranging from 23°C to -65°C. The implications and results of these findings is discussed and interpreted in the context of fracture mechanics.

3.2. Experimental Methods

3.2.1. Materials

All experiments were conducted on AA7075-T651 procured in the form of a 50.8-mm thick plate. This material heat was used in a prior interdisciplinary multiscale airframe fatigue prognosis study to approximate the composition of AA7075-T6 employed in older aircraft.[28] Though this alloy meets the compositional requirements for AA7075, it contains an elevated iron and silicon content relative to modern AA7075 heats.[29] The reported composition of the tested material heat

is listed in Table 1 shown in chapter 1 and detailed analyses of the alloy microstructure and mechanical properties are presented elsewhere.[19,28,30,31]

3.2.2. Fatigue crack growth experiments and characterization

Compact tension [C(T)] specimens with a width (W) of 50.8 ± 0.51 mm were extracted from the plate in the L-T orientation (loading axis parallel to the rolling direction of the plate, crack growth occurring in the transverse direction), such that the C(T) specimen mid-thickness was located at a depth of ≈ 8.5 mm from the plate surface (*i.e.*, S/6 location, where S is the plate thickness). The specimen thickness (B) was 7.62 mm ± 0.51 mm. The specimens were machined with a starter notch depth (a_0) of 10.7 ± 0.51 mm ahead of the load line. Each specimen was fatigue pre-cracked in laboratory air using a constant amplitude loading protocol with a stress ratio (R) of 0.1 and frequency (*f*) of 5 Hz, with the maximum load (P_{max}) selected such that maximum stress intensity (K_{max}) reached 10 MPa√m after 1 mm of crack propagation (typical P_{max} was ~3.4 kN).

All experiments in the current study were completed under ultra-high vacuum (UHV); (defined herein as a pressure less than $3\text{x}10^{-6}$ Pa) using a mechanical load frame integrated into a copper gasket-sealed stainless steel vacuum chamber. After the chamber was evacuated to UHV, specimens were cooled to the test temperature (ranging from 23ºC to -65ºC) using an expander unit attached to a water-cooled helium compressor. A copper plate with attached braiding was bolted to the coldhead of the expander unit, with the copper braiding ends clamped onto the C(T) specimen both above and below the crack plane. A DT-670B silicon diode thermocouple was placed in contact with the C(T) specimen using aluminum tape, thereby allowing for the specimen temperature to be directly monitored throughout each experiment. With this setup, fatigue experiments could be held within ±0.5ºC of the desired temperature.

For experiments conducted below 23ºC, as the specimen neared the targeted test temperature, a constant amplitude loading protocol ($P_{max} = 1$ kN, R = 0.5) was performed at 20 Hz to allow the temperature to stabilize while the specimen was being actively cycled. Once the temperature was fully stabilized under active loading, the modulus of elasticity used for the compliance-based crack length measurements was adjusted to compensate for temperature-induced modifications. This adjustment was performed until the final pre-crack length was obtained and then the decreasing stress intensity factor range (ΔK-shed protocol) was initiated. For

testing executed at 23ºC, the modulus of elasticity was not adjusted from the value established prior to the fatigue pre-cracking in laboratory air.

Each ΔK-shed experiment was performed at R = 0.5 and f = 20 Hz. ΔK was programmed to decrease as a function of instantaneously measured crack length (a) according to $\Delta K = \Delta K_o e^{C(a-a_o)}$, where the initial ΔK ($\Delta K_o$) was 10 MPa√m, initial crack length (a_o) corresponded to the crack length recorded at the end of the pre-crack protocol, and the K-gradient (C) was -0.08 mm^{-1} in accordance with ASTM E647.[32] Testing was stopped when either da/dN was consistently less than 1.0x10^{-7} mm/cycle or the R^2 value for a linear fit to the measured compliance was less than 0.8. Crack growth rates were calculated using the 7-point (n = 3) incremental polynomial method described in ASTM E647, while closure influences were monitored via the calculation of an effective ΔK using the adjusted compliance ratio (ACR) method.[33–35] After the completion of each experiment, the actual pre-crack and final crack length were measured using a FEI Quanta 650-FEG scanning electron microscope (SEM) to linearly correct the compliance-based crack length measurements. The compliance-based pre-crack and final crack length were generally found to be within 1% and 3%, respectively, of the post-test measured values. Fracture surface features were evaluated using the same previously mentioned SEM.

3.3. Results

The measured fatigue crack growth rate versus ΔK relationships for AA7075-T651 under UHV conditions as a function of temperature are shown in Figure 12; the experiment at -65ºC was truncated early due to facilities-related challenges. Examination of these data demonstrates that the fatigue crack growth rate for all tested temperatures appears to coalesce for both ΔK ≳ 8 MPa√m and for ΔK ≲ 5 MPa√m. However, between these two regions, a significant difference in the observed fatigue crack growth versus ΔK relationships are observed as a function of temperature. Considering the 23ºC results, the fatigue crack growth rate exhibits Paris-like behavior until ΔK ≈ 5.5 MPa√m, where the crack growth rate then sharply declines by several orders of magnitude, as has been previously reported.[13,36] This same general behavior is observed as the temperature is decreased, but with two important differences. First, the departure from the Paris-like behavior occurs at increasingly higher ΔK with decreasing temperature, this behavior saturates at where continued reduction of the temperature below 30ºC only exhibit a mild increase in the ΔK at which the growth rate begins to decrease. Second, counter to the 23ºC results, the

sharp decline in crack growth rate from the Paris regime is interrupted by an inflection in the crack growth rate versus ΔK relationship. Interestingly, the crack growth rate within this inflected region for all tested temperatures appears to be Paris-like behavior, albeit at a steeper slope than observed for "upper" Paris law region, with the ΔK range over which this behavior occurs increasing with decreasing temperature.
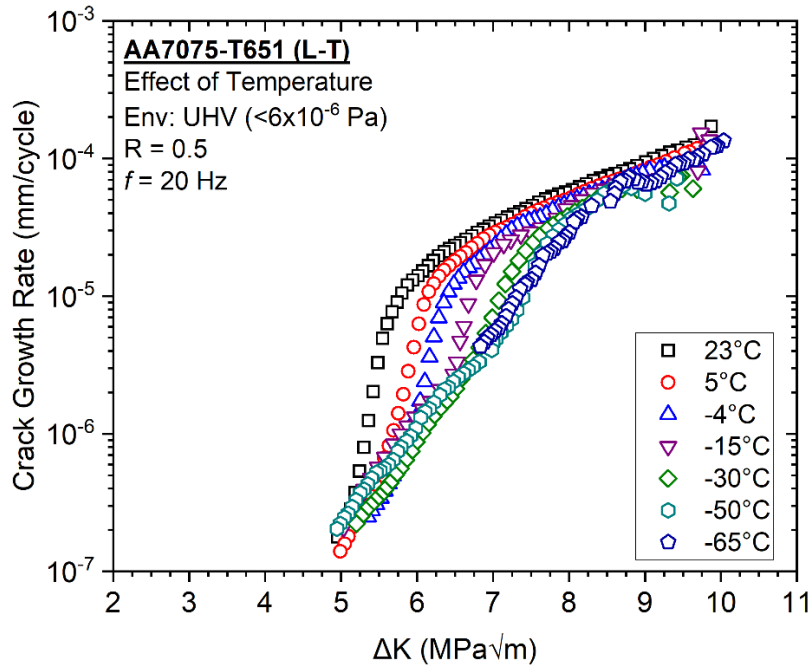
Figure 12 - Measured crack growth rate versus ΔK relationships for AA7075-T651 as a function of temperature in an ultra-high vacuum (UHV) environment at R = 0.5 and f = 20 Hz.

A systematic evaluation of the fracture surfaces at ΔK ranging from 5 to 8 MPa√m suggests an interesting dependence of the observed fracture morphology as a function of both temperature and ΔK. As shown in Figure 13, micrographs taken at locations on the fracture surface corresponding to ΔK ≈ 5 MPa√m show a widespread rough, slip band cracking morphology across all tested temperatures. Similar fracture surface features have been previously reported for AA7075-T6 experiments conducted under ultra-high vacuum at ambient temperature.[9,13,23,36,37] However, as ΔK increases, a temperature-dependent evolution in the fracture morphology is observed. Specifically, as shown in Figure 14 for ΔK ≈ 6 MPa√m (and including the results from

the end of the -65ºC experiment at $\Delta K \approx 6.6$ MPa√m), the fracture morphology at 23ºC (Figure 14a) has transitioned to the flat, river-like transgranular fracture morphology commonly reported in these alloys.[9,13,36–38] Conversely, all other temperatures still exhibit the rough, slip band cracking morphology, though isolated flat, river-like transgranular features can be identified at 5ºC and -4ºC (Figure 14b-c), as indicated by the white arrows. Further increases in ΔK to 7 MPa√m (Figure 15) indicates a complete transition to the flat, river-like transgranular fracture morphology for all temperatures greater than -15ºC (Figures 15a-d), while all lower temperatures still exhibit widespread slip band cracking (Figure 15e-g). Finally, at $\Delta K \approx 8$ MPa√m (Figure 16), the flat, river-like transgranular fracture morphology is present at all tested temperatures, though features consistent with slip band cracking can be still be observed at -50ºC and -65ºC (Figure 16f-g), as indicated by the white arrows.
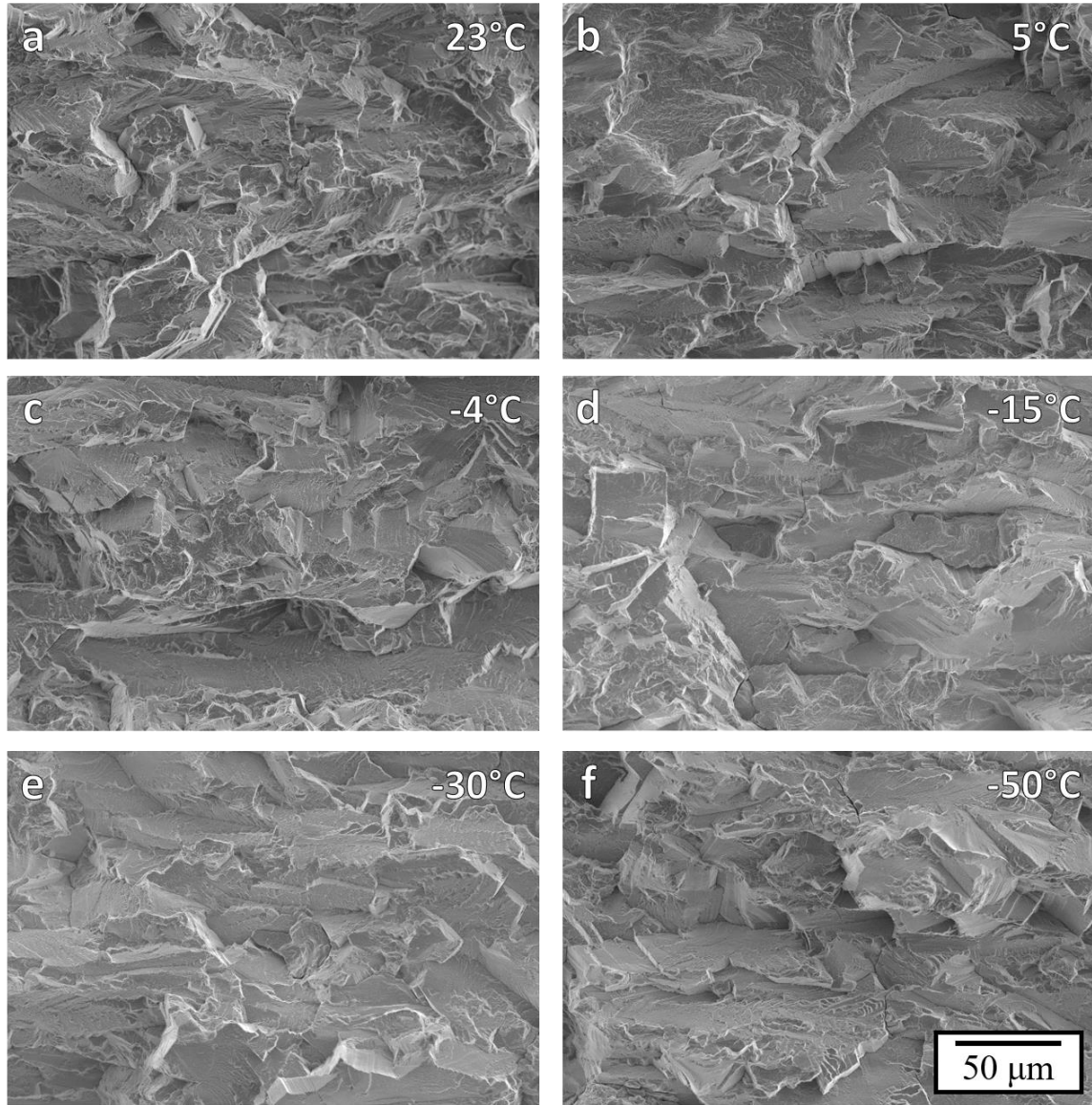
Figure 13 - Micrographs of the observed fracture morphology at ΔK ≈ 5 MPa√m and R = 0.5 for AA7075-T651 cyclic loaded in ultra-high vacuum at temperatures of (a) 23°C, (b) 5°C, (c) -4°C, (d) -15°C, (e) -30°C, and (f) -50°C.
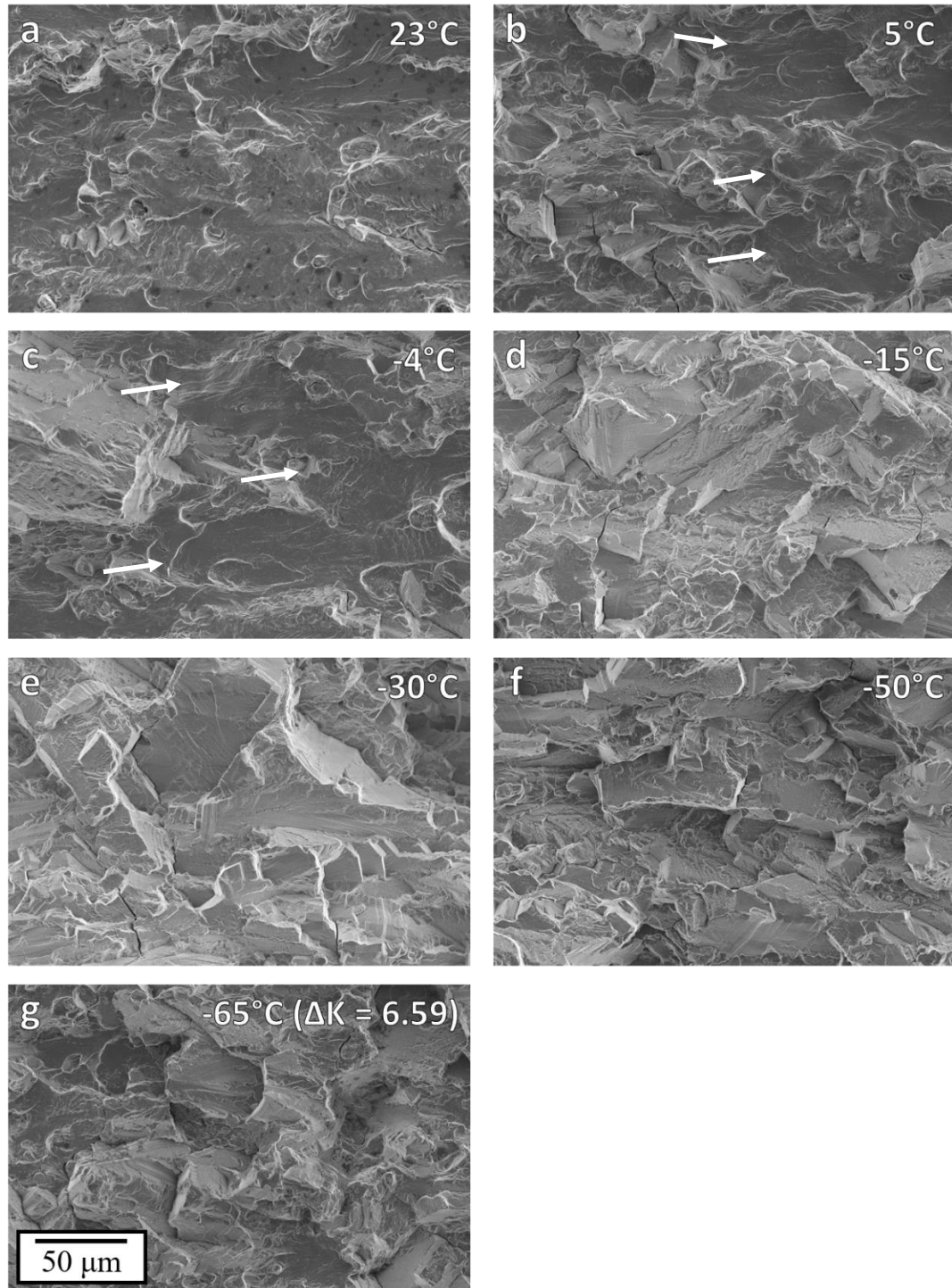
Figure 14 - Micrographs of the observed fracture morphology at $\Delta K \approx 6$ MPa$\sqrt{m}$ and R = 0.5 for AA7075-T651 cyclic loaded in ultra-high vacuum at temperatures of (a) 23°C, (b) 5°C, (c) -4°C, (d) -15°C, (e) -30°C, and (f) -50°C. The observed fracture morphology observed at the end of the experiment conducted at -65°C ($\Delta K \approx 6.6$ MPa$\sqrt{m}$) is shown in (g). White arrows in (b) and (c) indicate isolated flat, river-like features.
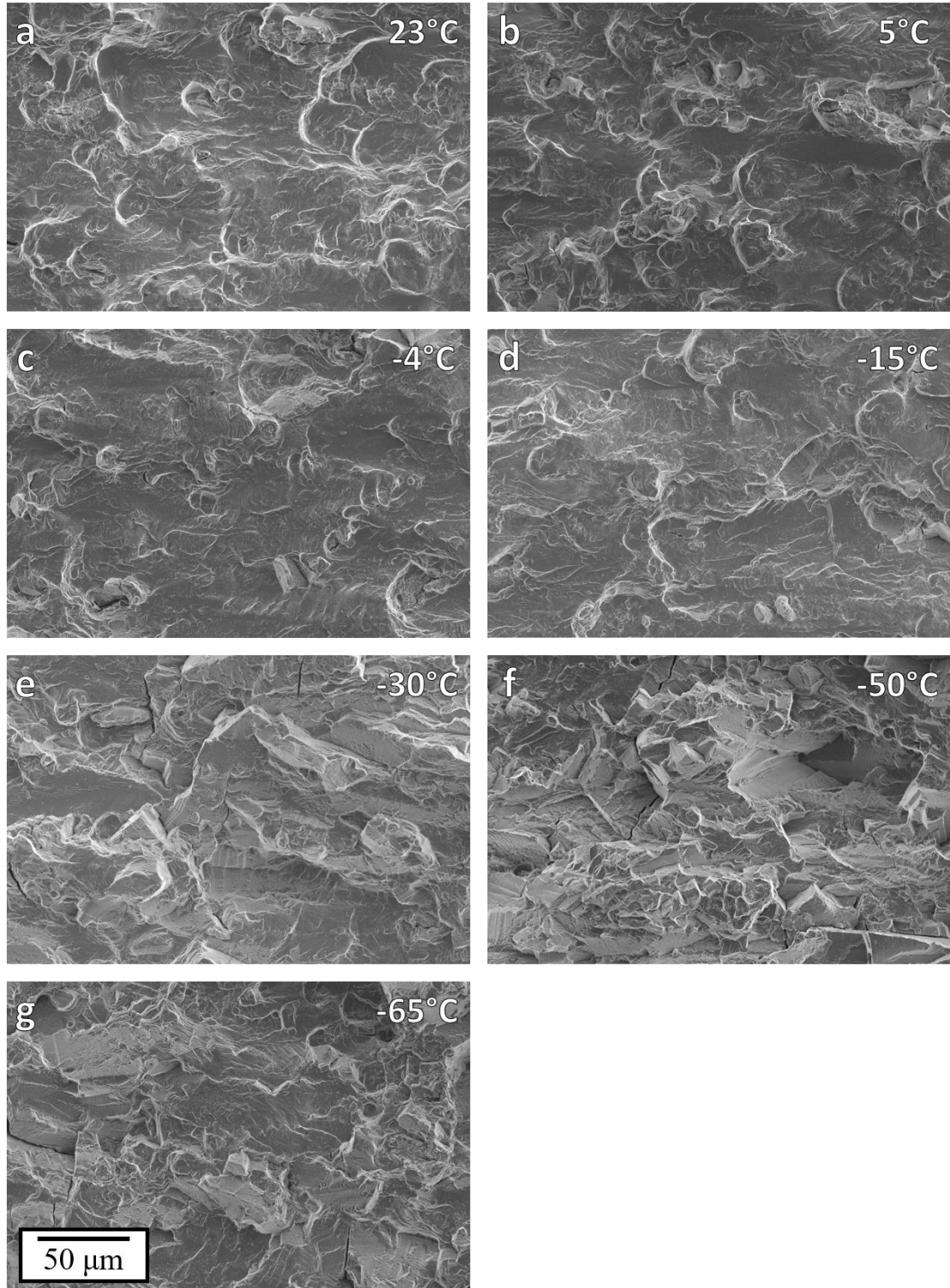
Figure 15 - Micrographs of the observed fracture morphology at $\Delta K \approx 7$ MPa$\sqrt{m}$ and R = 0.5 for AA7075-T651 cyclic loaded in ultra-high vacuum at temperatures of (a) 23°C, (b) 5°C, (c) -4°C, (d) -15°C, (e) -30°C, (f) -50°C, and (g) -65°C.
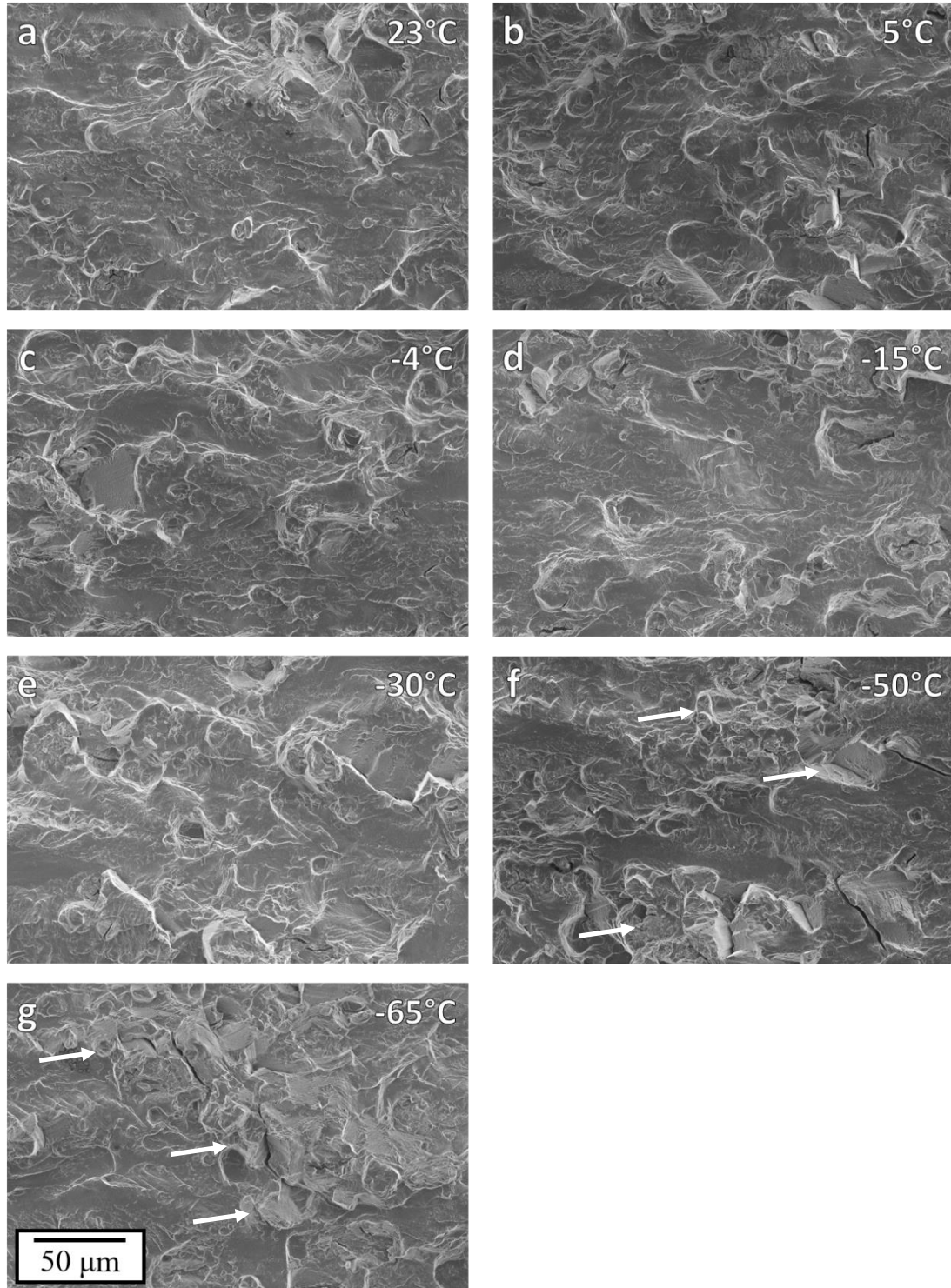
Figure 16 - Micrographs of the observed fracture morphology at ΔK ≈ 8 MPa√m and R = 0.5 for AA7075-T651 cyclic loaded in ultra-high vacuum at temperatures of (a) 23°C, (b) 5°C, (c) -4°C, (d) -15°C, (e) -30°C, (f) -50°C, and (g) -65°C. The white arrows in (f) and (g) indicate features associated with slip band cracking.

Using the fracture surfaces, the crack length (thus ΔK) associated with the transition to the slip band cracking morphology can be identified, thereby facilitating a correlation between the observed crack growth rate versus ΔK relationships and the transition in fracture morphology. The specific ΔK (and associated crack growth rate) corresponding to the onset of the slip band cracking relative to the measured fatigue crack growth relationships are identified in Figure 17 (indicated by the points). As shown in Figure 17, and in agreement with the micrographs shown in Figure 13-16, the ΔK associated with the onset of the slip band cracking increases as the test temperature decreases. Similarly, the crack growth rate associated with the transition to slip band cracking appears to systematically increase with decreasing temperature across the evaluated temperature range. A qualitative examination of these data suggests that the onset of slip band cracking occurs closer to the ΔK associated with the deviation from the upper Paris region as the temperature is decreased; the relevance of this subtle point is unclear.
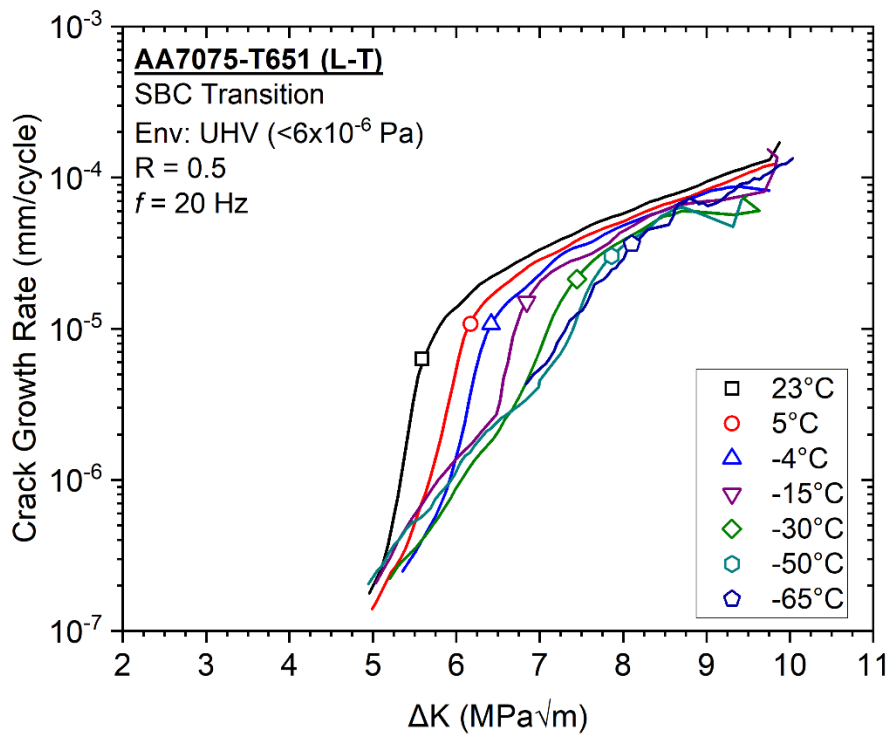
Figure 17 - Identification of the crack growth rate and ΔK associated with the onset of the slip-band cracking fracture morphology (indicated by the symbols) as a function of temperature for AA7075-T651 cyclically loaded in an UHV environment.

The data in Figure 17 suggest that temperature dependence for both the crack growth rate and ΔK is due to the transition from flat, river-like transgranular crack growth to the rough, slip band crack morphology. To better understand these potential dependencies on temperature, the transition ΔK (ΔK_{TR}) is plotted as a function of the inverse absolute temperature (1/T) in Figure 18. As shown in Figure 18, ΔK_{TR} exhibits an initially linear increase with increasing inverse temperature, before exhibiting a clear inflection (demonstrated by the black dashed lines) at an inverse temperature corresponding to -30°C. Beyond this inflection point, a distinctly shallower increase in ΔK_{TR} is observed as a function of inverse temperature. Note that Figure 18 is plotted on a linear-linear scale for clarity, but this same general trend was also observed when ΔK_{TR} is plotted on a log-scale, indicating that transition behavior may be related to thermally activated processes.
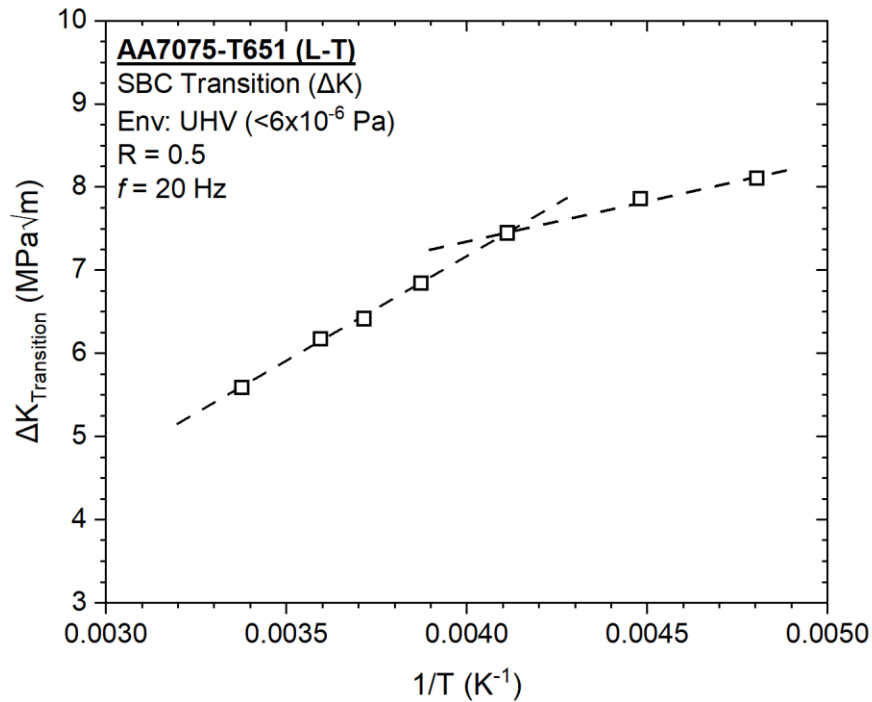
Figure 18 - Observed dependence of the (a) ΔK associated with the transition in fracture morphology on the inverse absolute temperature. The black lines are added to highlight the inflection in the ΔK versus 1/T relationship.

3.4. Discussion

The presented fatigue crack growth data (Figure 12) demonstrate that the fatigue behavior of AA7075-T651 in ultra-high vacuum environments is strongly affected by decreasing temperature. Systematic fractography conducted at ΔK ranging from 5 to 8 MPa√m (Figures 13-16) indicated that the transition in fracture morphology from flat, river-like crack growth to jagged, crystalline slip band cracking was also sensitive to temperature. The specific crack growth rate and ΔK associated with this transition were then identified for each temperature (Figure 17). Critically, both the crack growth rate and ΔK associated with this fracture morphology transition increase with decreasing temperature, but with different dependencies. Specifically, when evaluated as a function of inverse absolute temperature (Figure 18), ΔK_{TR} exhibits two apparent regimes of temperature dependent behavior. In the following discussion, these results are first considered in the context of current literature understanding of low temperature fatigue behavior in aluminum alloys. Based on this background, a mechanism to describe the observed temperature dependence of the transition in fracture morphology for AA7075-T651 cyclically loaded in an UHV environment is then proposed.

3.4.1. Comparison to literature

Low temperatures are broadly considered to decrease the susceptibility of fatigue damage in materials with the reasoning sometimes being inconclusive or mechanistic,[1,3–6,39–43] but when provided it is generally attributed to extrinsic factors such as the reduction or elimination of deleterious environmental elements such as water or oxygen,[8–13,19,20,44] crack closure from the cracking mechanism creating a rougher fractured surface,[25–27] or both.[14,15,45] Since both factors have a proven potential impact on fatigue behavior, specifically for AA7075-T651, it is critically important to remove these non-desired factors to properly evaluate the effects of low temperatures on the fatigue behavior. Specifically, when testing at low temperatures associated with high altitude environments, existing water vapor in the testing environment will form an ice layer on the cooled surface of the specimen where the partial pressure of water vapor above this ice is high enough to potentially impact the fatigue behavior of AA7075-T651 as shown by previous studies done by Burns et al.[13,19] Particularly, the low partial pressure values of water vapor associated with lower temperatures were shown to adversely affect fatigue behavior independent of any

contribution from the lower temperatures.[23] The specific issues from non-temperature environmental effects and closure can be identified in the comparison studies displayed in Figure 19.
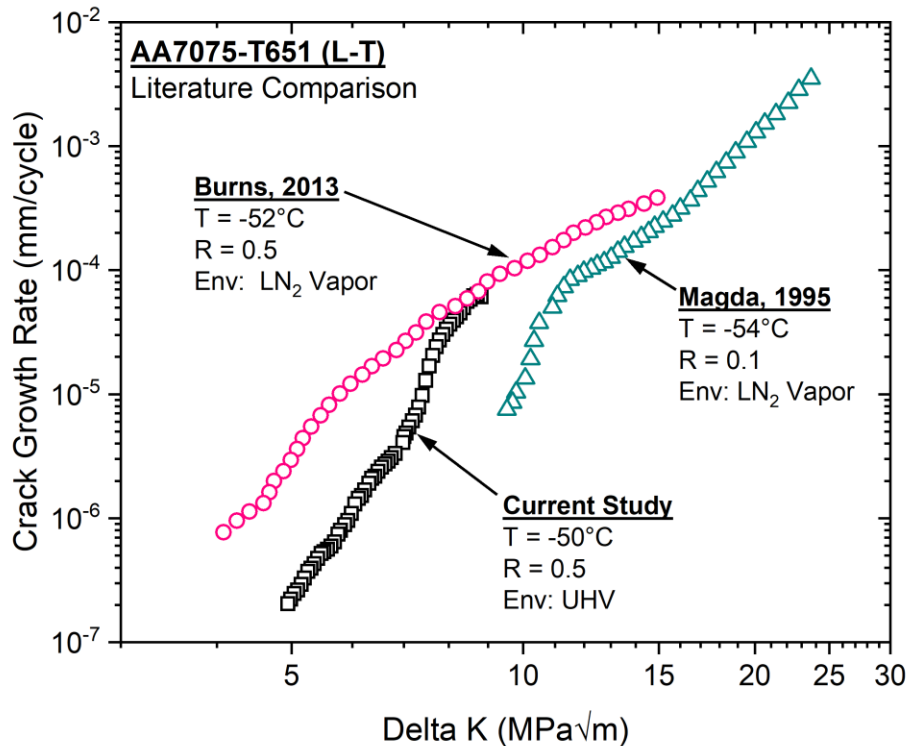
Figure 19 - Comparison of the measured crack growth rate versus ΔK relationship for AA7075-T651 from the current study at -50°C in an UHV environment to literature results on AA7075-T6 at similar temperatures. All data are for the L-T orientation.

Despite these studies being at similar temperatures with one of the experiments completed for the current study the observed fatigue behaviors are very different. The Burns et al. study, presents similar fatigue behavior observed in the comparison from the current study, but diverges with higher fatigue crack growth rates at driving forces of $\Delta K \approx 7$ MPa√m and lower, which is likely attributed to the water vapor/hydrogen embrittlement effects becoming dominate over the temperature-dependent intrinsic behavior of the material.[19] The Magda et al. study exhibits a significant deviation to slower fatigue crack growth rates from the other studies at a driving force of $\Delta K \approx 12$ MPa√m and below, which is likely a consequence of the low stress ratio (R = 0.1)

allowing for the closure effects to alter the behavior of the fatigue crack.[4] These same issues of water vapor and closure can be observed obfuscating the results of other similar studies completed with similar peak aged-alloys[13,20] as well as similar overaged-alloys.[1,10,36,46] Specifically, the results from Ostash et al. is further complicated by the load history of the specimen since the material used for the experiment was taken from the lower skins of an AN-12 aircraft after 40 years of operation.[20] The current study avoids such issues by eliminating non-temperature environmental factors by utilizing an UHV environment before the specimen is cooled and maintained during the duration of the experiments as well as employing a high stress ratio (R = 0.5), which eliminated closure issues as evidenced in Figure 20. Explanations for the change in low temperature fatigue behavior are not limited to just other environmental factors and closure as a transition to intergranular cracking in AA7475-T761[18] and delamination toughening in 8090-T6[47] have been postulated, but no evidence of either mechanism was found in the current study. Lastly, other studies have proposed that modifications to temperature sensitive dislocation processes and interactions such as cross-slip, dislocation cell formation, and emission of dislocations from sources near the crack tip are responsible for the observed differences in fatigue behavior at low temperatures.[26,48–52] The examination of the temperature dependence of the ΔK_{TR} for this study also implicates a temperature sensitive dislocation processes being affected as the slip band cracking appears to be associated with very low energy processes.
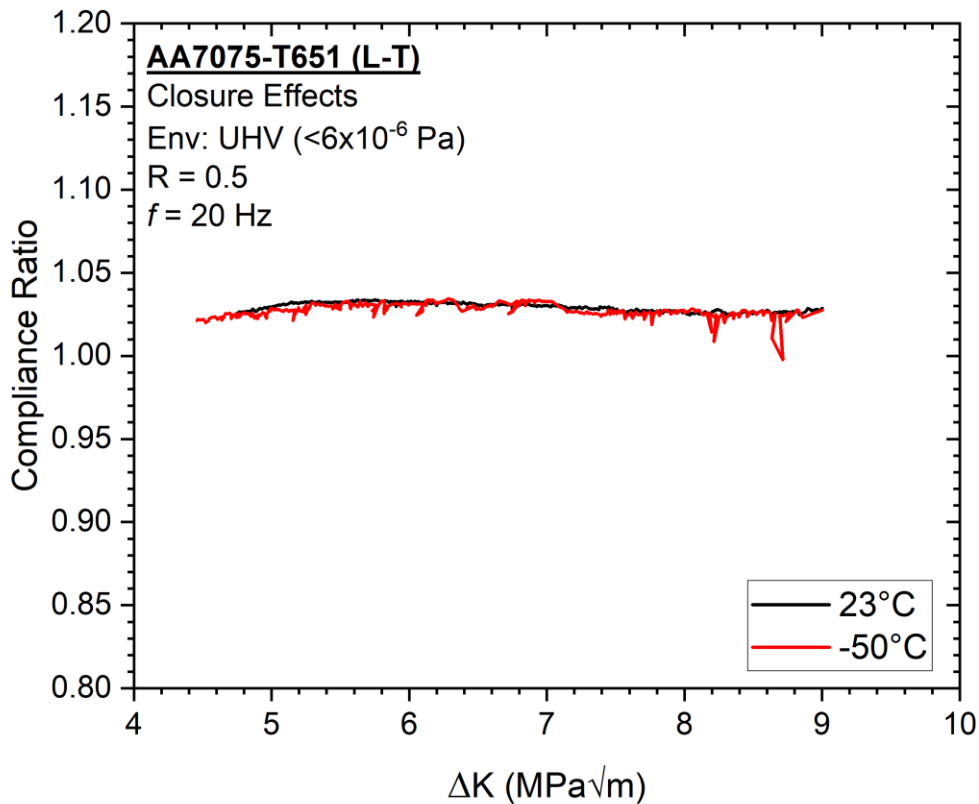
Figure 20 - Observed variation in compliance ratio with ΔK for testing conducted at 23 and -50°C demonstrating the general absence of closure for both experiments.

3.4.2. Proposed low temperature fatigue cracking mechanisms

The results of the current study suggest the intrinsic fatigue behavior of AA7075-T651 is impacted by temperature making the material more resistant to fatigue damage as the temperature is lowered. The intrinsic behavior for all observed temperatures of this material was observed to have a flat-transgranular cracking mechanism at the relatively high driving forces with a transition to a rough crystallographic cracking mechanism below some temperature-dependent threshold driving force, where the onset of the rough crystallographic cracking results in a significant decrease in the measured crack growth rate. During fatigue, materials accommodate cyclic damage via emission of dislocations or a cleavage-like fracture. In the flat-transgranular cracking regime, dislocation emission is dominant at the crack tip, moving newly emitted dislocations a driving force dependent distance away from the crack tip on a given slip system toward a barrier of

movement such as a precipitate. Emission of dislocations rather than a cleavage-type rupture of the slip plane is predicted by Peierls analyses done previously, which yield a principle result that the activation energy for dislocation emission is substantially lower.[53] Subsequent cycling and emission of additional dislocations push the previously emitted dislocations closer to the barrier, where at the higher driving forces the dislocations have sufficient energy to move passed the barrier via by-pass or shear allowing for further damage accumulation.[53] At some point the number of dislocations will become high enough and be far enough away from the crack tip where the driving force for dislocation movement is sufficiently low to create a dislocation pile-up at a barrier leading to instability between the barrier and dislocations, which results in a release of back stress allowing the crack tip to step forward via a fracture process to a new quasi-equilibrium position.[54] The 23°C experimental results suggest the existence of an intrinsic threshold driving force must be overcome for the observed flat-transgranular fracture mechanism to become the dominant.

The current experimental results at low temperatures indicate the value of this threshold driving force for flat-transgranular fracture increases as the temperature is lowered, which is believed to be a result of 1) A decrease in ability for dislocations to move and subsequently overcome barriers such as precipitates and/or 2) A decrease in thermal energy needed to overcome the activation energy for dislocation emission from the crack tip resulting in cleavage type rupture to become more favorable. First, the ability to move dislocations away from the crack tip and past barriers such as precipitates is thermally dependent, thus as the temperature decreases the activation energy required for dislocation movement increases.[45] The resulting restriction in dislocation movement would keep emitted dislocations closer to the crack tip, which a Peierls-type model predicts that dislocations within 10-100 nm of the crack tip may suppress continued emission of dislocations thus favoring a transition to a cleavage type rupture.[53] Second, the Peierls analyses done previously predicts a decrease in temperature will increase significantly the critical crack tip load needed for emission consequently lowering the barrier for a cleavage type rupture to occur.[53,55] The combination of decreasing ability to move dislocations away from the crack tip and past precipitates as well as the increase in activation energy for dislocation emission from the crack tip corresponds with the observed increase in the threshold driving force for the transition from crystallographic cracking to the flat transgranular cracking with decreasing temperature. Future work leveraging a multiscale characterization approach similar to the one outlined by the

Harris et al. study would be beneficial in gaining further insights into the mechanisms involved in the fatigue process and how they are affected by these low temperatures.[56]

3.5. Conclusions

The influence of low temperatures associated with high-altitude environments on the fatigue behavior of AA7075-T651 was assessed. Particularly, crack growth rates across a range of driving forces at various temperatures varying from 23°C to -65°C, SEM analysis of the fractured surface, and examination of the temperature depend behavior was evaluated. Additionally, the results from the current study were compared to relevant literature to develop a mechanistic understanding of the observed behavior. Based on the results of the current study the following conclusions can be made:

1. Low temperature environments have a clear effect on the fatigue behavior of AA7075-T651, where decreasing temperature decelerates the crack growth rates seen in the near-threshold regime.

2. Observations of the fatigue fracture surfaces demonstrated a widespread rough, slip band cracking morphology in the near threshold regime, but the appearance of a temperature-dependent evolution in the fracture morphology to a flat, river-like transgranular fracture morphology occurred at all tested temperatures.

3. The ΔK corresponding to the transition to a slip band cracking morphology was identified, which facilitated a correlation between the observed crack growth rate versus ΔK and the transition in fracture morphology. The correlation demonstrated the ΔK associated with the onset of the slip band cracking increasing as the temperature decreased and the crack growth rate associated with the transition to increase with decreasing temperature across the evaluated temperature range.

4. The ΔK_{TR} was plotted as a function of the inverse absolute temperature, exhibiting an initial linear increase with increasing inverse temperature with a clear inflection at an inverse temperature corresponding to -30ºC. Beyond the inflection point, a distinctly shallower increase in ΔK_{TR} was observed indicating the effects on fatigue behavior are most dominate at low ΔK levels and become decreasingly significant as driving forces increase, reaching a saturation point with high driving force levels.

5. The observed changes in low temperature fatigue of AA7075-T651 are not impacted by common extrinsic factors such as water vapor content or closure, indicating temperature impacts some temperature sensitive dislocation process responsible for fatigue damage.

3.6. Suggestions for future study

The data presented in this chapter indicated a possible full saturation of the temperature effects on fatigue cracking of AA7075-T651 at a temperature around -50°C. Data for the one temperature below -50°C was nearly identical, but it is not clear if this is an indication of the saturation of temperature effects or just smaller incremental changes to the temperature effects at temperatures below -50°C, thus future work examining temperatures far below -65°C would answer this question. Examination of fatigue at temperatures below -65°C can inform cryogenic applications, which also may also be prone to fatigue damage. Additionally, further characterization is still needed to either confirm the mechanisms proposed in this study or to inform another for the cause of shift to a higher driving force for the transition between transgranular cracking and SBC as the temperature decreases.

3.7. Acknowledgements

3.8. References

1. Abelkis, P. R., Harmon, M. B., Hayman, E. L., Mackay, T. L. & Orlando, J. Low Temperature and Loading Frequency Effects on Crack Growth and Fracture Toughness of 2024 and 7475 Aluminum. *ASTM Spec. Tech. Publ.* 257–273 (1985). doi:10.1520/stp32760s

2. Burns, J. T., Gupta, V. K., Agnew, S. R. & Gangloff, R. P. Effect of low temperature on fatigue crack formation and microstructure-scale propagation in legacy and modern Al-Zn-Mg-Cu alloys. *Int. J. Fatigue* **55**, 268–275 (2013).

3. Carpinteri, A. & Brighenti, R. Fracture and fatigue properties of metallic alloys S275 J2 and Al7075 T6 at low temperatures. *J. Mater. Sci.* **43**, 4780–4788 (2008).

4. Magda, D. J. Effect of Low Temperatures and Anisotropy on Fatigue Crack Behavior of Aluminum Alloys. (University of Utah, 1995).

5. Oskouei, R. H. & Ibrahim, R. N. The effect of typical flight temperatures on the fatigue behaviour of Al 7075-T6 clamped plates. *Mater. Sci. Eng. A* **528**, 1527–1533 (2011).

6. Shlyannikov, V. N., Yarullin, R. R. & Ishtyryakov, I. S. Effect of temperature on the growth of fatigue surface cracks in aluminum alloys. *Theor. Appl. Fract. Mech.* **96**, 758–767 (2018).

7. Burns, J. T. & Gangloff, R. P. Effect of Low Temperature on Fatigue Crack Formation and Microstructure-Scale Growth from Corrosion Damage in Al-Zn-Mg-Cu. *Metall. Mater. Trans. A* **44**, 2083–2105 (2013).

8. Brown, L. B., Jones, J. L., Warner, J. S. & Burns, J. T. Effect of low temperature , low water vapor pressure environments on the fatigue behavior of an Al-Li aerospace alloy. *Int. J. Fatigue* **148**, 106215 (2021).

9. Gasquères, C., Sarrazin-Baudoux, C., Petit, J. & Dumont, D. Fatigue crack propagation in an aluminium alloy at 223 K. *Scr. Mater.* **53**, 1333–1337 (2005).

10. Cox, J. M., Pettit, D. E. & Langenbeck, S. L. Effect of Temperature on the Fatigue and Fracture Properties of 7475-T761 Aluminum. *ASTM Spec. Tech. Publ.* 241–256 (1985). doi:10.1520/stp32759s

11. Tchitembo Goma, F. A. *et al.* Effect of extrusion aspect ratio and test temperatures on fatigue crack growth behavior of a 2099-T83 Al-Li alloy. *Int. J. Fatigue* **59**, 244–253 (2014).

12. Liu, M. D. & Xiong, J. J. Fatigue crack growth testing and evaluation for aluminum alloys at temperatures of 25°C and −70°C. *J. Test. Eval.* **46**, 1698–1707 (2017).

13. Burns, J. T., Jones, J. J., Thompson, A. W. & Locke, J. S. (Warner). Fatigue crack propagation of aerospace aluminum alloy 7075-T651 in high altitude environments. *Int. J. Fatigue* **106**, 196–207 (2018).

14. Grinberg, N. M. *et al.* Fatigue life and crack resistance of sheet Al-Li 1460 alloy at 293 to 4 K. *Int. J. Fatigue* **15**, 393–400 (1993).

15. Petit, J., Sarrazin-Baudoux, C. & Gerland, M. Influence of microstructure, environment and temperature on fatigue crack propagation in 2XXX aluminium alloys. *Key Eng. Mater.* **592–593**, 22–29 (2014).

16. Moreto, J. *et al.* Environmentally-assisted Fatigue Crack Growth in AA7050-T73511 Al Alloy and AA2050-T84 Al-Cu-Li Alloy. *Mater. Res.* **18**, (2015).

17. Liu, M. D., Xiong, J. J., Liu, J. Z. & Tian, B. J. Modified model for evaluating fatigue behaviors and lifetimes of notched aluminum-alloys at temperatures of 25 °C and −70 °C. *Int. J. Fatigue* **93**, 122–132 (2016).

18. Pettit, D. E. & van Orden, J. M. Evaluation of Temperature Effects on Crack Growth in Aluminum Sheet Material. *ASTM Spec. Tech. Publ.* 106–124 (1979). doi:10.1520/stp34909s

19. Burns, J. T., Gupta, V. K., Agnew, S. R. & Gangloff, R. P. Effect of low temperature on fatigue crack formation and microstructure-scale propagation in legacy and modern Al–Zn–Mg–Cu alloys. *Int. J. Fatigue* **55**, 268–275 (2013).

20. Ostash, O. P., Andreiko, I. M., Holovatyuk, Y. V., Semenets', O. I. & Koval'chuk, L. B. Low-Temperature and Corrosion Fatigue Crack-Growth Resistance of D16ATNV and V95T1 Aluminum Alloys after Long-Term Operation. *Mater. Sci.* **50**, 350–357 (2014).

21. Yarullin, R. & Ishtyryakov, I. Fatigue Surface Crack Growth in Aluminum Alloys under Different Temperatures. *Procedia Eng.* **160**, 199–206 (2016).

22. Wexler, A. Vapor Pressure Formulation for Ice. *J Res Natl Bur Stand Sect A Phys Chem* **81 A**, 5–20 (1977).

23. Burns, J. T. *et al.* Effect of water vapor pressure on fatigue crack growth in Al – Zn – Cu – Mg over wide-range stress intensity factor loading. *Eng. Fract. Mech.* **137**, 34–55 (2015).

24. Burns, J. T., Jones, J. J., Thompson, A. W. & Warner-Locke, J. S. Fatigue crack propagation of aerospace aluminum alloy 7075-T651 in high altitude environments. *Int. J. Fatigue* **106**, 196–207 (2018).

25. Esaklul, K. A., Yu, W. & Gerberich, W. W. Effect of Low Temperature on Apparent Fatigue Threshold Stress Intensity Factors. *ASTM Spec. Tech. Publ.* 63–83 (1985). doi:10.1520/stp32747s

26. Liaw, P. K., Logsdon, W. A. & Attaar, M. H. Computerized Near-Threshold Fatigue Crack Growth Rate Testing At Cryogenic Temperatures: Technique and Results. *ASTM Spec. Tech. Publ.* 173–190 (1985). doi:10.1520/stp32754s

27. Park, K. J. & Lee, C. S. Fatigue Crack Propagation in Al-Li 8090 Alloy at Room (300K) and Cryogenic (77K) Temperatures. *Scr. Mater.* **34**, 215–220 (1996).

28. Papazian, J. *et al.* DARPA/NCG structural integrity prognosis system. *DARPA* **HR0011-04**, (2009).

29. B209-14 Standard Specification for Aluminum and Aluminum-Alloy Sheet and Plate. *ASTM Int.* (2014). doi:https://doi.org/10.1520/B0209-14

30. Burns, J. T., Larsen, J. M. & Gangloff, R. P. Driving forces for localized corrosion-to-fatigue crack transition in Al-Zn-Mg-Cu. *Fatigue Fract. Eng. Mater. Struct.* **34**, 745–773 (2011).

31. Payne, J., Welsh, G., Christ Jr, R. J., Nardiello, J. & Papazian, J. M. Observations of fatigue crack initiation in 7075-T651. *Int. J. Fatigue* **32**, 247–255 (2010).

32. E647-15e1. Standard Test Method for Measurement of Fatigue Crack Growth Rates. *ASTM B. Stand.* 1–49 (2016). doi:10.1520/E0647-15E01.2

33. Donald, J. K. Introducing the compliance ratio concept for determining effective stress intensity. *Int. J. Fatigue* **19**, 191–195 (1997).

34. Donald, J. K., Bray, G. H. & Ralph, W. an Evaluation of the Adjusted Compliance Ratio Technique. 674–695 (1999).

35. E647-15e1 Standard Test Method for Measurement of Fatigue Crack Growth Rates. *ASTM Int.* 1–49 (2015). doi:10.1520/E0647-15E01.2

36. Lafarie-Frenot, M. C. & Gasc, C. The Influence of Age-Hardening of Fatigue Crack Propagation Behaviour in 7075 Aluminum Alloy in Vacuum. *Fatigue Eng. Mater. Struct.* **6**, 329–344 (1983).

37. Grinberg, N. M. The effect of vacuum on fatigue crack growth. *Int. J. Fatigue* **4**, 83–96 (1982).

38. Burns, J. T. *et al.* Effect of water vapor pressure on fatigue crack growth in Al-Zn-Cu-Mg over wide-range stress intensity factor loading. *Eng. Fract. Mech.* **137**, 34–55 (2014).

39. Ostash, O. P. & Zhmur-Klimenko, V. T. Fatigue crack growth in metals at low temperatures. *Sov. Mater. Sci.* **23**, 124–135 (1987).

40. Polak, J. & Klesnil, M. The Dynamics of Cyclic Plastic Deformation and Fatigue Life of Low Carbon Steel at Low Temperature. *Mater. Sci. Eng.* **26**, 157–166 (1976).

41. Verkin, B. I., Grinberg, N. M., Serdyuk, V. A. & Yakovenko, L. F. Low temperature fatigue fracture of metals and alloys. *Mater. Sci. Eng.* **58**, 145–168 (1983).

42. Laird, C. The Influence of Metallurgical Structure on the Mechanisms of Fatigue Crack Propagation. *ASTM STP 415* (1967).

43. Campbell, J. Fracture Toughness of High-Strength Alloys at Low Temperature—A Review. *Am. Soc. Test. Mater.* 3–25 (1974). doi:10.1520/stp33119s

44. Burns, J. T. & Gangloff, R. P. Effect of low temperature on fatigue crack formation and microstructure-scale growth from corrosion damage in Al-Zn-Mg-Cu. *Metall. Mater. Trans. A Phys. Metall. Mater. Sci.* **44**, 2083–2105 (2013).

45. Liaw, P. K. & Logsdon, W. A. Fatigue Crack Growth Threshold at Cryogenic Temperatures: A Review. *Eng. Fract. Mech.* **22**, 585–594 (1985).

46. Anderson, K., Weritz, J. & Kaufman, J. G. 7175 and 7475 High-Purity Versions of 7075. *Prop. Sel. Alum. Alloy.* **2**, 448–452 (2019).

47. Xu, Y. B., Wang, L., Zhang, Y., Wang, Z. G. & Hu, Q. Z. Fatigue and Fracture behavior of an Aluminum-lithium alloy 8090-T6 at ambient and cryogenic temperature. *Metall. Trans.* **22A**, 723–729 (1991).

48. Liaw, P. K. & Fine, M. E. Fatigue Crack Propagation in 99.99+ and 1100 Aluminum at 298 and 77 K. *Metall. Trans. A* **12A**, 1927–1937 (1981).

49. Liaw, P. K., Fine, M. E., Kiritani, M. & Ono, S. The Effect of Temperature on the Fatigue Crack Propagation Rate in Aluminum. *Scr. Metall.* **11**, 1151–1155 (1977).

50. McCammon, R. D. & Rosenberg, H. M. The fatigue and ultimate tensile strengths of metals between 4.2 and 293° K. *R. Soc.* **242**, (1957).

51. McKittrick, J., Liaw, P. K., Kwun, S. I. & Fine, M. E. Threshold for Fatigue Macrocrack Propagation in Some Aluminum Alloys. *Metall. Trans. A, Phys. Metall. Mater. Sci.* **12 A**, 1535–1539 (1981).

52. Yu, W., Esaklul, K. & Gerberich, W. W. Fatigue Threshold Studies in Fe, Fe-Si, and HSLA Steel: Part II. Thermally Activated Behavior of the Effective Stress Intensity at Threshold. *Metall. Trans.* **15A**, 889–900 (1984).

53. Shastry, V. & Anderson, P. M. Interaction between emission and cleavage at crack tips. *Philos. Mag. A* **75**, 771–789 (1997).

54. Gerberich, W. W., Davidson, D. L., Chen, X. F. & Lee, C. S. Dislocation dynamics of crack-tip processes-frequency observations and theoretical modeling. *Eng. Fract. Mech.* **28**, 505–518 (1987).

55. Rice, J. R. & Beltz, G. E. The activation energy for dislocation nucleation at a crack. *J. Mech. Phys. Solids* **42**, 333–360 (1994).

56. Harris, Z. D., Thompson, A. W. & Burns, J. T. Multiscale Assessment of Deformation Induced by Hydrogen Environment-Assisted Cracking in a Peak-Aged Ni-Cu Superalloy. *JOM* **72**, 1993–2002 (2020).

Chapter 4 – The development of a Pt deposition protocol for use with the FIB lift-out technique

The following chapter is a scaled down version of the publication made from the discussed study. The publication for this chapter can be found in Appendix A.

4.1. Overview

4.1.1. Introduction to the FIB Pt protection layer deposition

Focused ion beam (FIB) milling with Ga+ ions is a common technique for the preparation of transmission electron microscopy (TEM) specimens due to several distinct advantages over traditional TEM sample preparation strategies.[1–3] In particular, FIB milling enables one to obtain TEM samples: (1) from specific regions of interest with high spatial precision, (2) in a relatively time-efficient manner, and (3) with modestly-sized regions of electron transparency. However, a critical shortcoming of the FIB milling approach is the possibility of specimen damage from the impinging Ga+ ions.[4,5] This damage can occur in several forms, depending on specimen composition/microstructure, ion beam current and accelerating voltage, and the impingement geometry. For example, studies have shown that FIB milling with Ga+ ions can cause: (1) the formation of an amorphous surface layer (which can reach a thickness of >100 nm),[6] (2) the injection of dislocations and vacancies through knock-on processes,[7] (3) the formation of Ga intermetallic phases in certain metallic materials,[8,9] (4) the implantation of Ga into the specimen bulk (with local compositions being reported as high as 20 at. %),[10] (5) preferential grain growth/texture evolution in metallic materials,[11] and (6) phase transformations such as the $\gamma \rightarrow \alpha$ transformation in steels.[12,13]

As this damage can obfuscate the interpretation of any subsequent TEM characterization, numerous methodologies have been suggested for mitigating FIB-induced artifacts. Of these different approaches, the most common mitigation strategy is the deposition of a protective Pt "strap" over the region of interest prior to FIB milling.[3] Briefly, the Pt strap is deposited as follows: (1) a precursor gas (e.g. $C_9H_{16}Pt$) is introduced into the chamber via a fine nozzle located near the specimen surface, causing (2) the precursor gas to adsorb onto the specimen surface, where (3) the incident beam (either electron or ion) causes a decomposition of the precursor gas into volatile and nonvolatile components, which results in (4) the volatile components (hydrogen and carbon)

leaving the surface and (5) the deposition of the nonvolatile Pt.[3] This Pt strap provides two advantages: (1) it protects the underlying material from a direct interaction with the ion beam (I-beam) during FIB milling and (2) it ensures a smooth surface, which has been shown to minimize "curtaining" from surface irregularities.[3] However, a critical limitation of this protection scheme is that the ions impinging on the specimen surface during the initial stages of the Pt deposition process (i.e. until a critical thickness is achieved) can cause damage that is predominantly localized to the near-surface region.[14–16]

Understanding the implications of this surface-localized damage layer is particularly pertinent given the increased interest in leveraging FIB milling to prepare TEM specimens from the fracture surfaces of metallic components. For example, several recent studies have utilized FIB milling to examine the near-fracture surface deformation structure generated during both cyclic and monotonic loading in Ni and Fe-based alloys.[17,18] Such experiments are especially of interest to the environmental cracking community, where the localized environment-material interactions occurring proximate to the crack tip are expected to govern alloy susceptibility.[19] Critically, as FIB milling enables the opportunity to directly examine the microstructure in the near-crack tip region, it is now possible to correlate changes in environment, loading protocol, and metallurgy with local deformation behavior and the concomitant effect on crack growth kinetics. Such insights could then be used to mechanistically inform models for environmental cracking, validate theories for crack tip mechanical fields, and understand the role of individual microstructural features on the fracture process. However, decoupling the deformation/microstructure evolution induced from damage during FIB milling from that generated during loading is non-trivial. Numerous studies on mitigating FIB-induced damage have been published, with particular focus on understanding damage character in Si and pure metals.[4,9,10,20–22] However, extension of these results into more complex engineering-relevant alloys is complicated by the possible influences of prior cold working, precipitation hardening, and other alloy modifications. Additionally, a small number of studies suggest that depositing an initial layer of Pt using the electron beam (E-beam) can effectively mitigate damage induced during I-beam deposition.[16,23] Other authors have suggested using materials such as sputter-deposited Au and Cr or polymeric sheets for a similar "initial barrier" purpose.[4,14,24] However, despite being widely available, the use of E-beam Pt prior to depositing I-beam Pt is generally not utilized in the literature, particularly on structural alloys which have complex microstructures. These knowledge gaps motivate a study to better understand

the extent of damage as a function of applied Pt deposition parameters, as well as the efficacy of the E-beam/I-beam strategy to prevent such damage in structural alloys.

The objective of this work is to evaluate the near-surface damage induced by commonly employed Pt deposition strategies in the aerospace alloy AA7075-T651. Transmission electron microscopy is employed to quantify the depth of FIB-induced damage as a function of applied Pt deposition parameters, which are compared to the results of Monte Carlo simulations of ion bombardment. The impact of these results is then discussed in the context of preparing TEM specimens from surface-sensitive specimens, such as fracture surfaces.

4.2. Material and Methods

All experiments were conducted on AA7075-T651, procured in the form of a 50.8-mm thick plate. This alloy was selected due to the high likelihood of susceptibility to FIB-induced damage (based on a previous study on FIB damage in Al alloys)[25] as well as its technological relevance as a widely-utilized aerospace alloy. Microstructure details for this plate of material are reported elsewhere.[26,27] For this study, two small sections (termed Block 1 and Block 2) were taken from the plate such that the thickness of each section was centered at a depth of 8.5 mm from the surface. Block 1 had dimensions (L x W x H) of 12.15 mm x 7.60 mm x 7.06 mm, while Block 2 was 8.88 mm x 5.80 mm x 7.59 mm. Five different Pt deposition protocols, termed Samples 1-5 and shown in Figure 21, were evaluated in this work. Samples 1-4 were separately excised from a surface of Block 1 that was cut using a low-speed wafering saw; this saw-cut surface was used to simulate the damage and uneven surface topography of a fracture surface. The primary objective for Samples 1-4 was to determine the extent of damage that occurs during different Pt deposition strategies, to inform which Pt deposition protocol best prevented damage for subsequent use on Sample 5. Sample 5 was excised from Block 2, which was cold-rolled to ~50% of the original thickness and then polished to a surface finish of 0.1 μm using diamond slurries. Polishing prior to the Pt deposition was completed to remove the recrystallized surface layer induced by adiabatic heating from the rolling process. Critically, the removal of this recrystallized layer formed during rolling enabled any observed recrystallization in the FIB-prepared TEM specimen to be solely attributed to FIB damage. Moreover, as this cold-worked specimen is expected to contain a significantly increased dislocation density relative to Samples 1-4, the driving force for recrystallization from either FIB-induced temperature increases or imparted strain from impinging

Ga$^+$ ions is expected be elevated, thereby making Sample 5 more susceptible to FIB damage relative to Samples 1-4.
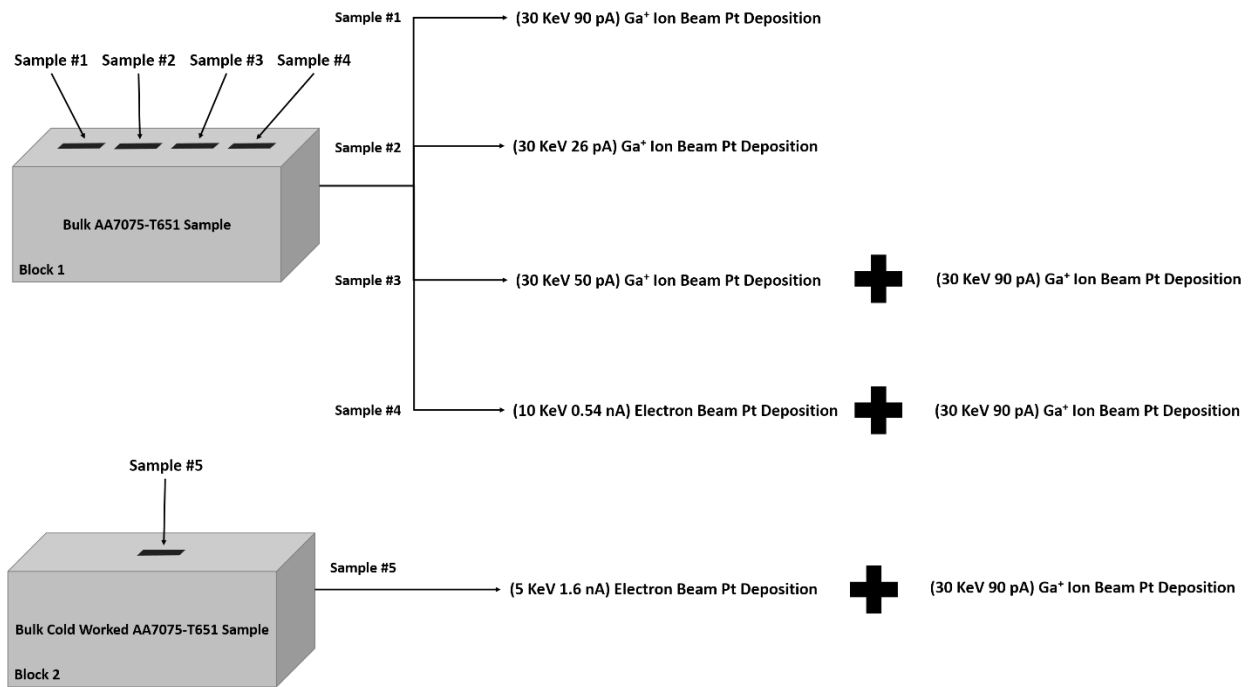
Figure 21 - Overview of applied Pt deposition protocols for each TEM sample.

Damage induced from each Pt deposition protocol was examined *via* TEM using a FEI Titan operated at 300 keV. TEM specimens were prepared using the following lift-out procedure. First, Pt was deposited over an approximate area of 10 μm x 3 μm using the protocols shown in Figure 21. A trench was then milled about the Pt deposition area with the sample surface oriented normal to the I-beam. All samples were trenched using a stepped trench technique with an accelerating voltage of 30 keV and an I-beam current of 9.0 nA. An OmniProbe micromanipulator was used to remove the specimen from the sample bulk and then attach the excised sample to a 3-mm diameter Cu TEM half-grid. Each sample was then incrementally thinned to electron transparency (final thickness ≈ 100-150 nm) using the I-beam (specimen surface was oriented perpendicular to I-beam), finishing with an accelerating voltage of 30 KeV and a beam current of 90 pA. The extent of FIB-induced near-surface damage was then quantified by measuring the average damage depth under the Pt layer across the TEM specimen width at ten equidistant points.

To evaluate the efficacy of suggested E-beam Pt deposition thicknesses, Monte Carlo simulations of the Ga^+ ion implantation were conducted using the SRIM software package.[28] Calculations of the Ga^+ ion and recoiled atom distributions were completed using 30 keV Ga^+ ions impinging perpendicular to an amorphous 250-nm thick Pt layer. This layer thickness was utilized to enable the simultaneous evaluation of the likely range of E-beam Pt layer thicknesses (*e.g.* 50-150 nm). The density of the Pt layer was reduced to 7.50 g/cm^3 (~35% of crystalline Pt) based on previous composition measurements of E-beam Pt deposited using $C_9H_{16}Pt$ (~22% Pt, 73% C, and 5% O; in at. %).[29] As the density will likely vary with deposition parameters, in addition to expected improvements in Pt deposition purity as new FIB systems are developed, results are also plotted for calculations which used Pt densities of 4.29 g/cm^3 and 10.72 g/cm^3 (corresponding to ~20 and ~50% of crystalline Pt, respectively) to account for such differences/improvements. The upper-bound density of 50% was selected to reflect that Pt deposited using $C_9H_{16}Pt$ is generally C-rich[30] and no efforts were made in this study to modify the E-beam Pt purity post-deposition.[31]

4.3. Results

TEM micrographs of each Pt deposition condition taken at two different magnifications are shown in Figure 22; three general observations can be made from these micrographs. First, extensive damage (extending greater than 1 μm into the TEM specimen) was observed in Samples 2 and 3 (Figure 22c-d and 22e-f, respectively). Damage is broadly characterized as any microstructural feature which is not observed in the bulk foil; a clear example of such differences is shown in Figure 22e, with the FIB-induced damage indicated by the red arrow. Second, the sample prepared using standard I-beam current values (Sample 1, 90 pA) still exhibits a noticeable damage layer, but the damage depth is significantly less than that found in the "low" I-beam current specimens (Samples 2 and 3.) Third, protocols which utilized the E-beam to deposit an initial layer of Pt before switching to I-beam deposition exhibit minimal damage (Samples 4 and 5) as shown in Figures 2g-h and 22i-j, respectively.
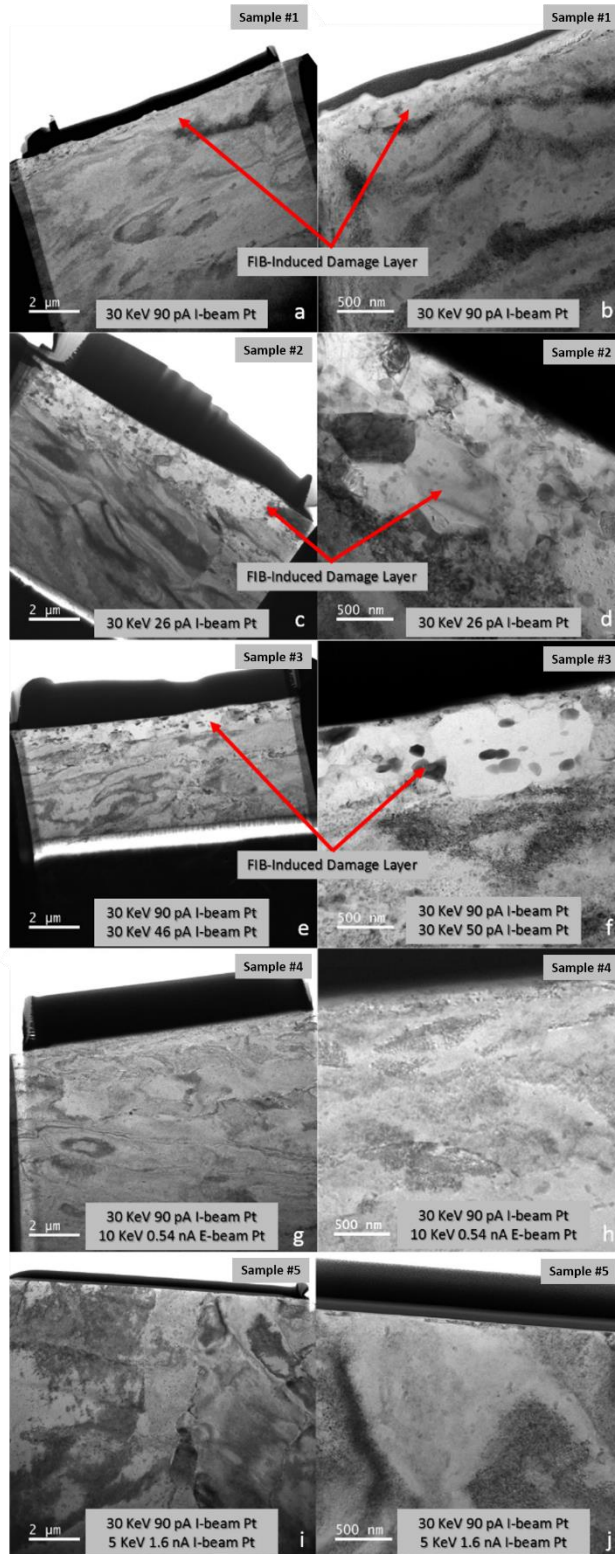
Figure 22 - Overview TEM micrographs at two different magnifications for (a,b) Sample 1, (c,d) Sample 2, (e,f) Sample 3, (g,h) Sample 4, and (i,j) Sample 5.

High-magnification images of the Pt-Al interface for Samples 1 and 4 are shown in Figure 23. These micrographs demonstrate the advantages of using an initial E-beam Pt deposition step (Sample 4; Figure 23b) as the damage is noticeably reduced relative to the I-beam specimen (Sample 1; Figure 23a). Critically, as Sample 1 and 4 were both prepared from Block 1 but have different damage depths, these images suggest that the observed damage layer in Sample 1 is attributable to the Pt deposition process and is not an artifact from other steps in the sample preparation procedure (e.g. the saw cut). Figure 24a shows high magnification images of Sample 5, which was cold-rolled to a 50% thickness reduction and then prepared with a thicker E-beam Pt layer (prior to I-beam deposition) than Sample 4 (~110 vs. ~45 nm for Sample 4). Critically, this sample exhibits a continuous, unaltered microstructure (*i.e.* negligible change/gradient in microstructure), even immediately proximate to the Pt-Al interface, suggesting minimal damage occurred in this specimen during Pt deposition. Additional evidence for a negligible microstructural gradient in Sample 5 is shown in Figure 24b, where the specimen has been tilted to show the deformation substructure proximate to the sample surface. Clearly, the deformation structure appears unaltered up to the Pt-Al interface. Such results indicate that FIB-induced damage was effectively mitigated by the applied E-beam/I-beam Pt deposition strategy. To quantitatively compare the FIB-induced damage depth from the five employed Pt deposition protocols, ten measurements of the damage layer thickness were made at equally spaced intervals across the width of each TEM specimen. The average damage layer for each deposition protocol from these measurements is shown in Figure 25. As expected from the micrographs presented in Figure 22, Samples 2 and 3 exhibit the largest average damage depths (1351 and 825 nm, respectively), which are both deeper than the damage observed in Sample 1 (388 nm). However, these three samples are all significantly elevated compared to the damage found in Samples 4 and 5, which were prepared using the combined E-beam/I-beam Pt deposition strategies (67 and 7 nm, respectively).
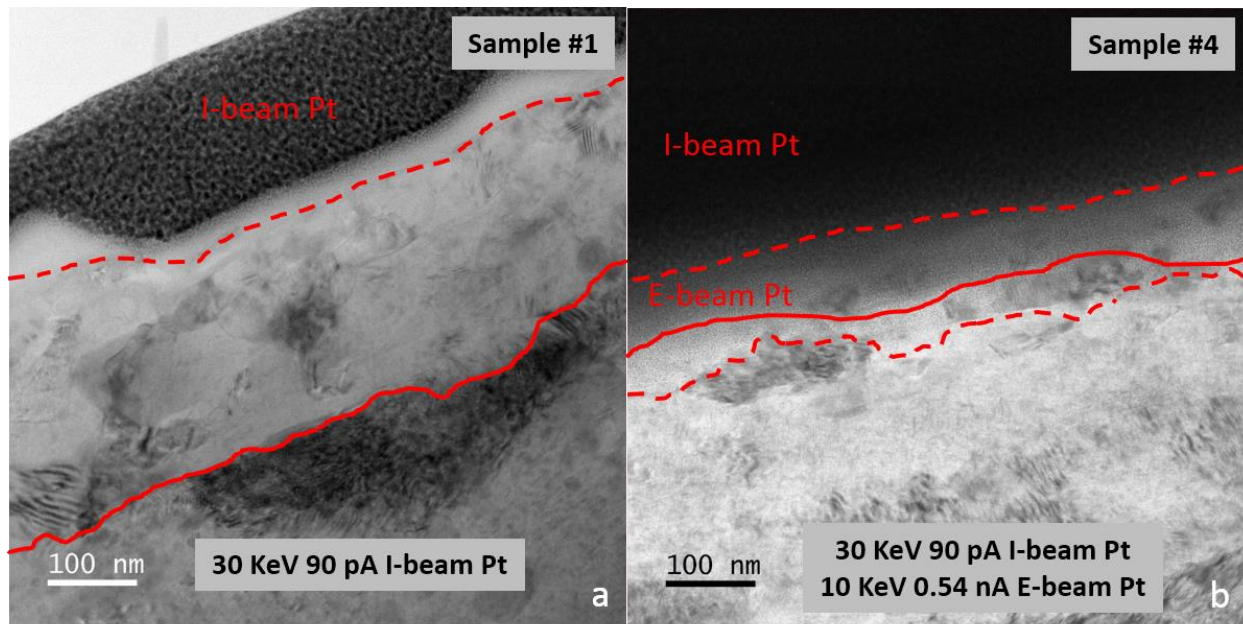
Figure 23 – High magnification TEM micrographs of the Pt/Al interface for (a) Sample 1 and (b) Sample 4. Red lines indicate transition in damage character as well as the location of interfaces between E-beam Pt, I-beam Pt, and the Al alloy.
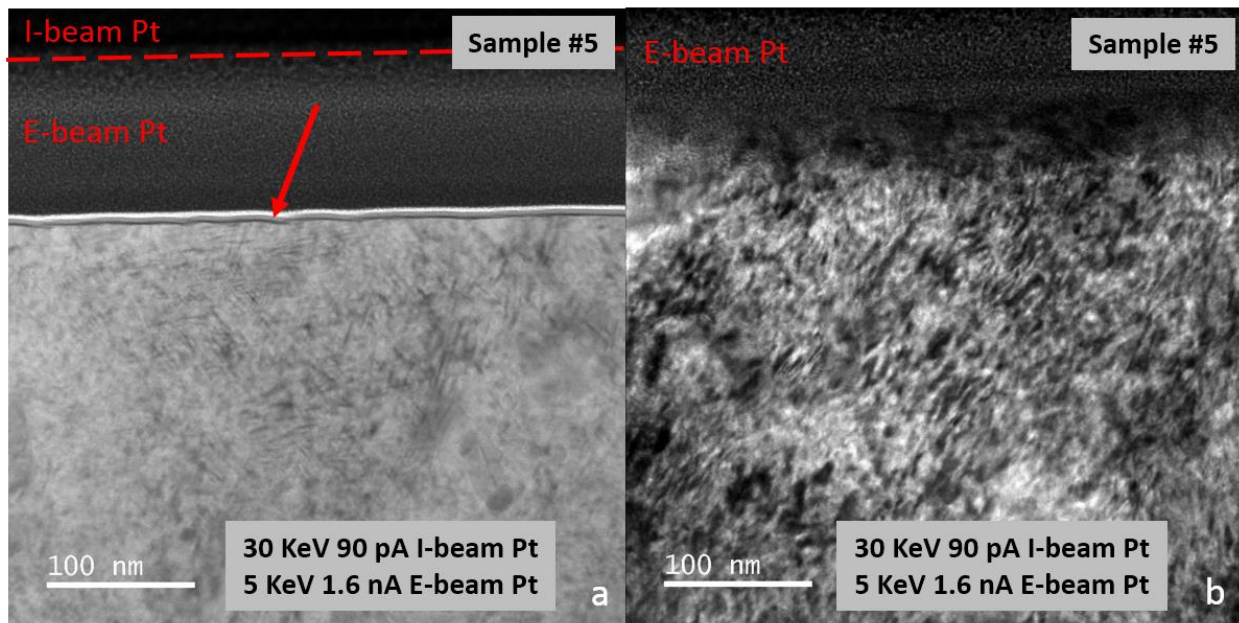
Figure 24 - High magnification TEM micrographs of the Pt/Al interface for (a) Sample 5 un-tilted and (b) Sample 5 tilted to show continuity of deformation. In (a), the red dashed line indicates the transition between the E-beam Pt and I-beam Pt, while the red arrow indicates the 'damage' used for calculating the damage depth shown in Figure 25.
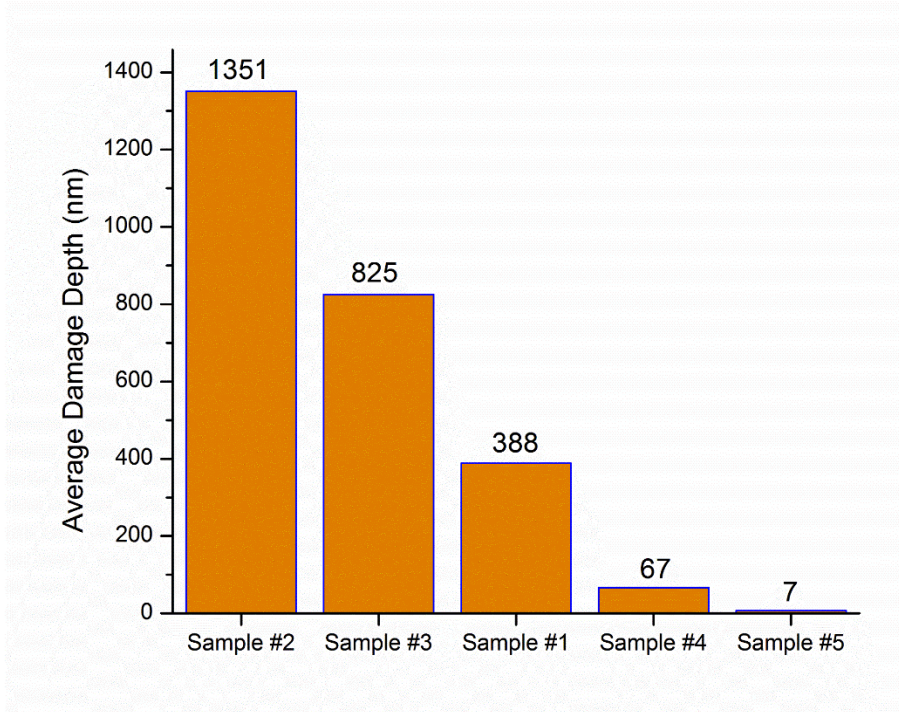
Figure 25 – Average damage depth for each Pt deposition strategy based on ten equidistant measurements across the TEM specimen width.

In addition to the different damage depths, the character of the damage appears to differ between samples. Specifically, a clear gradient in microstructure is observed in Samples 1-3 (Figures 22 and 23a), but not in Samples 4 and 5 (Figures 23b and 24a). In particular, the "high" I-beam current sample (Sample 1) contains an Al material layer that appears to be dislocation and precipitate-free (bright region between red dashed line and I-beam Pt layer in Figure 23a). Conversely, Samples 2 and 3 (Figure 22) do not appear to have such an amorphous region, but instead exhibit a microstructure similar to that expected after recrystallization. Finally, regarding the damage observed in Sample 5 (white and gray layer in Figure 24a, indicated by the red arrow), it is speculated that this "damage" is either an oxide layer or damage induced during polishing prior to Pt deposition. However, as the origin of the damage cannot be rigorously determined, it is conservatively attributed to the FIB for the purposes of this comparison. Additional postulation on the details of the observed microstructure for each specimen is presented in the discussion.

4.4. Discussion

The results shown in Figures 22-25 demonstrate that for AA7075-T651: (1) the damage layer induced in the near-surface region by impinging Ga$^+$ ions during I-beam Pt deposition varies extensively with I-beam deposition parameters, and (2) the use of a combined E-beam/I-beam Pt deposition strategy greatly reduces such damage. In the following discussion, we: (1) qualitatively evaluate the observed damage depth and character for each condition based on the findings of previous studies, and (2) outline the implications of the presented results in the context of efforts to understand near-surface deformation using specimens excised from crack wakes.

4.4.1. Effect of Pt deposition approach on damage depth

The observed dependence of FIB-induced damage depth on Pt deposition strategy for AA7075-T651 shown in Figure 22 (and quantitatively in Figure 25) are consistent with the findings of previous studies. For example, it was expected that the "low" I-beam current specimens would exhibit the largest damage depth. As discussed extensively elsewhere,[32] the advantage of utilizing a "low" I-beam current during Pt deposition is a reduction in the I-beam milling rate. However, the beneficial impact of this decrease in milling rate on the induced damage is countered by a concomitant decrease in the decomposition rate of the Pt precursor gas, which can decrease the Pt layer growth rate. Therefore, while the milling rate is reduced under such "low" I-beam currents, the time required to deposit a Pt layer that is sufficiently thick to stop the impinging Ga$^+$ ions is increased, thereby allowing more damage to accumulate relative to higher I-beam currents.[32] Such a decrease in damage depth with increasing beam current (for modest beam currents; *i.e.* < 100 pA) is consistent with the observed damage depth in Samples 2, 3, and 1 (Figures 22 and 23), where the employed I-beam current was 26, 50, and 90 pA, respectively.

A small number of prior studies have shown that the damage layer induced during I-beam Pt deposition can be reduced by first depositing a Pt layer using the E-beam.[16,30] This use of the E-beam for the initial deposition, while having sufficient energy to decompose the Pt precursor gas (albeit slowly relative to the I-beam), is not expected to induce damage at typical accelerating voltages in an SEM (*i.e.* < 30 keV), especially in metallic specimens. Therefore, as long as the E-beam Pt deposition is made sufficiently thick to stop Ga$^+$ ions from interacting with the specimen, negligible damage should be imparted during the subsequent "finishing" I-beam Pt deposition. Literature suggests that ~50 nm of E-beam Pt is necessary to eliminate I-beam damage in Si,[30] but

the results presented herein indicate that this may not be adequate for AA7075-T651. As shown in Figure 23b, a small layer of near-surface damage (area between the red dashed and solid line) was observed in Sample 4, which contained ~45 nm of E-beam Pt, while no such damage was observed in Sample 5 (despite being more susceptible to possible recrystallization due to an increased dislocation density from cold rolling), which contained ~110 nm of E-beam Pt (Figure 24a). As such, the present results suggest that, while 50 nm of E-beam Pt will certainly reduce I-beam damage, at least 100 nm of E-beam Pt should be deposited to nominally eliminate I-beam damage during Pt deposition at 30 keV on Al alloys. This approach was effective even under conditions where the sample contains significant deformation (Sample 5), as would be the case in a near-fracture surface location.

These experimental observations on the effect of E-beam Pt layer thickness are consistent with the results from Monte Carlo-based simulations of ion implantation from the SRIM software package.[28] Several observations can be made from the calculated normalized distribution of Ga^+ ions as a function of depth, shown in Figure 26. First, it is clear that the peak damage location is between 10-30 nm of the Pt surface, depending on Pt layer density, which indicates that the previously suggested 50-nm thick E-beam Pt layer[30] will shield the underlying specimen from the worst of the Ga^+ ion penetration. Second, in all three cases, a non-negligible fraction of the Ga^+ ions will penetrate beyond 50 nm, thereby implying that a 50 nm E-beam layer thickness is not sufficient to completely preclude damage during subsequent I-beam Pt deposition. Third, an E-beam Pt layer depth of >100 nm is sufficiently thick to effectively stop all Ga^+ ions from reaching the specimen for the most likely E-beam Pt density values (based on composition; between 7.5 and 10.72 g/cm^3)[29]. Finally, the simulation results suggest that an E-beam Pt layer thickness of >150 nm would likely preclude specimen damage at all evaluated density values.
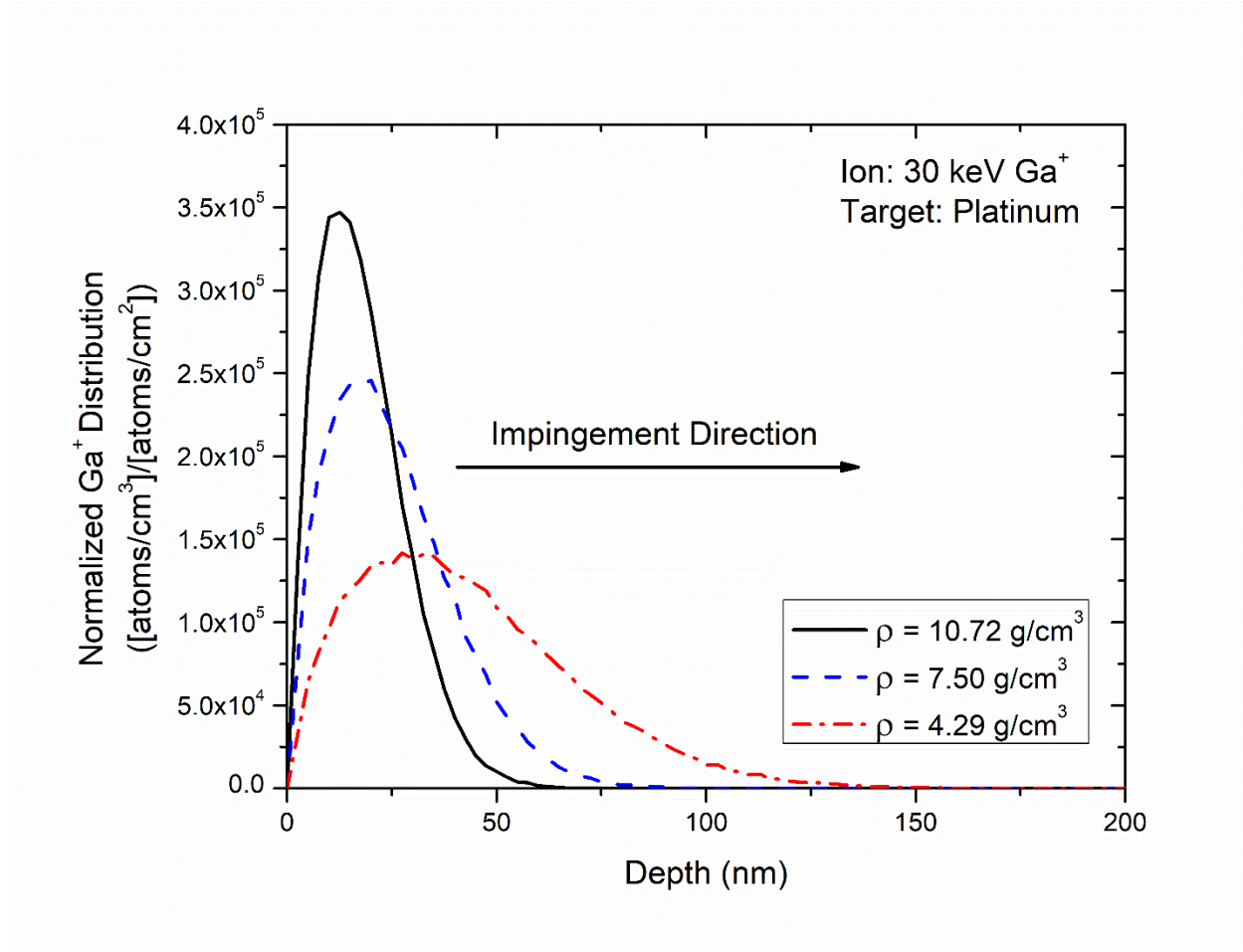
Figure 26 - Normalized Ga+ ion distribution as a function of depth from the Pt surface calculated using Monte Carlo-based simulations for three different Pt density values. Calculations were completed using 30 keV Ga+ ions impinging from a source oriented perpendicular to the Pt layer surface.

4.4.2. Effect of Pt deposition approach on damage character

The focus of the current study is to evaluate the efficacy of various Pt deposition strategies in preventing damage; as such, an extensive damage characterization effort is outside of the scope of the current work. However, it is pertinent to note the apparent variations in damage character with Pt deposition parameters. Considering the micrographs presented in Figure 22d and 22f (Sample 2 and 3, respectively), the presence of nominally equiaxed grains (as opposed to the pancake-type grains expected in a rolled AA7075 microstructure) suggests that the near-surface region has recrystallized in the "low" I-beam current specimens – an inference which is supported by the apparent reduction in deformation relative to the bulk material observed deeper in the TEM

foil. Conversely, the specimen prepared using only a 30 keV, 90 pA I-beam deposition (Sample 1) exhibits two "layers" of damage. As shown in Figure 23a, a region which appears to be completely dislocation-free and likely amorphous (area between I-beam Pt and dashed red line in Figure 23a) can be found immediately adjacent to the Pt-Al interface. Beneath this first layer, a second region is observed that also appears to have a reduced dislocation density relative to the bulk foil, as was found on Samples 2 and 3. These observations suggest that the near-surface region of specimens prepared using only I-beam Pt deposition strategies can be appreciably modified. Moreover, the variation in damage character, despite each TEM sample being excised in an identical manner from the same region of the bulk specimen and finished with a sufficiently thick Pt layer to avoid damage during milling, implies that the noted damage is likely due to the differences in I-beam Pt deposition parameters. That such microstructural changes occur *during* the I-beam Pt deposition process is significant as I-beam Pt deposition is most commonly used for preventing FIB-induced damage during milling.

Literature suggests that this recovery/recrystallization of the near-surface region may be due to irradiation effects and/or thermal effects.[4,11,33] Concerning the former, irradiation of Cu with Ga^+ ions for 360 seconds at 30 KeV and 30 pA resulted in recrystallization and grain growth in the irradiated surface region as well as the development of a strong <110> texture.[11] Based on these results, it was suggested that recrystallization/grain growth is driven by the orientation-dependence of ion channeling. Specifically, grains which have a non-channeling orientation will have increased interactions with the ion beam, thereby resulting in an increased generation of defects with such grains. As the defect density is locally increased, there is an appreciable increase in free energy in the non-channeling grains, which is then relieved through the growth of grains that are well-oriented for channeling. Considering thermal effects, it has been suggested that impinging Ga^+ ions can cause localized heating of the specimen surface, which may be sufficient to induce recovery and recrystallization. For example, it was reported that the brief irradiation of Au/Ni bilayers with 30 keV Ga^+ ions during specimen placement resulted in microstructural variations equivalent to annealing the specimen for several minutes at 400°C.[33] However, while either of these processes may be active (or even work synergistically) during ion impingement, decoupling the relative influence of these two potential contributions is complicated by their likely simultaneous nature. Critically, such complications in determining the source of observed damage

will also obfuscate evaluating damage-like features that may have been present prior to TEM sample preparation.

Examination of the damage near the Pt-Al interface in samples prepared using the combined E-beam/I-beam strategy (Figures 23 and 24) suggests that such irradiation and/or thermal effects can be neutralized if a sufficiently thick E-beam Pt layer is deposited. In particular, a sample which was severely deformed so as to contain an increased dislocation density (and therefore have increased sensitivity to recovery/recrystallization) exhibited a continuous microstructure even immediately adjacent to the Pt-Al alloy interface. Tilting of the TEM foil (Figure 24b) confirms the continuity of strong contrast (likely due to deformation), even proximate to the interface, thereby corroborating the assessment that a sufficiently thick E-beam Pt layer can eliminate near-surface damage induced during I-beam Pt deposition. Moreover, the results of Monte Carlo-based simulations (presented in Figure 26) indicate that an E-beam Pt layer of >100 nm is sufficiently thick to effectively prevent the interaction between Ga^+ ions and the underlying specimen. Such mitigation of these specimen-ion interactions has important implications for preparing TEM samples from near-surface regions.

4.4.3. Implications on the characterization of near-surface microstructure

Despite its inherent simplicity and widespread availability, the use of E-beam Pt as a mitigation scheme is not well-documented in the FIB damage literature nor is it widely employed in microstructural studies that utilize FIB milling for TEM sample preparation. For example, several recent studies have sought to employ FIB milling as a means by which to examine the near-fracture surface region of specimens exposed to aggressive environments so as to better understand the deformation processes governing material failure.[18,34–36] In particular, FIB extraction of TEM specimens from the crack wake has been employed as a means to evaluate the role of hydrogen in causing premature fracture of metallic structural components *via* TEM characterization of the dislocation structure.[37] It has been hypothesized that the processes responsible for this "hydrogen embrittlement" phenomenon (and other fracture processes) occur close to the crack tip (< 1 μm),[38] indicating that damage induced during I-beam Pt deposition could complicate the interpretation of such experiments. Examination of methods employed in these studies reveals a consistent use of only I-beam Pt deposition strategies, as well as possible evidence of near-surface damage in FIB-prepared specimens (often observed as a bright white line immediately beneath the surface; similar

to that shown in Figure 23a). Conversely, other studies have employed a "low" I-beam current during Pt deposition to reduce the observed damage;[35] the current results (Figure 22d and 22f) demonstrate that such a protocol induces more extensive damage than the typically utilized I-beam current of 90 pA. Conversely, the current study demonstrates that an E-beam/I-beam Pt deposition strategy enables unambiguous characterization of the damage structure in the high interest region within 100 nm of the crack surface. Such a protocol could enable additional mechanistic insights relative to prior efforts where the experimental complications associated with Pt induced damage forced analysis of "bulk" microstructures further away from the Pt deposition region.[36] In conclusion, the present results demonstrate that the combined E-beam/I-beam strategy can be utilized to enable rigorous characterization of these near-surface regions.

4.5. Conclusions

The influence of Pt deposition strategy on the damage induced in the near-surface region of FIB-prepared specimens of AA7075-T651 was systematically examined using transmission electron microscopy, resulting in several important insights:

1. The depth and character of damage induced during I-beam Pt deposition was found to strongly depend on the employed deposition parameters for AA7075-T651.

2. The use of a combined E-beam/I-beam Pt deposition strategy, in which ~110 nm of Pt was initially deposited using the E-beam, was found to effectively eliminate damage during I-beam Pt deposition in AA7075-T651. This observation is consistent with the results of Monte Carlo-based modeling of ion implantation.

3. Mitigation of this near-surface damage suggests that the combined E-beam/I-beam Pt deposition strategy could be employed to enable the examination of near-surface damage processes in AA7075-T651. This efficacy of this deposition strategy is expected to extend to other alloy systems.

4.6. Suggestions for future study

Just as the development of the FIB instrument was driven by the semiconductor industry, so was the new instrumentation development utilizing a xenon plasma source instead of a gallium ion (Ga^+) source known as a plasma focus ion beam (PFIB), enabling faster milling rates. Xenon ions (Xe^+) are larger, thus theoretically providing a more efficient material removal rate while

imparting less damage than Ga^+ ions. A comparative study which prepared samples via a Ga^+ ion FIB and a Xe^+ PFIB, examined the mechanical properties of a high-entropy alloy via in situ tensile straining TEM.[39] The study found differences due to the small ion-irradiated volumes and insignificant alloying effect brought on by the PFIB sample preparation.[39] How this translates to other metal materials like AA7075-T651, specifically for TEM sample preparation isn't fully understood. Doing a comparative study similar to which was performed in this chapter, but utilizing a PFIB would provide insights to the utilization of this new tool as it pertains to TEM sample preparation of materials like AA7075-T651.

4.7. Acknowledgements

4.8. References

1. Stevie, F. A., Griffis, D. P. & Russell, P. E. *Introduction to Focused Ion Beams: Instrumentation, Theory, Techniques and Practice*. (Springer Science+Business Media, Inc., 2005).

2. Munroe, P. R. The application of focused ion beam microscopy in the material sciences. *Mater. Charact.* **60**, 2–13 (2009).

3. Yao, N. *Focused Ion Beam Systems: Basics and Applications*. (Cambridge University Press, 2007).

4. Kato, N. I. Reducing focused ion beam damage to transmission electron microscopy samples. *J. Electron Microsc. (Tokyo).* **53**, 451–458 (2004).

5. Mayer, J., Giannuzzi, L., Kamino, T. & Michael, J. TEM Sample Preparation and FIB-Induced Damage. *MRS Bull.* **32**, 400–407 (2007).

6. Giannuzzi, L. A. & Stevie, F. A. A review of focused ion beam milling techniques for TEM

specimen preparation. *Micron* **30**, 197–204 (1999).

7. Lee, S. *et al.* FIB-induced dislocations in Al submicron pillars: Annihilation by thermal annealing and effects on deformation behavior. *Acta Mater.* **110**, 283–294 (2016).

8. Phaneuf, M. W., Li, J. & Casey, J. D. Gallium phase formation in Cu and other FCC metals during near-normal incidence Ga-FIB milling and techniques to avoid this phenomenon. *Microsc. Microanal.* **8**, 52–53 (2002).

9. Yu, J., Liu, J., Zhang, J. & Wu, J. TEM investigation of FIB induced damages in preparation of metal material TEM specimens by FIB. *Mater. Lett.* **60**, 206–209 (2006).

10. Kiener, D., Motz, C., Rester, M., Jenko, M. & Dehm, G. FIB damage of Cu and possible consequences for miniaturized mechanical tests. *Mater. Sci. Eng. A* **459**, 262–272 (2007).

11. Michael, J. R. Focused Ion Beam Induced Microstructural Alterations: Texture Development, Grain Growth, and Intermetallic Formation. *Microsc. Microanal.* **17**, 386–397 (2011).

12. Babu, R. P., Irukuvarghula, S., Harte, A. & Preuss, M. Nature of gallium focused ion beam induced phase transformation in 316L austenitic stainless steel. *Acta Mater.* **120**, 391–402 (2016).

13. Knipling, K. E., Rowenhorst, D. J., Fonda, R. W. & Spanos, G. Effects of focused ion beam milling on austenite stability in ferrous alloys. *Mater. Charact.* **61**, 1–6 (2010).

14. Kempshall, B. W., Giannuzzi, L. A., Prenitzer, B. I., Stevie, F. A. & Da, S. X. Comparative evaluation of protective coatings and focused ion beam chemical vapor deposition processes. *J. Vac. Sci. Technol. B Microelectron. Nanom. Struct.* **20**, 286 (2002).

15. Langford, R. M. & Petford-Long, A. K. Preparation of transmission electron microscopy cross-section specimens using focused ion beam milling. *J. Vac. Sci. Technol. A Vacuum, Surfaces, Film.* **19**, 2186–2193 (2001).

16. Lipp, S. Investigations on the topology of structures milled and etched by focused ion beams. *J. Vac. Sci. Technol. B Microelectron. Nanom. Struct.* **14**, 3996 (1996).

17. Martin, M. L. A New Approach to Discovering the Fundamental Mechanisms of Hydrogen Failure. (University of Illinois at Urbana-Champaign, 2013).

18.   Wang, S., Nagao, A., Sofronis, P. & Robertson, I. M. Acta Materialia Hydrogen-modified dislocation structures in a cyclically deformed ferritic-pearlitic low carbon steel. *Acta Mater.* **144**, 164–176 (2018).

19.   Gangloff, R. P. H-enhanced deformation and fracture in the crack tip process zone. in *2016 International Hydrogen Conference* 1–35 (2016).

20.   Huang, J., Loeffler, M., Moeller, W. & Zschech, E. Ga contamination in silicon by Focused Ion Beam milling: Dynamic model simulation and Atom Probe Tomography experiment. *Microelectron. Reliab.* **64**, 390–392 (2016).

21.   McCaffrey, J. P., Phaneuf, M. W. & Madsen, L. D. Surface damage formation during ion-beam thinning of samples for transmission electron microscopy. *Ultramicroscopy* **87**, 97–104 (2001).

22.   Rubanov, S. & Munroe, P. R. FIB-induced damage in silicon. *J. Microsc.* **214**, 213–221 (2004).

23.   Chandler, C. (FEI) & Megorden, M. (FEI). Platinum Deposition Technical Note. 52 (2007).

24.   Vermeij, T., Plancher, E. & Tasan, C. C. Preventing damage and redeposition during focused ion beam milling: The "umbrella" method. *Ultramicroscopy* **186**, 35–41 (2018).

25.   Unocic, K. A., Mills, M. J. & Daehn, G. S. Effect of gallium focused ion beam milling on preparation of aluminium thin foils. *J. Microsc.* **240**, 227–238 (2010).

26.   Burns, J. T., Larsen, J. M. & Gangloff, R. P. Driving forces for localized corrosion-to-fatigue crack transition in Al-Zn-Mg-Cu. *Fatigue Fract. Eng. Mater. Struct.* **34**, 745–773 (2011).

27.   Papazian, J. *et al. DARPA/NCG structural integrity prognosis system, HR0011-04-C-0003*. (DARPA, 2009).

28.   Ziegler, J. F., Ziegler, M. D. & Biersack, J. P. SRIM - The stopping and range of ions in matter (2010). *Nucl. Instruments Methods Phys. Res. Sect. B Beam Interact. with Mater. Atoms* **268**, 1818–1823 (2010).

29.   Yavas, O. *et al.* Field emitter array fabricated using focused ion and electron beam induced reaction. *J. Vac. Sci. Technol. B Microelectron. Nanom. Struct.* **18**, 976 (2000).

30. FEI Company. *Platinum Deposition Technical Note (PN 4035 272 21851-D)*. (2007).

31. Villamor, E., Casanova, F., Trompenaars, P. H. F. & Mulders, J. J. L. Embedded purification for electron beam induced Pt deposition using MeCpPtMe3. *Nanotechnology* **26**, (2015).

32. Yao, N. *Focused ion beam systems: basics and applications*. *Science And Technology* (2007). doi:10.1017/CBO9780511600302

33. Cen, X. & van Benthem, K. Ion beam heating of kinetically constrained nanomaterials. *Ultramicroscopy* **186**, 30–34 (2018).

34. Wang, S., Nagao, A., Edalati, K., Horita, Z. & Robertson, I. M. Influence of hydrogen on dislocation self-organization in Ni. *Acta Mater.* **135**, 96–102 (2017).

35. Martin, M. L., Somerday, B. P., Ritchie, R. O., Sofronis, P. & Robertson, I. M. Hydrogen-induced intergranular failure in nickel revisited. *Acta Mater.* **60**, 2739–2745 (2012).

36. Ro, Y. J., Agnew, S. R. & Gangloff, R. P. Effect of Environment on Fatigue Crack Wake Dislocation Structure in Al-Cu-Mg. *Metall. Mater. Trans. A* **43A**, 2275–2292 (2012).

37. Robertson, I. M. *et al.* Hydrogen Embrittlement Understood. *Metall. Mater. Trans. B* (2015). doi:10.1007/s11663-015-0325-y

38. Gangloff, R. P. H-Enhanced Deformation and Fracture in the Crack Tip Process Zone. in *Material Performance in Hydrogen Environments: Proceedings of the 2016 International Hydrogen Conference* (eds. Somerday, B. P. & Sofronis, P.) 1–35 (ASME Press, 2016).

39. Liu, J. *et al.* Effect of Ion Irradiation Introduced by Focused Ion-Beam Milling on the Mechanical Behaviour of Sub-Micron-Sized Samples. *Sci. Rep.* **10**, 1–8 (2020).

Chapter 5 – The development of a novel multi-length scale characterization protocol

The following chapter is a scaled down version of the publication made from the discussed study. The publication for this chapter can be found in Appendix B.

5.1. Overview

5.1.1. Introduction to the development of the multi-scale characterization protocol

Prior FIB/TEM studies have provided important insights regarding the contribution of microscale deformation processes to environmental mechanisms such as H embrittlement, but several obfuscating factors complicate the incorporation of the results into micromechanical models. First, the inherent grain-to-grain variation in dislocation patterning size is not insignificant, with Keller et al. reporting standard deviations reaching between 30 and 50% of the mean cell diameter (depending on location in the specimen and strain level) for monotonically deformed Ni.[1] This variability in patterning is likely attributable to (1) differences in the relative orientation of slip planes to the loading axis as the grain orientation is changed and (2) variations in the level of constraint induced by neighboring grains.[2] As such, the development of mechanistic insights from dislocation patterning data obtained (1) from a limited set of observations and (2) without identification of the grain orientations observed in TEM samples obtained from different specimens must be done cautiously. These challenges are likely responsible for the inconsistent reports regarding topics such as H effects on the evolution of dislocation cell size in strained nickel alloys, with several studies on this topic indicating either a minimal influence[3–5] or a more salient role of H[6–8], respectively. Second, ambiguities regarding the mechanical driving force present at the location of the FIB extraction from the fracture surface in prior studies[9,10] also obfuscates interpretation of the observed dislocation patterning as it is well established that the dislocation cell size is dependent on the applied stress.[11] More recent studies have sought to precisely conduct FIB extractions from fracture mechanics specimens at locations that experienced identical stress intensity (K, which can be considered the continuum-scale mechanical driving force for crack growth)[12] values.[13–15]. Such efforts are an important first step in mitigating this complication, but the importance of quantifying the continuum and local mechanical loading conditions should not be neglected. Lastly, though TEM enables the direct observation of the local dislocation patterning at high resolution, the area sampled during typical TEM characterization is typically less than tens

of μm². Given this areal limitation, the observed statistical variation in dislocation cell diameter within a single specimen, and the complications induced by grain orientation and other microstructural features, the development of globally representative mechanisms via TEM alone is non-trivial. These challenges motivate the use of characterization techniques that enable the assessment of deformation behavior at larger length scales, particularly if such methods can preserve < 100 nm-level resolution.

The need for a multiscale characterization approach for assessing the interaction between H and deformation is widely recognized in the literature, with a number of recent reports documenting the coupling of standard electron backscatter diffraction (S-EBSD), electron contrast channeling imaging (ECCI), TEM/FIB, and even x-ray techniques.[7,13–22] In addition to these techniques, high resolution electron backscatter diffraction (HREBSD), which can be leveraged to calculate geometrically necessary dislocation (GND) densities via cross-correlation techniques,[23,24] offers promise as a complementary technique to TEM for assessing localized deformation due to an attractive combination of spatial resolution (> 75 nm) and sampling area (≈ 100–10,000 s of μm²).[25–27] This approach has been extensively applied to characterize deformation distributions induced by a wide range of processes, including: near-notch cracks in AA6061 [28], indentations in Ta,[29] Cu deformed in tension,[30] blocked slip bands in Ti,[31] thermal stress effects from carbides in a Ni-base superalloy,[32] after fatigue in Ti-6Al-4V,[33] and from microstructurally small crack growth from inclusions in a Ni-based superalloy.[34] However, despite this robust literature precedent, the use of HR-EBSD to assess deformation distributions pertinent to H-assisted cracking is limited.

The objective of this study was to evaluate the efficacy of a multiscale characterization approach utilizing S-EBSD, HR-EBSD, and FIB/TEM to assess the deformation pertinent to hydrogen environment-assisted cracking (HEAC) in a model Ni-base superalloy. First, a "global" understanding of the mechanical driving force (defined by the applied K) and microstructure for three regions proximate to the fracture surface is developed via fracture mechanics analysis and S-ESBD. The microscale deformation character for these three regions is assessed using GND density maps obtained using HR-EBSD, which are then qualitatively compared to the dislocation patterning observed via FIB/TEM.

5.2. Experimental Methods

5.2.1. Material and fracture mechanics-based testing

This study was conducted on a peak-aged Monel K-500 (UNS N05500) single edge notch tension (SEN(T)) specimen that was previously tested using a slow-rising K methodology while immersed in 0.6 M NaCl at an applied potential of -1200 mV$_{SCE}$. Prior work on Monel K-500 demonstrates that the alloy is highly susceptible to HEAC under this applied potential and environment combination.[35–40] Details of the specimen microstructure, heat treatment, mechanical properties, and composition are reported elsewhere.[36]

Fracture mechanics testing at a monotonically increasing elastic K (dK/dt) was achieved by coupling active crack length feedback *via* the direct current potential difference (dcPD) technique[41] with software-controlled, servo-hydraulic actuator displacement. The current experiment was completed at a constant dK/dt = 0.33 MPa√m/hr, with the grip displacement adjusted every 15 seconds to maintain the specified dK/dt. The crack length was calculated from the dcPD-measured potentials using Johnson's equation,[42] where the adjustable constant (V_0) is the potential associated with the initial notch depth (a_0).[43] A post-test correction for false crack growth due to crack surface electrical contact enabled by cathodic polarization-induced destabilization of the crack wake surface oxide film and localized plasticity was performed as has been previously described.[37,44] The effects of plasticity on the fracture driving force were also accounted for through the calculation of a total stress intensity (K_J) *via* established J-integral procedures. Details of the J analysis procedure[45] as well as the specific testing approach utilized for the specimen evaluated in the current study are presented elsewhere.[36]

5.2.2. Specimen preparation

The fracture surface of the specimen was excised from the gage section using a low-speed cutoff saw, with the saw cut performed > 3 mm from the fracture surface to prevent the introduction of extraneous deformation. As schematically shown in Figure 27, after the fracture surface was excised, the specimen height was progressively thinned to a final thickness of 0.6 mm using SiC papers and diamond slurries, with a finishing polish of 1 μm diamond slurry (Figure 27a). Extensive care was taken to minimize polishing-induced damage by removing at least 3x the average particle size of the preceding SiC grinding paper before advancing to next grit size. For example, since the supplier-reported average particle size for the 400-grit SiC paper is ~22 μm, a

94

minimum of 70 μm was removed using the 600-grit SiC paper before advancing to the 800-grit SiC paper. A similar strategy was employed to reduce the specimen thickness from ~2.68 mm to 1.4 mm (Figure 27b). This targeted value of 1.4 mm corresponded to the centerline of the specimen and was selected to ensure the evaluation of deformation in a region that was under plane strain conditions.[46] Final dimensions of the specimen post-polish were ~1.4 mm x 12.5 mm x 0.6 mm (W x L x H), as shown in Figure 27d. An argon broad-beam ion mill (Hitachi IM4000) was then utilized to expose a cross-section of material at a surface condition suitable for EBSD, with the depth of the ion mill trench positioned so as to be sufficiently deep (>3 μm) to remove any residual damage induced by the final 1 μm diamond polish (Figure 27c).
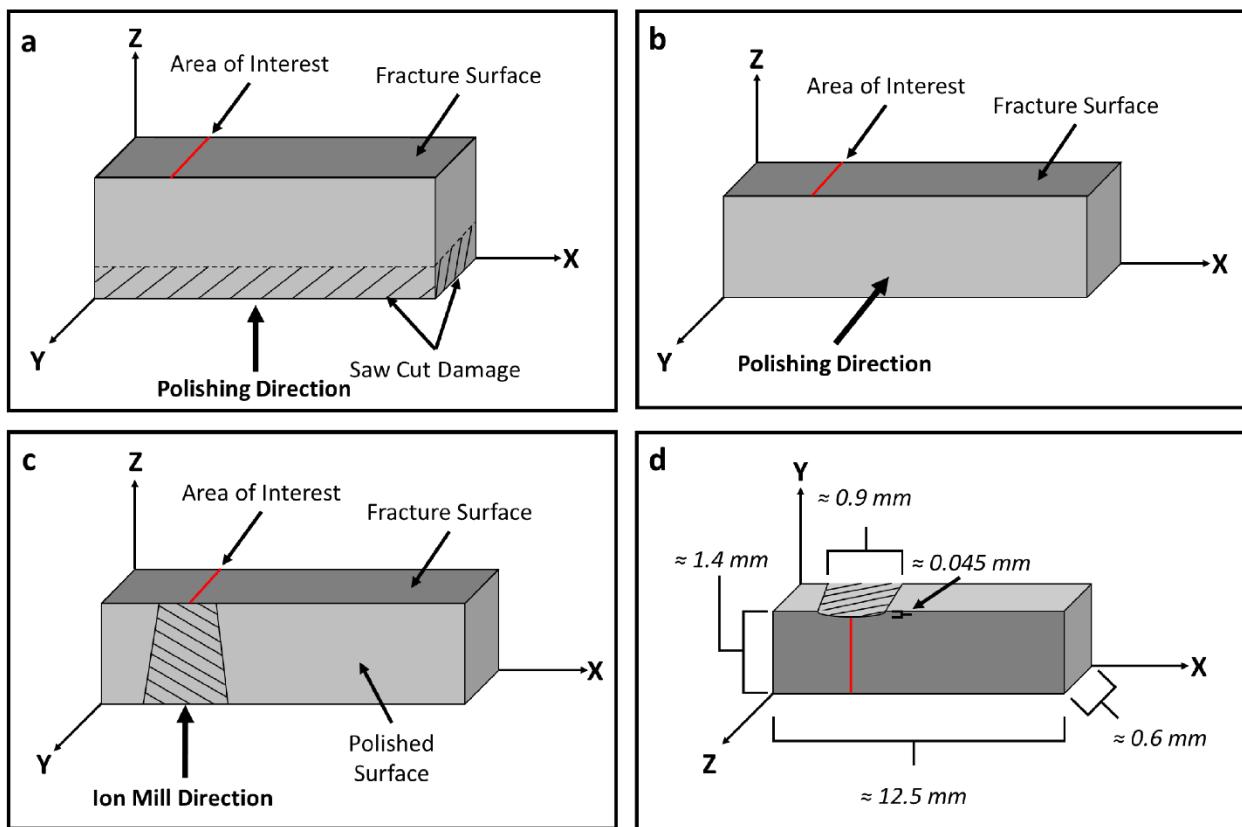
Figure 27 - Overview of the specimen preparation procedure. (a) First, after the fracture surface has been excised from the gage section of the test specimen, the bottom of the sample is polished (in the +Z direction) until the specimen is ~ 0.6 mm thick. (b) The sample is then polished in the -Y direction to the midplane of the fracture surface, thereby ensuring that the evaluation region was loaded in plane strain conditions. (c) After the two thinning steps are completed, the specimen is then cross-sectioned using an ion mill such that the ions impinge on the bottom of the sample in the +Z direction. Final dimensions of the prepared sample are shown in (d).

The advantage of this cross-section approach is the ability to (1) expose the region proximate to the crack wake with minimal exposure to the ion beam and negligible edge rounding, thereby facilitating characterization to within 300-500 nm of the fracture surface and (2) precisely expose a region at a specific crack length so as to evaluate the deformation behavior at a specific K of interest. During milling, the specimen was oriented such that the ion beam impinged on the bottom surface of the specimen, in a direction perpendicular to the fracture surface. As localized heating of the specimen is expected during broad-beam ion milling, an EBSD study (not shown) was conducted using cold-rolled Monel K-500 prepared using the above polishing procedure to inform the optimal cross-sectioning parameters. Characterization of the specimen before and after ion milling revealed no observable effect on the kernel average misorientation (KAM) or grain structure for a two-hour cross-section mill completed using an accelerating voltage of 6 keV (which was sufficient to mill through the ~600 μm thickness of the specimen). Typical "cross-section" dimensions using this accelerating voltage and milling time are 800-1000 μm in width and between 25-75 μm in height.

5.2.3. Characterization

Both S-EBSD and HR-EBSD were conducted using a FEI Helios G4 UC FIB/SEM equipped with an Oxford Symmetry EBSD detector. All scans utilized an accelerating voltage of 30 keV and probe current of 3.2 nA, with the primary difference between each scan being the step size and magnification. S-EBSD was performed at a magnification of 200x with a 750 nm step size and 2x2 binning of the EBSD camera pixels to provide a "global" or bulk perspective. HR-EBSD scans were conducted at two magnifications: (1) 800x at a step size of 150 nm and 2x2 binning to provide a 'neighborhood' perspective and (2) 6000x at a step size of 75 nm and 2x2 binning to provide a local, complementary scan to compare to excised FIB/TEM specimens. While 1x1 binning is typically preferred for HR-EBSD calculations, Jiang *et al.* demonstrated that the binning effect on calculated GND density was negligible between 1x1 (no binning) and 2x2 binning.[26] In addition to the binning mode, it has been demonstrated that the step size utilized in HR-EBSD scans can have important effects on both the observed distribution and magnitude of calculated GND density values.[26,47] However, as demonstrated by Ruggles *et al.*,[47] the relationship between employed step size and GND density exhibits a "plateau" between ~70 and 1 μm, where the calculated GND density is nominally independent of the step size. As such, it is expected that

the two step sizes employed in the current study should yield similar distributions and magnitudes of GND density.

The primary difference between HR-EBSD and S-EBSD is the 1-2 order of magnitude improvement in angular resolution for HR-EBSD, which arises from the use of cross-correlation methods as opposed to the traditional Hough transform approach for analyzing Kikuchi patterns.[23] In the current study, the commercial cross-correlation analysis software, CrossCourt 4, was employed to generate maps of the GND density from the HR-EBSD scans. Full details of this analysis methodology are presented by Britton and coworkers, but are briefly summarized below.[23,24] First, reference patterns to which each pixel (for a given grain) will be compared are selected based on pattern quality, with various elimination criteria employed as necessary to improve reference selection (*e.g.* a minimum KAM value) Given that strain-free references for each grain/sub-grain were not collected for this work (since a strain-free location does not exist within the sample area of interest proximate to the crack path), all calculated values should be considered relative as opposed to absolute. Additionally, as HR-EBSD only calculates the GND density (it does not assess the statistically stored dislocation density), the calculated values should also be considered a lower-bound for the total dislocation density. Once a suitable set of reference patterns is selected, the camera area is divided into regions of interest (ROIs), with the number of ROIs used in the calculation selected based on a balancing of reduced error and increased computational times. In the current study, 40 ROIs were used. Next, the cross-correlation function of each ROI is calculated, resulting in a "cross-correlation function peak". The relative shift in this peak between each of the reference and sample ROIs is then utilized to generate the deformation gradient tensor for the Kikuchi pattern of interest, which can then be used to calculate the strain and rotation relative to the reference pattern. Additional passes using a remapping procedure, which correct for errors induced by large rotations between the reference and test pattern, were then be employed to improve calculation quality.[24] Once these shifts are known, the local curvature about the pixel of interest can then be calculated, which is then related to the GND density *via* the Nye tensor.[23]

TEM specimens were excised from the fracture surface utilizing a FEI Helios G4 UC FIB/SEM. To prevent FIB-induced damage and/or alteration of the microstructure during TEM sample preparation, a two-step Pt deposition sequence was employed that was previously shown

to prevent such near-surface damage during Pt deposition and FIB milling of Al alloys.[48] After completion of the Pt deposition, the TEM specimen was excised from the fracture surface using standard FIB practices and then attached to a Cu TEM half-grid using a FEI EasyLift micromanipulator.[48] All TEM specimens were examined in a FEI Titan scanning/transmission electron microscope (S/TEM) equipped with a double-tilt holder and operated at 300 keV in bright field scanning TEM (BF-STEM) mode (camera length of 2.4 m). Each TEM specimen was imaged with the specimen center aligned to the <110> zone axis so as to enable (1) a common imaging condition across the excised specimens and (2) imaging under conditions where many dislocation types can be observed for comparison with calculated GND maps.[49]

5.3. Results

A lateral micrograph of the crack path for the region of interest within the milled cross-section is shown in Figure 28a, with the red boxes indicating three locations that will be excised from the fracture surface using FIB for evaluation in the TEM. The inverse pole figure map corresponding to this location is shown in Figure 28b. It should be noted that these IPF data are presented as-collected (*i.e.* noise reduction techniques to remove zero solutions *were not* employed); the high indexing ratio indicates that the surface finish within the ion mill cross-section is sufficient for EBSD despite evidence of curtaining in Figure 28a. The K_J versus crack length relationship for this region is shown in Figure 28c, with the K_J corresponding to the centerline of each indicated area noted by the respective dashed line (Area 1: ~42.3 MPa√m, Area 2: ~44.3 MPa√m, and Area 3: ~46.0 MPa√m, respectively; this range of applied mechanical driving force is considered to be qualitatively similar). Note that the endpoints of the plotted K_J versus crack length data correspond to the edges of the micrograph shown in Figure 28a. Utilizing the S-EBSD data, the degree of deformation can be nominally quantified *via* the KAM distribution, which is calculated using the mean of the misorientation within a group of pixels. Since plastic deformation induces rotations in the lattice, it can be inferred that regions exhibiting increased KAM values underwent more plastic deformation.[50] Examination of the KAM map for the region of interest, shown in Figure 28d, suggests that deformation was localized to within ~25 μm of the fracture surface, with the KAM decreasing to a constant value of effectively 0° beyond this depth from the crack path. To quantify the degree of deformation localization, the observed 25 μm depth can be compared to the plane strain plastic zone size, which may be estimated from the applied K and

material yield strength.[36] Prior work demonstrated that the yield strength of the employed peak-aged alloy was ~570 MPa. As such, given an average applied K ≈ 44 MPa√m for the three locations, the plastic zone size is calculated as ~630 μm, indicating that the deformation is localized to within ~4% of the plastic zone size.

The apparent localization of deformation to the crack path observed *via* KAM is corroborated by GND maps calculated from HR-EBSD scans. As shown in Figure 29, the GND density nominally decreases with increasing distance from the crack path, reaching a "bulk" level (~10^{14} m^{-2}) after 30-45 μm (~5-7% of the plastic zone size). Additionally, the GND map also suggests that the distribution and intensity of deformation varies strongly from grain-to-grain along the crack path, as demonstrated by a qualitative examination of the two adjacent grains indicated by the red arrows in Figure 29. Specifically, the left grain exhibits a lower GND density which is fairly uniform throughout the grain, with slight elevations in GND density as grain boundaries are approached. Conversely, while the GND density distribution is more heterogeneous in the right grain, several bands exhibit GND densities that are nearly an order of magnitude higher than the average GND density in the left grain.
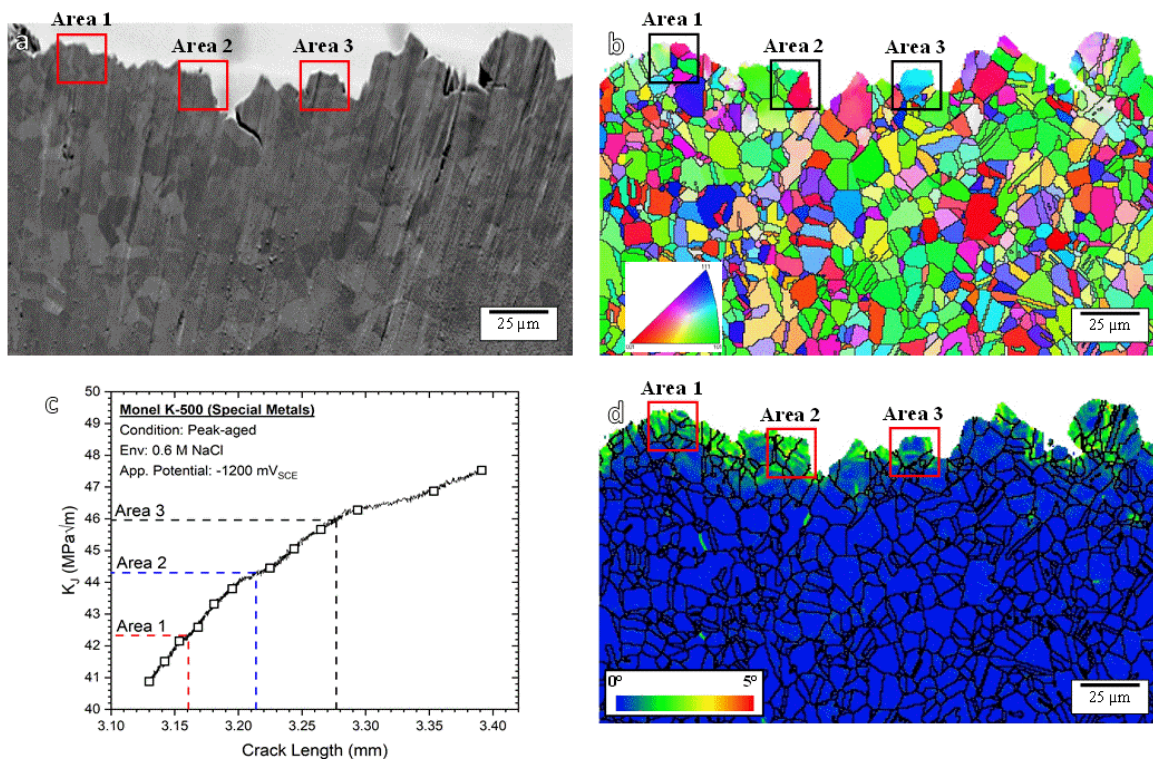
Figure 28 - (a) Micrograph of the region of interest within the ion milled cross-section, with areas for subsequent FIB/TEM analysis identified. The accompanying IPF map, K_J versus crack length relationship, and KAM map for this region are shown in (b)-(d), respectively
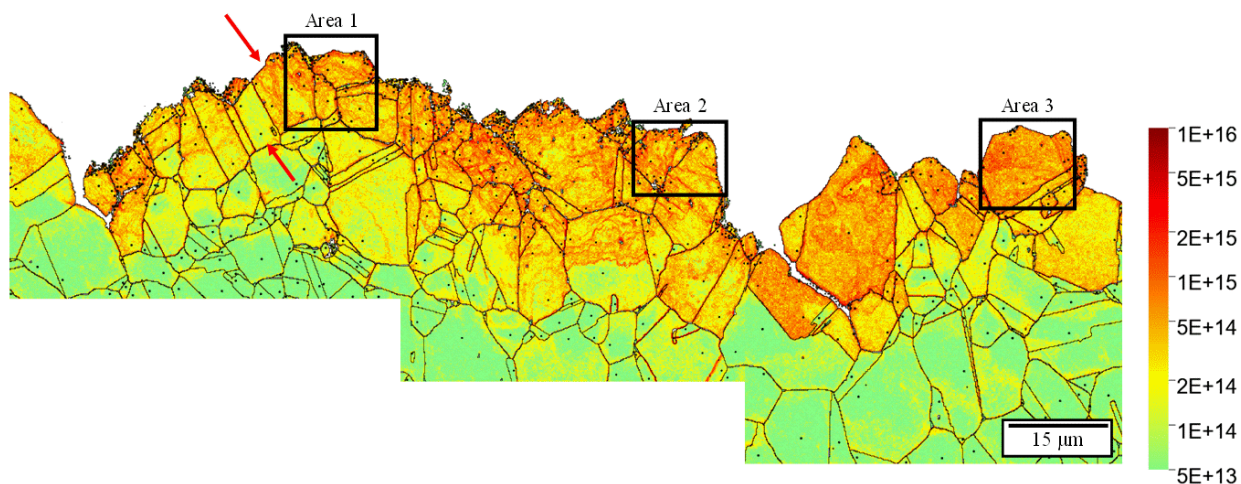
Figure 29 – GND density map corresponding to the near-crack path region of the ion milled cross-section presented in Figure 28. The black boxes correspond to the areas characterized using HR-EBSD at higher magnification in Figure 30, while the red arrows indicate adjacent grains that exhibit differences in dislocation patterning. Note that the scale bar is logarithmic and units are in m^{-2}.

To further assess this grain-to-grain variation in dislocation distribution, three grains (denoted as Area 1, 2, and 3 in Figures 28 and 29, respectively) were designated for additional evaluation using additional HR-EBSD (with a reduction in step size from 150 to 75 nm) and FIB/TEM. These grains were selected due to their nominally low-index orientation and optimal location for conducting FIB extraction. The average grain orientation, indicated on the IPF legend shown in Figure 30d, was [114], [414], and [212] for Areas 1, 2, and 3, respectively. The GND maps calculated from these additional HR-EBSD scans are also shown in Figure 30; a comparison with the GND density distributions observed in Figure 29 for the selected grains suggests nominally similar results were obtained despite the difference in step size.[47] Each grain exhibits a slightly different distribution of GND density, with Area 1 containing thick "bands" of elevated GND density (two examples indicated by the black arrows in Figure 30a), while Area 2 appears to be divided into a "cell"-like arrangement with regions of low GND density surrounded by boundaries of high GND density (example indicated by black arrow in Figure 30b). Conversely, the upper half of the grain of interest in Area 3 contains a nominally uniform GND density, though local regions of increased or decreased density can still be identified, as noted by the black arrows in Figure 30c.

In order to evaluate the efficacy of the GND density mapping strategy as a complementary technique to FIB/STEM approaches, the dislocation patterning observed using each technique must be compared. As such, TEM specimens were excised from each area of interest in Figure 30 for comparison to the results shown in Figure 29. Care was taken to keep the plane of the TEM specimen within 100-150 nm of the cross-section surface, thereby ensuring that the same nominal region was evaluated by both HR-EBSD and STEM. BF-STEM micrograph montages of the FIB specimen excised from each area are shown in Figure 31, with the area depicted in the BF-STEM image nominally corresponding to the dashed boxes in Figure 30. Two observations are readily apparent from a comparison of Figures 30 and 31. First, fine dislocation patterning features, such as the planar bands oriented along {111} planes noted in Figure 30a and 30c (white arrows), were not observed in the corresponding GND density maps. However, consistent with expectations for examination of different grain orientations,[51,52] differences in the fine dislocation patterning were noted amongst the three regions. Specifically, while evidence of planar slip was observed in both Figure 31a and 31c, slip along multiple {111} planes was observed in that Figure 31c (white

arrow), while only one set of {111} bands was observed in the Figure 31a (white arrow). Conversely, evidence of planar slip was limited in Area 2 (some planar bands can be seen near the bottom of Figure 31b), with a more cellular structure observed as noted by white arrow in Figure 31b. Second, while these fine features were not distinguished by GND maps generated using HR-EBSD, a qualitative evaluation of the regions containing "high" and "low" dislocation density suggests reasonable agreement between the GND maps and BF-STEM images. For example, the "bands" indicated by the black arrows in Figure 30a correspond well with the regions of high contrast observed in Figure 31a (indicated by the red arrows), while the regions of "increased" and "reduced" dislocation density noted in Figure 30c (black arrows) are well-aligned with the noted regions of "high" and "low" dislocation density in Figure 31c (red arrows). Lastly, though broad agreement was not generally observed in Area 2, a region of reduced dislocation density was observed in Figure 31b in the same vicinity (shown by the red arrow) as the low GND density region indicated by the black arrow in Figure 30b. It is speculated that this poor agreement is due to thickness variations in the TEM specimen that were induced during FIB milling by the jagged fracture surface.
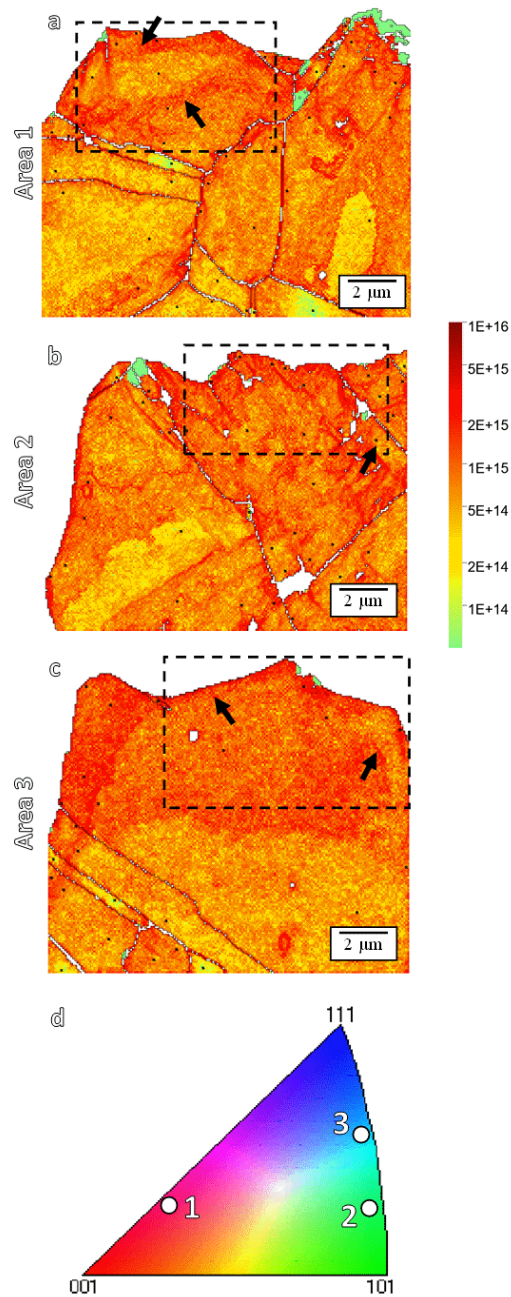
Figure 30 – GND density maps for (a) Area 1, (b) Area 2, and (c) Area 3 denoted in Figures 2 and 3, along with (d) an inverse pole figure documenting the grain orientation of each area. The dashed black boxes in (a)-(c) correspond to the nominal location of TEM micrographs shown in Figure 5, with the black arrows highlighting features observed by both TEM and HR-EBSD. Note that (1) these GND maps have been mirrored across the vertical axis relative to Figure 3 so as to align with the STEM images in Figure 5 and (2) the green regions in (a)-(c) represent areas that could not be solved due to Kikuchi pattern quality and therefore are assigned the minimum GND density.
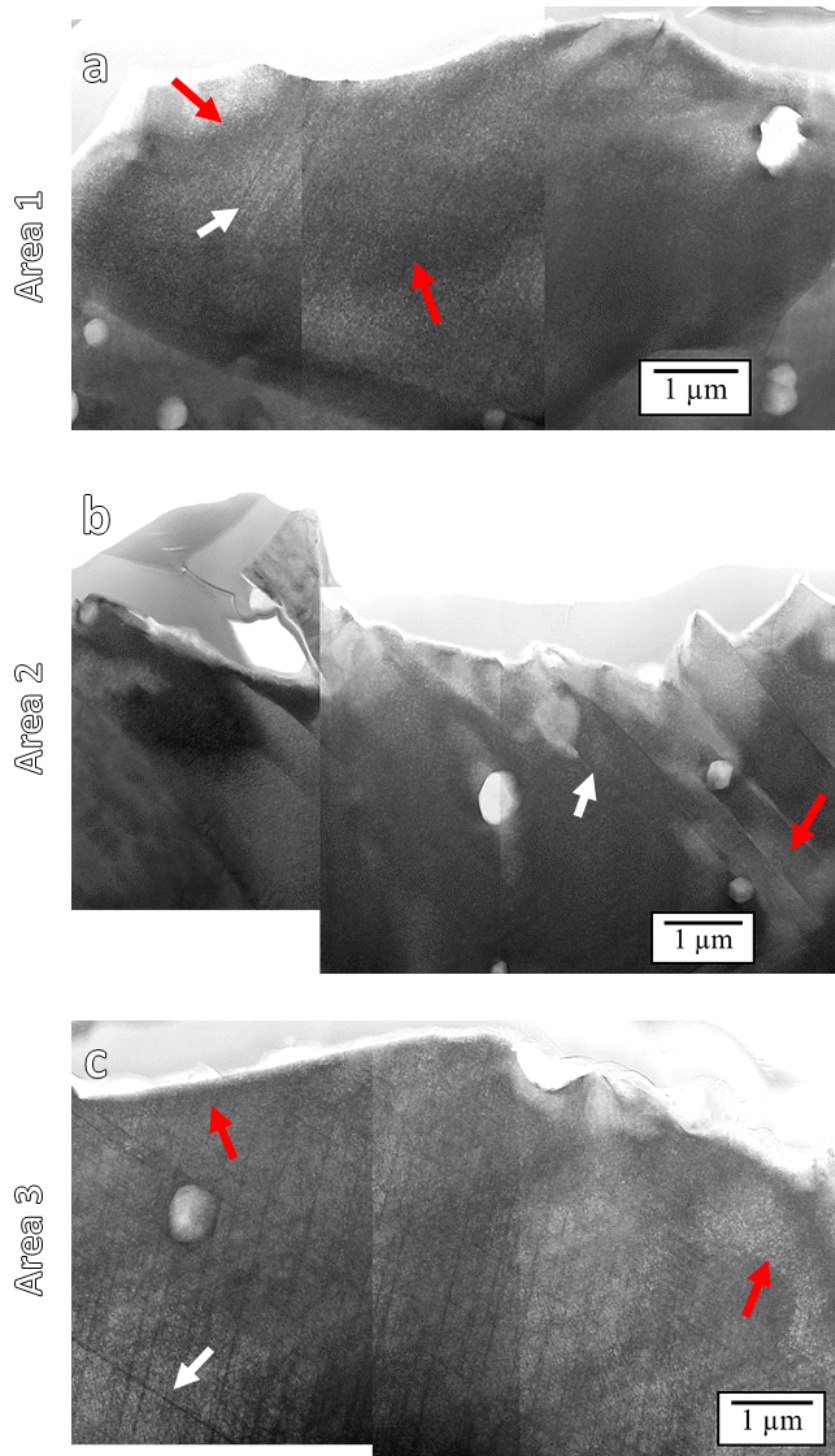
Figure 31 – BF-STEM micrographs of (a) Area 1, (b) Area 2, and (c) Area 3. The red arrows in each figure correspond to the features indicated by the black arrows in the GND maps presented in Figure 30.

Dislocation patterning features of interest in each area are indicated by the white arrows, such as planar bands in (a) and (c) as well as an apparent cell morphology in (b).

5.4. Discussion

The critical observations from this study are as follows: (1) increases in the calculated KAM and GND density from S-EBSD and HR-EBSD are strongly localized to the crack path, (2) distinct variations in dislocation patterning were observed among three separate grains when examined by both HR-EBSD and TEM, (3) the GND density distribution determined *via* HR-EBSD was qualitatively similar to the distribution observed using BF-STEM for each grain, but (4) the GND density maps could not resolve the fine-scale features observed *via* BF-STEM.

The localization in deformation proximate to the crack path shown in Figures 28 and 29 is consistent with the results of prior literature comparing the effect of gaseous hydrogen exposure on the fatigue crack growth behavior of iron versus the response in laboratory air.[13,53,54] Conducting similar comparative experiments in laboratory air for HEAC is challenging due to the toughness of Monel K-500 (200-300 MPa√m)[37] being significantly increased relative to the threshold stress intensity for HEAC (10-15 MPa√m).[36] As such, while the current study cannot inform the relative role of H on the scale or intensity of localized deformation, the present results do suggest that HEAC occurs by local damage processes, as the pertinent deformation is essentially on the scale of the grain size. It follows then that the local microstructure plays a critical role in determining the resistance to HEAC, suggesting that a spectrum of failure criteria exists with a complicated dependence on the local microstructure and mechanical driving force (*e.g.* applied stress intensity). Stated otherwise, the combination of contributing factors (*e.g.* remote stress, local stresses induced by slip, grain boundary character, constraint from neighboring grains, degradation in cohesive strength by hydrogen, etc.) that result in failure along one grain boundary may not cause failure in another. Given the number of potential contributors to H-assisted failure, it is critical that the highly localized TEM/FIB approach be augmented to account for possible variations induced by microstructure and mechanical driving force.

Though HR-EBSD is unable to resolve fine dislocation patterning features (*e.g.* dislocation cells or planar bands), the presented data demonstrates that the technique can identify regions of nominally "high" and "low" dislocation density over regions spanning 100s-10000s μm^2, while simultaneously collecting grain orientation, size, and neighborhood data. The qualitative

agreement between the calculated GND density distribution and the observed dislocation distribution imaged using BF-STEM regarding broad regions of elevated or reduced dislocation density suggests that HR-EBSD is a potential pathway for conducting complementary assessments of the deformation and microstructure at the length scales pertinent to HEAC. This general agreement between the two techniques is consistent with recent efforts comparing dislocation characteristics measured *via* TEM[28] and ECCI[29] with those calculated using HR-EBSD. Additionally, the current results are also qualitatively consistent with strain gradient plasticity (SGP) predictions of the crack-tip stress field. Specifically, SGP predicts a strong enhancement in the GND density (and hydrostatic stress) within 1-5 µm of the crack tip, as shown by Martinez-Paneda *et al.* for Monel K-500 loaded to K levels similar to those observed herein.[55] While these theories predict a continuous increase in GND density as the crack is approached,[55] which is counter to the discontinuous GND density distributions shown in Figure 29, the magnitude of the predicted GND density is qualitatively similar ($\sim 10^{-16}$ m^{-2} at 1 µm from the crack tip) to the values observed proximate to the crack path in Figure 30.

Taken together, these data and prior reports provide support for the use of HR-EBSD in assessing the role of deformation on HEAC, while simultaneously underscoring the need to develop clear linkages between microstructural elements and material resistance to HEAC. As the analysis in the current study was predominantly qualitative to demonstrate the utility of this multiscale approach, future efforts will seek to develop quantitative relationships between GND density metrics and the local conditions for failure. For example, it is well-established that an increased propensity for planar slip generally increases the susceptibility to stress corrosion cracking (such as HEAC).[56,57] Recent studies also indicate that H modifies the interaction between dislocation and strengthening precipitates,[58] which could induce local variations in slip morphologies that are not representative of the bulk morphology. The quantitative comparison of GND distributions proximate to the crack path for precipitation-hardened alloys undergoing bulk wavy and planar slip may provide insights into these dependences.

5.5. Conclusions

The efficacy of a multiscale characterization approach leveraging S-EBSD, HR-EBSD, and FIB/BF-STEM to understand the microstructural factors governing the local failure criteria for HEAC in Monel K-500 was assessed. In particular, the variation in local plastic deformation across

three different locations experiencing nominally the same mechanical driving force was quantified by KAM and GND metrics obtained *via* EBSD and HR-EBSD, while the dislocation structure was qualitatively evaluated *via* BF-STEM. Based on the results of this analysis, the following conclusions can be made:

1. Assessment of KAM maps obtained *via* S-EBSD demonstrate that deformation induced during HEAC is highly localized to the crack path, suggesting that the evaluation of local damage processes is critical to developing mechanistic understanding of HEAC.

2. A qualitative comparison of GND maps and BF-STEM micrographs obtained from the same location revealed an inability to resolve the fine-scale dislocation patterning observed in the TEM. However, a qualitative similarity in dislocation density was observed between the two techniques.

3. Comparison of BF-STEM micrographs taken from three separate grains of different orientation along the crack path, which all experienced the same nominal mechanical driving force, confirms the effect of grain orientation on observed dislocation patterning.

5.6. Acknowledgements

5.7. References

1. Keller, C., Hug, E., Retoux, R. & Feaugas, X. Mechanics of Materials TEM study of dislocation patterns in near-surface and core regions of deformed nickel polycrystals with few grains across the cross section. *Mech. Mater.* **42**, 44–54 (2010).

2. Bay, B., Hansen, N. & Kuhlmann-Wilsdorf, D. Microstructural evolution in rolled aluminum. *Mater. Sci. Eng. A* **158**, 139–146 (1992).

3. Harris, Z. D. *et al.* Elucidating the contribution of mobile hydrogen-deformation interactions to hydrogen-induced intergranular cracking in polycrystalline nickel. *Acta Mater.* **158**, 180–192 (2018).

4. Mcinteerf, W. A., Thompson, A. W. & Bernstein, I. M. THE EFFECT OF HYDROGEN ON THE SLIP CHARACTER OF NICKEL. *Acta Metall.* **28**, 887–894 (1980).

5.   Robertson, I. M. & Birnbaum, H. K. Effect of Hydrogen on the Dislocation Structure of Deformed Nickel. *Scr. Metall.* **18**, 269–274 (1984).

6.   Martin, M. L., Somerday, B. P., Ritchie, R. O., Sofronis, P. & Robertson, I. M. Hydrogen-induced intergranular failure in nickel revisited. *Acta Mater.* **60**, 2739–2745 (2012).

7.   Bertsch, K. M., Wang, S., Nagao, A. & Robertson, I. M. Hydrogen-induced compatibility constraints across grain boundaries drive intergranular failure of Ni. *Mater. Sci. Eng. A* **760**, 58–67 (2019).

8.   Wang, S., Nagao, A., Edalati, K., Horita, Z. & Robertson, I. M. Acta Materialia In fl uence of hydrogen on dislocation self-organization in Ni. **135**, 96–102 (2017).

9.   Martin, M. L., Sofronis, P., Robertson, I. M., Awane, T. & Murakami, Y. A microstructural based understanding of hydrogen-enhanced fatigue of stainless steels. *Int. J. Fatigue* **57**, 28–36 (2013).

10.   Nagao, A., Smith, C. D., Dadfarnia, M. & Sofronis, P. The role of hydrogen in hydrogen embrittlement fracture of lath martensitic steel. *Acta Mater.* **60**, 5182–5189 (2012).

11.   Kocks, U. F. & Mecking, H. Physics and phenomenology of strain hardening: The FCC case. *Prog. Mater. Sci.* **48**, 171–273 (2003).

12.   Anderson, T. *Fracture Mechanics: Fundamentals and Applications*. (Taylor & Francis Group, 2005).

13.   Ogawa, Y., Birenis, D., Matsunaga, H., Thøgersen, A. & Prytz, Ø. Scripta Materialia Multi-scale observation of hydrogen-induced , localized plastic deformation in fatigue-crack propagation in a pure iron. *Scr. Mater.* **140**, 13–17 (2017).

14.   Birenis, D., Ogawa, Y., Matsunaga, H. & Takakuwa, O. Acta Materialia Interpretation of hydrogen-assisted fatigue crack propagation in BCC iron based on dislocation structure evolution around the crack wake. *Acta Mater.* **156**, 245–253 (2018).

15.   Ogawa, Y., Birenis, D., Matsunaga, H. & Takakuwa, O. Materials Science & Engineering A The role of intergranular fracture on hydrogen-assisted fatigue crack propagation in pure iron at a low stress intensity range. *Mater. Sci. Eng. A* **733**, 316–328 (2018).

16.   Merson, E. D., Myagkikh, P. N., Poluyanov, V. A., Merson, D. L. & Vinogradov, A. Quasi-cleavage hydrogen-assisted cracking path investigation by fractographic and side surface observations. *Eng. Fract. Mech.* **214**, 177–193 (2019).

17.   Chen, Y. Z. *et al.* Increase in dislocation density in cold-deformed Pd using H as a temporary alloying addition. *Scr. Mater.* **68**, 743–746 (2013).

18.   Wan, D., Alvaro, A., Olden, V. & Barnoush, A. Hydrogen-enhanced fatigue crack growth behaviors in a ferritic Fe-3wt% Si steel studied by fractography and dislocation structure analysis. *Int. J. Hydrogen Energy* **44**, 5030–5042 (2019).

19.   Birenis, D. *et al.* Hydrogen-assisted crack propagation in α-iron during elasto-plastic

fracture toughness tests. *Mater. Sci. Eng. A* **756**, 396–404 (2019).

20. Ogawa, Y. *et al.* Pronounced transition of crack initiation and propagation modes in the hydrogen-related failure of a Ni-based superalloy 718 under internal and external hydrogen conditions. *Corros. Sci.* **161**, 108186 (2019).

21. Ogawa, Y., Okazaki, S., Takakuwa, O. & Matsunaga, H. The roles of internal and external hydrogen in the deformation and fracture processes at the fatigue crack tip zone of metastable austenitic stainless steels. *Scr. Mater.* **157**, 95–99 (2018).

22. Connolly, M. *et al.* In situ high energy X-ray diffraction measurement of strain and dislocation density ahead of crack tips grown in hydrogen. *Acta Mater.* **180**, 272–286 (2019).

23. Britton, T. B. & Hickey, J. L. R. Understanding deformation with high angular resolution electron backscatter diffraction (HR-EBSD). *IOP Conf. Ser. Mater. Sci. Eng.* **304**, (2018).

24. Britton, T. Ben, Jiang, J., Karamched, P. S. & Wilkinson, A. J. Probing deformation and revealing microstructural mechanisms with cross-correlation-based, high-resolution electron backscatter diffraction. *Jom* **65**, 1245–1253 (2013).

25. Wilkinson, A. J., Meaden, G. & Dingley, D. J. High-resolution elastic strain measurement from electron backscatter diffraction patterns : New levels of sensitivity. *Ultramicroscopy* **106**, 307–313 (2006).

26. Jiang, J., Britton, T. B. & Wilkinson, A. J. Measurement of geometrically necessary dislocation density with high resolution electron backscatter diffraction : Effects of detector binning and step size. *Ultramicroscopy* **125**, 1–9 (2013).

27. Ruggles, T. J., Rampton, T. M., Khosravani, A. & Fullwood, D. T. Ultramicroscopy The effect of length scale on the determination of geometrically necessary dislocations via EBSD continuum dislocation microscopy. *Ultramicroscopy* **164**, 1–10 (2016).

28. Yoo, Y. S. J., Lim, H., Emery, J. & Kacher, J. Relating microstructure to defect behavior in AA6061 using a combined computational and multiscale electron microscopy approach. *Acta Mater.* **174**, 81–91 (2019).

29. Dunlap, B. E., Ruggles, T. J., Fullwood, D. T., Jackson, B. & Crimp, M. A. Comparison of dislocation characterization by electron channeling contrast imaging and cross-correlation electron backscattered diffraction. *Ultramicroscopy* **184**, 125–133 (2018).

30. Jiang, J., Britton, T. B. & Wilkinson, A. J. ScienceDirect Evolution of dislocation density distributions in copper during tensile deformation. *Acta Mater.* **61**, 7227–7239 (2013).

31. Britton, T. B. & Wilkinson, A. J. Stress fields and geometrically necessary dislocation density distributions near the head of a blocked slip band. *Acta Mater.* **60**, 5773–5782 (2012).

32. Karamched, P. S. & Wilkinson, A. J. High resolution electron back-scatter diffraction analysis of thermally and mechanically induced strains near carbide inclusions in a

superalloy. *Acta Mater.* **59**, 263–272 (2011).

33. Littlewood, P. D. & Wilkinson, A. J. Geometrically necessary dislocation density distributions in cyclically deformed Ti – 6Al – 4V. *Acta Mater.* **60**, 5516–5525 (2012).

34. Jiang, J. *et al.* Acta Materialia Microstructurally sensitive crack nucleation around inclusions in powder metallurgy nickel-based superalloys. *Acta Mater.* **117**, 333–344 (2016).

35. Harris, Z. D. *et al.* The Effect of Microstructural Variation on the Hydrogen Environment-Assisted Cracking of Monel K-500. *Metall. Mater. Trans. A* **47**, 3488–3510 (2016).

36. Harris, Z. D. & Burns, J. T. The effect of isothermal heat treatment on hydrogen environment-assisted cracking susceptibility in Monel K-500. *Mater. Sci. Eng. A* **764**, 138249 (2019).

37. Gangloff, R. P., Ha, H. M., Burns, J. T. & Scully, J. R. Measurement and Modeling of Hydrogen Environment-Assisted Cracking in Monel K-500. *Metall. Mater. Trans. A* **45**, 3814–3834 (2014).

38. Burns, J. T., Harris, Z. D., Dolph, J. D. & Gangloff, R. P. Measurement and Modeling of Hydrogen Environment Assisted Cracking in a Ni-Cu-Al-Ti Superalloy. *Metall. Mater. Trans. A* **47**, 990–997 (2016).

39. Troconis, B. C. R., Harris, Z. D., Ha, H., Burns, J. T. & Scully, J. R. The effect of heat-to-heat variations in metallurgy and hydrogen-metal interactions on the hydrogen embrittlement of Monel K-500. *Mater. Sci. Eng. A* **703**, 533–550 (2017).

40. Martínez-Pañeda, E., Harris, Z. D., Fuentes-Alonso, S., Scully, J. R. & Burns, J. T. On the suitability of slow strain rate tensile testing for assessing hydrogen embrittlement susceptibility. *Corros. Sci.* **163**, 108291 (2020).

41. Donald, J. K. & Ruschau, J. Direct current potential difference fatigue crack measurement techniques. in *Fatigue crack measurement: techniques and applications* (eds. Marsh, K. J., Smith, R. A. & Ritchie, R. O.) 11–37 (EMAS, 1991).

42. Johnson, H. H. Calibrating the Electric Potential Method for Studying Slow Crack Growth. *Mater. Res. Stand.* **5**, 442–445 (1965).

43. Schwalbe, K.-H. & Hellmann, D. Application of the Electrical Potential Method to Crack Length Measurements Using Johnson's Formula. *J. Test. Eval.* **9**, 218–221 (1981).

44. Popernack, A. S. Loading Rate Effects on Hydrogen-Enhanced Cracking Behavior of Ni- and Co-Based Superalloys for Marine Applications. (University of Virginia, 2017).

45. Kumar, V., German, M. D. & Shih, C. F. *An Engineering Approach for Elastic-Plastic Fracture Analysis*. (Electric Power Research Institute, 1981).

46. Anderson, T. L. *Fracture Mechanics: Fundamentals and Applications*. (Taylor & Francis, 2005).

47. Ruggles, T. J., Rampton, T. M., Khosravani, A. & Fullwood, D. T. The effect of length scale on the determination of geometrically necessary dislocations via EBSD continuum dislocation microscopy. *Ultramicroscopy* **164**, 1–10 (2016).

48. Thompson, A. W., Harris, Z. D. & Burns, J. T. Examination of focused ion beam-induced damage during platinum deposition in the near-surface region of an aerospace aluminum alloy. *Micron* **118**, 43–49 (2019).

49. Fultz, B. & Howe, J. M. *Transmission Electron Microscopy and Diffractometry of Materials, 3rd Edition*. (2008). doi:10.1017/CBO9781107415324.004

50. Brewer, L. N., Field, D. P. & Merriman, C. C. Mapping and Assessing Plastic Deformation Using EBSD. in *Electron Backscatter Diffraction in Materials Science* (eds. Schwartz, A. J., Kumar, M., Adams, B. L. & Field, D. P.) 251–262 (Springer, 2009).

51. Wert, J. A., Huang, X., Winther, G., Pantleon, W. & Poulsen, H. F. Revealing deformation microstructures. *Mater. Today* **10**, 24–32 (2007).

52. Hansen, N., Huang, X. & Winther, G. Grain orientation , deformation microstructure and flow stress. **494**, 61–67 (2008).

53. Birenis, D. *et al.* Interpretation of hydrogen-assisted fatigue crack propagation in BCC iron based on dislocation structure evolution around the crack wake. *Acta Mater.* **156**, 245–253 (2018).

54. Ogawa, Y. *et al.* The role of intergranular fracture on hydrogen-assisted fatigue crack propagation in pure iron at a low stress intensity range. *Mater. Sci. Eng. A* **733**, 316–328 (2018).

55. Niordson, C. F., Gangloff, R. P. & Martínez-pa, E. Acta Materialia Strain gradient plasticity-based modeling of hydrogen environment assisted cracking. **117**, (2016).

56. Swann, P. R. Dislocation Substructure vs Transgranular Stress Corrosion Susceptibility Of Single Phase Alloys. *Corrosion* **19**, 102t-114t (1963).

57. Thompson, A. W. & Bernstein, I. M. The Role of Metallurgical Variables in Hydrogen-Assisted Environmental Fracture. in *Advances in Corrosion Science and Technology* (eds. Fontana, M. G. & Staehle, R. W.) 53–175 (Springer-Verlag, 1980). doi:10.1007/978-1-4615-9065-1_2

58. Harris, Z. D., Bhattacharyya, J. J., Ronevich, J. A., Agnew, S. R. & Burns, J. T. The combined effects of hydrogen and aging condition on the deformation and fracture behavior of a precipitation-hardened nickel-base superalloy. *Acta Materialia* (2020). /doi:10.1016/j.actamat.2020.01.033

Chapter 6 – Elucidating the mechanisms governing fatigue behavior in AA7075-T651 exposed to high altitude environments

6.1. Overview

It is well known that the fatigue crack growth behavior of aluminum is affected by the loading environment, particularly for the near-threshold region and Paris regime of fatigue. Studies have demonstrated fatigue testing of aluminum alloys under vacuum or dry air (extremely low amounts of water vapor), result in significantly slower crack growth rates than the growth rates in laboratory air, moist or corrosive environments.[1–18] Various mechanisms such as adsorption, chemisorption, hydrogen embrittlement and rewelding of the fractured surfaces due to the degree of friction have all been proposed as the cause for the observed changes in fatigue growth behavior.[6,12,13,19] It is generally agreed the results observed from fatigue cracking of aluminum alloys in a moist (non-negligible water) or corrosive environment are most consistent with a hydrogen embrittlement mechanism for fatigue.[3–10,20,21] The hydrogen embrittlement process starts with the mass transport of water vapor to the crack tip, where it is postulated that the reaction of water vapor with the fresh aluminum surfaces at the crack tip produce atomic hydrogen enabling the hydrogen-assisted cracking of aluminum alloys.[5] This reaction yields the production of hydrogen gas, but an intermediate reaction step is needed for the formation of atomic H with can either be adsorbed by the material or can recombine forming H_2 gas.[22] Additionally, the water reduction at the oxide-aluminum interface is a direct path for the formation of atomic hydrogen where the atomic hydrogen can be adsorbed into the aluminum or recombine to form H_2 gas.[22] The atomic hydrogen that is adsorbed into the aluminum alloy can diffuse between interstitial lattice sites, but can also get trapped in other lower potential energy sites such as solute atom clusters, free surfaces, sites between the first few atomic layers beneath the surface, mono-vacancies and vacancy clusters, dislocation cores, strain fields, grain boundaries, precipitate/matrix interfaces, strain fields around a precipitate, inclusion/matrix interfaces, voids, and internal cracks.[23] Typically this hydrogen will diffuse and concentrate ahead of notches and cracks due to the hydrostatic stresses that will cause an expansion of the crystal lattice.[23] Exactly what the mechanisms are for hydrogen embrittlement in aluminum alloys are still debated as a number of mechanisms have been proposed, but identification of the exact mechanism is beyond the scope of this study.

Commonly, the severity of the water vapor in the environment is defined with the exposure parameter, P_{H2O}/f, which quantifies the product of the partial pressure of water vapor and the time available for the water vapor to react with fresh surface created by the fatigue cracking process.[5,9] High altitude environment have two main components that make them distinguishable from other environments; (1) lower water vapor and (2) a significant decrease in temperature.[24] Individually, the significant differences in partial pressure of water is important as studies have shown fatigue testing on aluminum alloys in a vacuum, dry air or extremely low humidity environments generally result in significantly slower fatigue crack growth rates when compared to those tested in moist or high humidity environments.[1,2,5,11–13,15–17,25] The lower levels of water vapor pressure in the bulk environment is considered to correlate with lower amounts of hydrogen generation and uptake at the crack tip, thus limiting the effects of the hydrogen embrittlement process.[5,6,8,9,20,21] Studies focused on the effect of low temperature on fatigue behavior of 7xxx series aluminum alloys (or equivalent) generally display a decrease in crack growth rates or an increase in fatigue life when compared to ambient temperature experiments.[25–35] Particularly, the work by Cox et al. and Magda observed a change in the fracture mechanism from a ductile type fracture to a quasi-cleavage type occurring at temperatures below -28°C.[27,29] A study of the effect of temperature on dislocation structure development during fatigue using copper suggested a decrease in temperature affects the dislocation structure of f.c.c. materials with observations indicating a possible reduction of cross-slip.[36] Another study fatigued polycrystalline aluminum near room temperature (298K) and at 77K and observed via TEM the dislocation substructure, which had a large cellular structure with high dislocation density within the cell walls at 298K, but in contrast observed a homogeneous distribution of dislocation tangles at 77K suggesting a limitation in deformation structure development due to temperature.[37]

When the effects of both low partial pressure of water vapor and low temperature are coupled a reduction in the fatigue crack growth rate in aluminum alloys is observed when compared to experiments completed with the same P_{H2O}/f at room temperature.[38,39] These observed changes have been postulated to be due to the low temperatures impacting the kinetics of the surface reaction, hydrogen uptake, diffusion rate of hydrogen, nature of the local dislocation structure evolution, and/or the hydrogen-dislocation interaction.[37,38,40] However, more study is needed to develop a mechanistic understanding of the fatigue behavior.

113

The objective of this study is to develop a further understanding of the fatigue behavior which is responsible for the observed reduction in fatigue crack growth rates of AA7075-T651 at low temperatures and low water vapor pressures commonly associated with high altitude environments. Specifically, the efforts of this study will be two-fold; 1) Constant ΔK experiments at a low temperature to determine if there is any frequency dependent fatigue behavior that exists in the frequency range of 1 − 20 Hz. If there is no frequency dependence, then frequency can be used as a critical variable in a set of constant ΔK and P_{H2O}/f at low temperature to determine if slower diffusion rates of hydrogen are responsible for the observed differences in crack growth rates. 2) Decouple potential impacts on the fatigue behavior due to exposure to a high altitude environments by implementing the multiscale characterization method outlined in Chapter 4 to examine underlying damage structure proximate to the crack wake surface. First, by targeted fatigue crack propagation experiments using a decreasing K-shed protocol with different temperatures in UHV environments to isolate the effects of temperature. Second, by more targeted fatigue crack propagation experiments using a decreasing K-shed protocol with different temperatures, but a constant P_{H2O}/f environment to 1) isolate the impact of hydrogen by comparison with UHV sample and 2) the temperature dependent hydrogen effects on fatigue. The implications and results of these findings on the mechanisms controlling the observed behavior is discussed and interpreted in the context of fatigue fracture in high altitude environments.

6.2. Experimental Methods

6.2.1 Materials

All experiments were conducted on AA7075-T651 procured in the form of a 50.8-mm thick plate. This material heat was previously utilized in an interdisciplinary multiscale airframe fatigue prognosis study to simulate the alloy composition typical of AA7075 used in older aircraft [41]. Specifically, while this alloy meets the current elemental specification for AA7075 [42], it contains an elevated iron and silicon content relative to what is typically observed in modern AA7075 heats. Mechanical properties and the elemental composition for the tested material heat are listed in Tables 3 and 1, respectively in a previous chapter; a more detailed microstructural analysis is presented elsewhere [43,44]. Compact tension [C(T)] specimens with a width (W) of 50.8 ± 0.51 mm were extracted from the plate in the L-T orientation (loading axis parallel to the rolling direction of the plate, crack growth occurring in the transverse direction), such that the C(T) specimen mid-

thickness was located at a depth of ≈8.5 mm from the plate surface (*i.e.*, S/6 location, where S is the plate thickness). The specimen thickness (B) was 7.62 mm ± 0.51 mm with a machined starter notch depth (a_0) of 10.7 ± 0.51 mm ahead of the load line.

6.2.2. Fatigue crack growth experiments (Constant ΔK protocol)

Fatigue crack growth experiments were performed using a constant stress intensity factor range (ΔK) protocol with the crack length actively calculated throughout each experiment *via* the specimen compliance determined from the crack mouth opening displacement measured by an attached clip gage. All specimens were fatigue pre-cracked in laboratory air using a constant amplitude loading protocol with a stress ratio (R) of 0.1 and frequency (*f*) of 5 Hz, such that K_{MAX} value reached 10 MPa√m after 1 mm of crack propagation. For experiments conducted below 23ºC, as the specimen neared the targeted test temperature, a constant amplitude loading protocol ($P_{max} = 1$ kN, R = 0.5) was performed at 20 Hz to allow the temperature to stabilize while the specimen was being actively cycled. Once the temperature was fully stabilized under active loading, the modulus of elasticity used for the compliance-based crack length measurements was adjusted to compensate for temperature-induced modifications. For testing executed at 23ºC, the modulus of elasticity was not adjusted from the value established prior to the fatigue pre-cracking in laboratory air.

Three separate fatigue experiments were conducted, one completed in room temperature (Specimen 1) and two completed with the specimen cooled to -30°C (Specimen 2 and 3). Specimen 1 had two segments conducted in an UHV environment at a constant ΔK = 6 MPa√m and a R = 0.5 and a *f* = 1 and 20 Hz with a target final crack length of 2 mm for the 1 Hz segment and 3 mm for the 20 Hz segment. Specimen 2 had a series of four fatigue segments run in a 0.027 Pa·s environment with a constant ΔK = 6 MPa√m and a R = 0.5 and multiple *f* = 5, 10, 15, and 20 Hz. The final target crack length was 2 mm for the 5 Hz segment and 3 mm for the 10, 15 and 20 Hz segments. Specimen 3 had a series of four fatigue segments, the first two in an UHV environment at a constant ΔK = 6 MPa√m and a R = 0.5 and a *f* = 1 and 20 Hz and the final two segments run in a 0.027 Pa·s environment with a constant ΔK = 6 MPa√m and a R = 0.5 and a *f* = 1 and 20 Hz. The final target crack length was again 2 mm for the 1 Hz segments and 3 mm for the 20 Hz segments. Selection of environmental and driving force parameters were guided by the previous work done by Burns et al.[5] The combination of parameters selected had to provide an environment

that would impact the fatigue crack growth rate by transport of water vapor from the bulk environment to the crack front, while avoiding the production of ice on the crack mouth surface. These considerations along with equipment limitations provided a P_{H2O}/f range of 2.0E-2 to 1.0E-1 Pa·s in turn limiting the ΔK range to 5.6 - 7 MPa√m, thus the selection of of 6 MPa√m and a P_{H2O}/f = 0.027 Pa·s was appropriate.[5] Since segments were run at a different frequencies, experiments utilizing the 0.027 Pa·s environment had the P_{H2O} adjusted prior to the segment starting to maintain a constant P_{H2O}/f for all segments. Crack growth rates were calculated using the 7-point (n = 3) incremental polynomial method described in ASTM E647[45] and closure was monitored using the adjusted compliance ratio (ACR) method outlined by the studies done by Donald et al.[46,47] Experiments were performed with a computer controlled servohydraulic machine retrofitted with an ultra-high vacuum system. The -30°C experiments were cooled using a water-cooled helium compressor attached to an expander unit containing a copper plate on the end of the coldhead. Bolted to the copper plate was copper braiding with the opposing ends of the braiding clamped onto the C(T) specimen both above and below the crack plane. A DT-670B silicon diode thermocouple was placed in contact with the C(T) specimen using aluminum tape, thereby allowing for the specimen temperature to be directly monitored throughout each experiment. With this setup, fatigue experiments could be held within ±0.5ºC of the desired temperature.

6.2.3. Fatigue crack growth experiments (K-shed protocol)

Fatigue crack growth experiments with a 0.027 Pa·s environment were performed using a decreasing ΔK protocol (ΔK-shed) conducted in accordance with ASTM Standard E647.[45] Crack length was calculated from a clip gauge, which measured the crack mouth opening displacement using unloading compliance. Post-test visual crack length measurements were always within 10% of the compliance values and visual measurements were used for data correction. The fatigue testing parameters had an R = 0.5 and f = 20 Hz with a C-value of 0.08 mm^{-1} with the ΔK-shed starting at 10 MPa√m and running to threshold. The 23°C experiment was performed with a computer controlled servohydraulic machine retrofitted with an ultra-high vacuum system with purified water was introduced through a sealed glass flask via a leak valve and the pressure was dynamically maintained by balancing the water vapor input and the vacuum turbomolecular pumping out. The water vapor pressure was monitored throughout the testing and a mass

spectrometer confirmed better than 95% (by partial pressure) H_2O purity through all tests (the impurities in the vacuum chamber were a mixture of gaseous CO_2 and N_2).

The -65°C experiment was performed using a computer controlled servohydraulic machine retrofitted with a furnace casing with low temperature insulation and a controlled solenoid valve entry point for liquid nitrogen converted to cold nitrogen gas to enter the environmental chamber. For the initial cool down, the solenoid valve operated in the fully open position until the temperature was within approximately 5 °C of the target temperature at which point the open/close rate was slowed to prevent severe over-shooting of the target temperature. Once at the target temperature, the solenoid valve would open when the chamber temperature increased above the target. The critical assumption in this experimental configuration is that the water vapor pressure at -65°C is well represented by the equilibrium water vapor pressure above ice at -65°C.[48] A Clausius-Clapeyron relationship known as the Goff-Gratch equation was used to calculate the equilibrium $P_{H2O-ICE}$ and $P_{H2O-ICE}/f$ values, which were found to be 0.54 Pa and 0.027 Pa·s respectively. This assumption is justified so long as (1) there is thin ice layer on the surface of the specimen which sets the local P_{H2O} pertinent to the cracking process at a constant regardless of the global P_{H2O} inside the chamber, and (2) the active flowing of the nitrogen gas (which has very low humidity) does not disrupt the local equilibrium at the specimen surface. Containers of water were inserted into the environmental chamber prior to decreasing the temperature to ensure an initial high humidity environment would precipitate the formation of an ice layer on the surfaces and the gas flow inlet was positioned away from the sample to avoid destabilization of the local environment.

While the water vapor pressure local to the crack is most pertinent to the environmental cracking behavior, the global water vapor pressure within the environmental testing chamber was monitored by a combined temperature and humidity meter (Viasala HMT337) placed 150–200 mm from the specimen surface. The average values measured via the humidity meter was 0.57 Pa, which corresponded well with the previously calculated value. Deviation from the average measured value would occur during the ingress of the nitrogen gas which measured at a minimum of 0.37 Pa during the test. Considerations strongly suggesting the variations were not controlling the P_{H2O} at the crack tip are an ice-layer was maintained on the sample and the gas inlet configurations precluded direct disturbance of the local specimen environment (even if disturbed

local equilibrium would be rapidly re-established), and detailed correlation between the cycle count specific bulk measurements of P_{H2O} with the applied da/dN vs. ΔK data show that the measured bulk P_{H2O} fluctuations do not correspond with observed changes in the growth rate behavior.

Fatigue crack growth experiments with a UHV (defined as a pressure less than 3×10^{-6} Pa) environment were performed using a decreasing ΔK protocol (K-shed) conducted in accordance with ASTM Standard E647.[45] Specimens were first fatigue pre-cracked in laboratory air using a constant amplitude loading protocol with a stress ratio (R) of 0.1 and frequency (*f*) of 5 Hz, such that K_{MAX} value reached 10 MPa√m after 1 mm of crack propagation. For experiments conducted below 23ºC, as the specimen neared the targeted test temperature, a constant amplitude loading protocol ($P_{max} = 1$ kN, R = 0.5) was performed at 20 Hz to allow the temperature to stabilize while the specimen was being actively cycled. Once the temperature was fully stabilized under active loading, the modulus of elasticity used for the compliance-based crack length measurements was adjusted to compensate for temperature-induced modifications. For testing executed at 23ºC, the modulus of elasticity was not adjusted from the value established prior to the fatigue pre-cracking in laboratory air. The K-shed portion of the experiment was performed with testing parameters of R = 0.5 and *f* = 20 Hz, with the ΔK programmed to decrease as a function of instantaneously measured crack length (a) according to $\Delta K = \Delta K_o e^{C(a-a_o)}$, where the initial ΔK (ΔK_o) was 10 MPa√m, the initial crack length (a_o) corresponded to the crack length recorded at the end of the pre-crack protocol, and the K-gradient (C) was -0.08 mm^{-1} all in accordance with ASTM E647.[45] Testing was stopped when either da/dN was consistently less than 1.0×10^{-7} mm/cycle or the R^2 value for a linear fit to the measured compliance was less than 0.8. Crack growth rates were calculated using the 7-point (n = 3) incremental polynomial method described in ASTM E647,[45] while closure influences were monitored via the calculation of an effective ΔK using the adjusted compliance ratio (ACR) method.[46,47]

After the completion of each experiment, the actual pre-crack and final crack length were measured using a FEI Quanta 650-FEG scanning electron microscope (SEM) to linearly correct the compliance-based crack length measurements. The compliance-based pre-crack and final crack length were generally found to be within 1% and 3%, respectively, of the post-test measured values. Both experiments were performed with a computer controlled servohydraulic machine

retrofitted with an ultra-high vacuum system. The -65°C experiment was cooled using a water-cooled helium compressor attached to an expander unit containing a copper plate on the end of the cold head. Bolted to the copper plate was copper braiding with the opposing ends of the braiding clamped onto the C(T) specimen both above and below the crack plane. A DT-670B silicon diode thermocouple was placed in contact with the C(T) specimen using aluminum tape, thereby allowing for the specimen temperature to be directly monitored throughout each experiment. With this setup, fatigue experiments could be held within ±0.5ºC of the desired temperature.

6.2.4. Characterization of fatigue crack growth experiments (K-shed protocol)

Characterization of the four K-shed fatigue experiments was guided by the work done in the Harris et al. study, which developed a novel multi-scale characterization technique for examination of near crack wake surfaces.[49] The fracture surfaces of each of the four specimens were excised from the bulk C(T) specimen using a cut off saw with performed cuts at least 3 mm from the target areas of the fracture surface to prevent the introduction of any obfuscation of deformation observed in final samples. The target areas selected were crack lengths indicated by the growth kinetics data to be at a ΔK of 6 MPa√m, which showed a strong deviation in crack behavior between the different environments and a ΔK of 9 MPa√m, which showed similar crack growth behavior regardless of the different environments. After excision of the target areas the specimens were progressively thinned to final dimensions outlined in Figure 27, with the exception of the final thickness in the Y-direction being exactly half the B_{NET} thickness of the C(T) specimen to ensure the evaluation of the sub crack wake was under plane strain conditions. The thinning was done using SiC polishing papers and diamond slurries with the final polish ending with a 1 μm diamond slurry. An argon broad-beam ion mill (Hitachi IM4000) was then utilized to expose a cross section of material at a surface condition suitable for EBSD, with the depth of the ion mill trench positioned so as to be sufficiently deep (> 3 μm) to remove any residual damage induced by the final 1 μm diamond polish.

Both standard electron backscatter diffraction (S-EBSD) and high resolution electron backscatter diffraction (HR-EBSD) were conducted using an FEI Helios G4 UC FIB/SEM equipped with an Oxford Symmetry EBSD detector. The main purpose of the "global" perspective was to identify the orientations of the exposed grains to ensure that all selected areas for further interrogation were of similar orientation, which for this study was near {100} grains. All the EBSD

utilized an accelerating voltage of 30 keV and probe current of 3.2 nA, with the S-EBSD being performed with a 750-nm step size and 2 x 2 binning of the EBSD camera pixels to provide a "global" perspective and HR-EBSD scans being conducted with a 75-nm step size and 2 x 2 binning to provide a "local" perspective. The commercial cross-correlation analysis software, CrossCourt 4, was used to generate the KAM and GND density maps from the HR-EBSD scans. Next the area of interest was excised from the specimen utilizing an FEI Helios G4 UC DB-FIB. Before the excision, to prevent damage and/or alteration of the microstructure during transmission electron microscope (TEM) sample preparation, a two-step Pt deposition outlined by the Thompson et al. study utilizing both the E-beam and I-beam was deposited onto the surface of the target area for protection.[50] After this Pt protection layer was deposited, the TEM samples were completed using the standard FIB lift-out practice using an FEI EasyLift micromanipulator and attached to a Cu TEM half- grid. Completed samples were thinned to around 100 nm in thickness and examined using an FEI titan TEM equipped with a double-tilt holder and operated at 300 KeV with the specimen centers aligned to the <100> zone axis. Additionally, the precession electron diffraction (PED) was performed with an FEI Talos F200X TEM utilizing a NanoMEGAS ASTAR equipment and software with a step size of 5 nm.

6.3. Results

6.3.1. Fatigue crack growth experiments (Constant ΔK protocol)

The data collected for the constant ΔK protocol experiments was collected and the crack length was plotted as a function of the number of cycles. A linear regression was performed yielding a R^2 value of .98 or higher for all fits was achieved. The slope of each fit line was reported and used as the reported crack growth rate (da/dN) for the respective fatigue segment shown in Table 4 and plotted in Figures 32 and 33.

Table 4 - A table listing the crack growth rates for each of the fatigue segments run with a constant 1ΔK (6 MPa√m) protocol.

Specimen ID	Environment (Pa·s)	Frequency (Hz)	Crack Growth Rate (mm/cycle)
Specimen 1	23°C UHV	1	2.08E-5
		20	1.46E-5
Specimen 2	-30°C 0.027	5	2.33E-7
		10	2.71E-7
		15	3.95E-7
		20	5.64E-7
Specimen 3	-30°C UHV	1	1.06E-6
		20	1.87E-6
	-30°C 0.027	1	1.59E-7
		20	5.55E-7
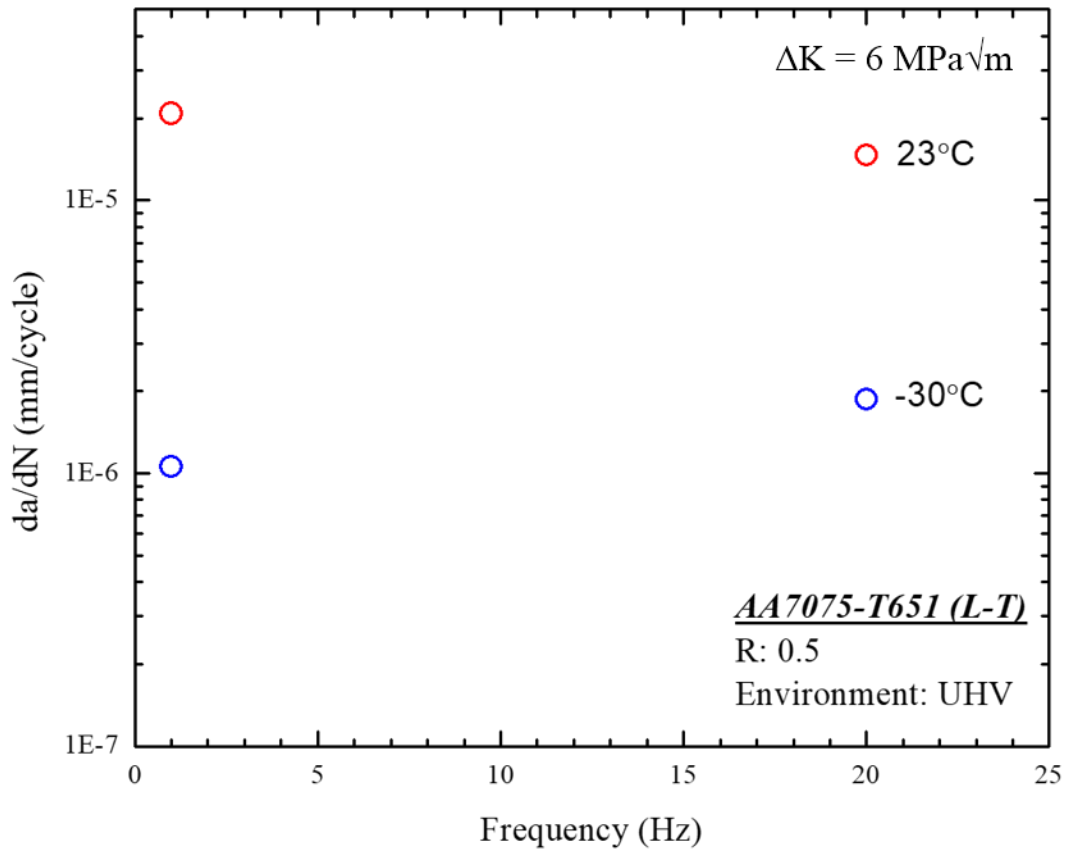
Figure 32 – A plot of the fatigue segments completed with a constant ΔK = 6 MPa√m in a UHV environment. A segment at each frequency was run at 23°C and -30°C and the subsequent crack growth rate was recorded for each segment and the reported value was plotted to determine the relative difference between the data points.
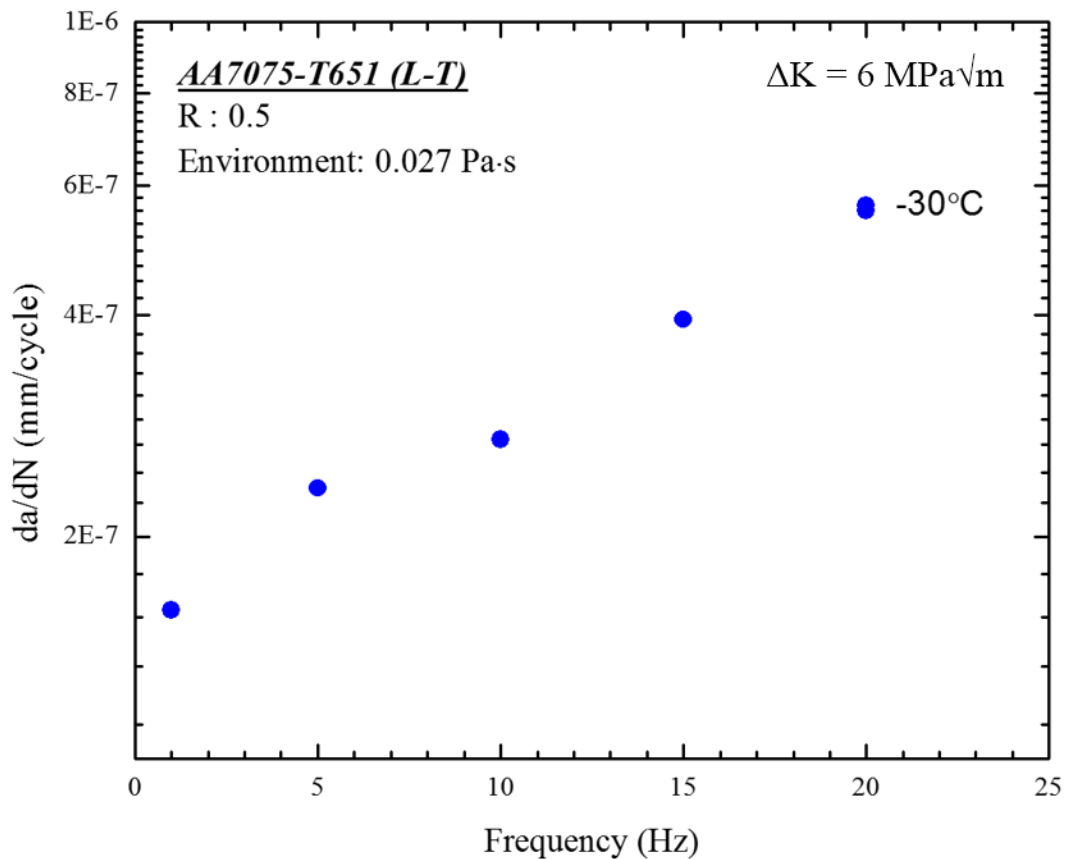
Figure 33 – A plot of the fatigue segments completed with a constant ΔK = 6 MPa$\sqrt{m}$ in a 0.027 Pa·s environment. A segment at each frequency was run at -30°C with the P_{H2O} adjusted accordingly to maintain the same P_{H2O}/f. The subsequent crack growth rate was recorded for each segment and the reported value was plotted to determine the relative difference between the data points.

6.3.2. Fatigue crack growth experiments (K-shed protocol)

Fatigue crack growth rates from experiments completed in a 0.027 Pa·s environment is shown in Figure 34 as a function of ΔK and temperature. The fatigue experiment completed at 23°C displayed a dip in the crack growth rate starting around 5.5 MPa$\sqrt{m}$ and a subsequent spike around 4 MPa$\sqrt{m}$ before resuming more typical behavior expected for fatigue finishing with a threshold value (ΔK_{th}) around 2 MPa$\sqrt{m}$. This atypical behavior has been previously discussed and termed the TTR.[5,51] The TTR behavior is postulated to be a product of an interaction of the

molecular transport of H_2O from the bulk environment to the crack tip with the evolving crack wake morphology roughness and crack front shape.[5,51] Generally, the fatigue experiment completed at -65°C displayed a systematic decrease in fatigue susceptibility with a slight decrease at high ΔK values (>8.5 MPa√m), but larger decreases in growth rates starting around 8.5 MPa√m and become more significant as the ΔK values fall into the near threshold regime. Additionally, a significant increase in the ΔK_{th} value was observed, which occurred at a ΔK value around 5 MPa√m. Fatigue crack growth rates from experiments completed in a UHV environment are shown in Figure 12 as a function of ΔK and temperature. The -65°C experiment ended early due to facilities-related challenges around a ΔK value of 6.59 MPa√m. Comparison between the two experiments demonstrates the crack growth rates begin to deviate at a ΔK value around 8 MPa√m and with the most significant differences being around a ΔK value of 7 MPa√m with the 23°C experiment reaching ΔK_{th} value just below 5 MPa√m.
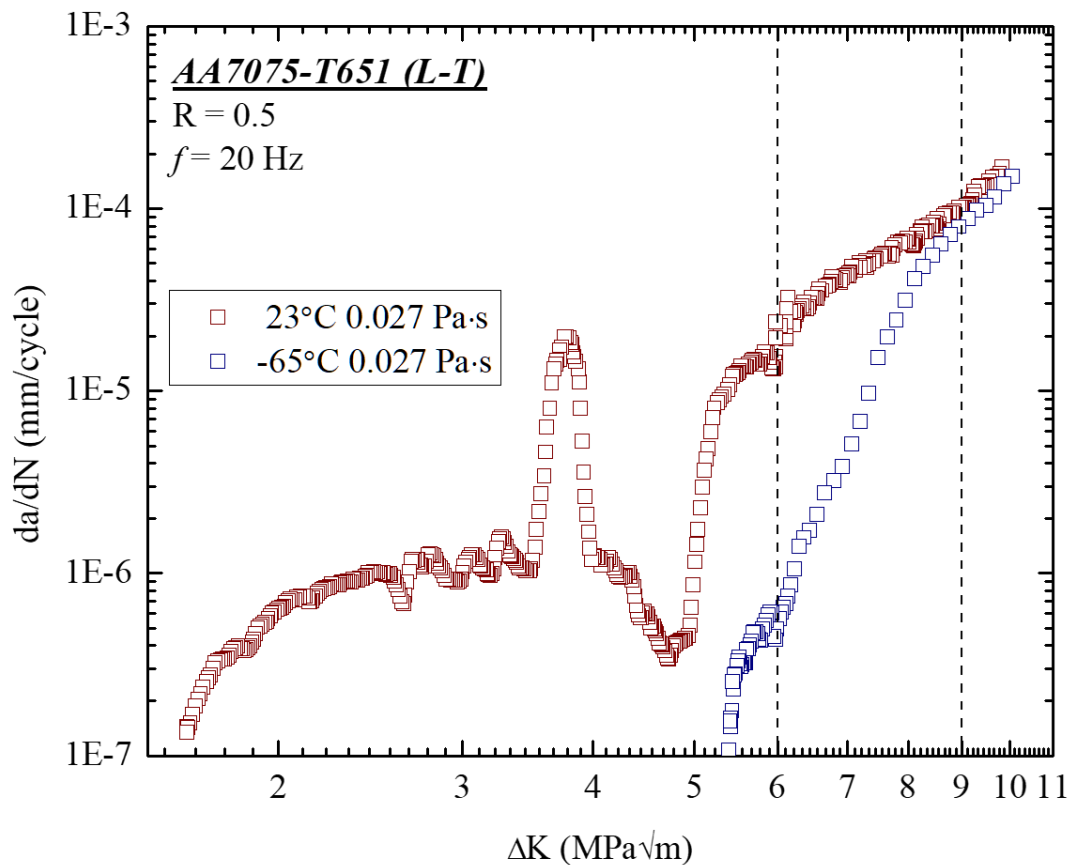
Figure 34 – A plot of the growth kinetics from the K-shed protocol in a 0.027 Pa·s environment. Dashed lines were included at a ΔK = 6 MPa√m and 9 MPa√m to indicated the crack growth rates at the locations which were further interrogated via the multi-scale characterization protocol.

6.3.3. Characterization of fatigue crack growth experiments (K-shed protocol)

Areas of the fatigue samples exposed to a ΔK of 6 MPa√m and 9 MPa√m were targeted for characterization as the ΔK of 6 MPa√m represented an area where significant differences were observed in the crack growth behavior and the ΔK of 9 MPa√m represented an area with little difference observed in crack growth behavior. When probing deformation structure proximate to the fracture surface is important to hold variable such as grain orientation constant. Previous work by Wert et al. in other material has shown different grain orientations developed different dislocation structure despite the same driving force being applied.[53] From the S-EBSD collected,

a [100] grain at the crack wake surface was selected for further interrogation. The [100] grains were selected because of the rolling texture found in AA7075 plate material making it the most likely orientation that would be found in all areas examined.[54] S-EBSD was collected for all K-shed protocol specimens at both a ΔK of 6 and 9 MPa$\sqrt{}$m and a specific {100} grain was selected for further interrogation. HR-EBSD performed on the targeted grain from the 23°C 0.027 Pa·s specimen at both a ΔK of 6 and 9 MPa$\sqrt{}$m as well as the -65°C 0.027 Pa·s specimen at a ΔK of 6 MPa$\sqrt{}$m can be seen in Figure 35. The HR-EBSD data was processed into GND density and show minimal to no difference between all the different data sets collected. BF-TEM images are shown in Figures 36, which provides a low magnification overview and Figure 37, which provides a higher magnification image of an area of interest best representing the nature of the sample. A major take away from the TEM images is the appearance of a clean layer about 500 nm deep, displaying significantly less dislocations and secondary particles as compared to the area greater than 500 nm deep. The severity of this layer increases with increasing driving force and exposure as the 0.027 Pa·s environment yielded a more prominent layer compared to the UHV environment. Additionally, temperature also has an impact on the layer, as at the higher temperature it appears more uniform in thickness and more globular at the low temperature. Figure 38 displays PED performed on the 23°C 0.027 Pa·s at both driving forces and the -65°C 0.027 Pa·s at 9 MPa$\sqrt{}$m samples. Holding the driving force constant, the data qualitatively indicates larger amounts of crystal misorientation occurring deeper into the subsurface with lower temperature, while an isothermal analysis indicates more misorientation at the higher driving force.

ΔK = 6 MPa√m   ΔK = 9 MPa√m

T = 23°C

T = -65°C
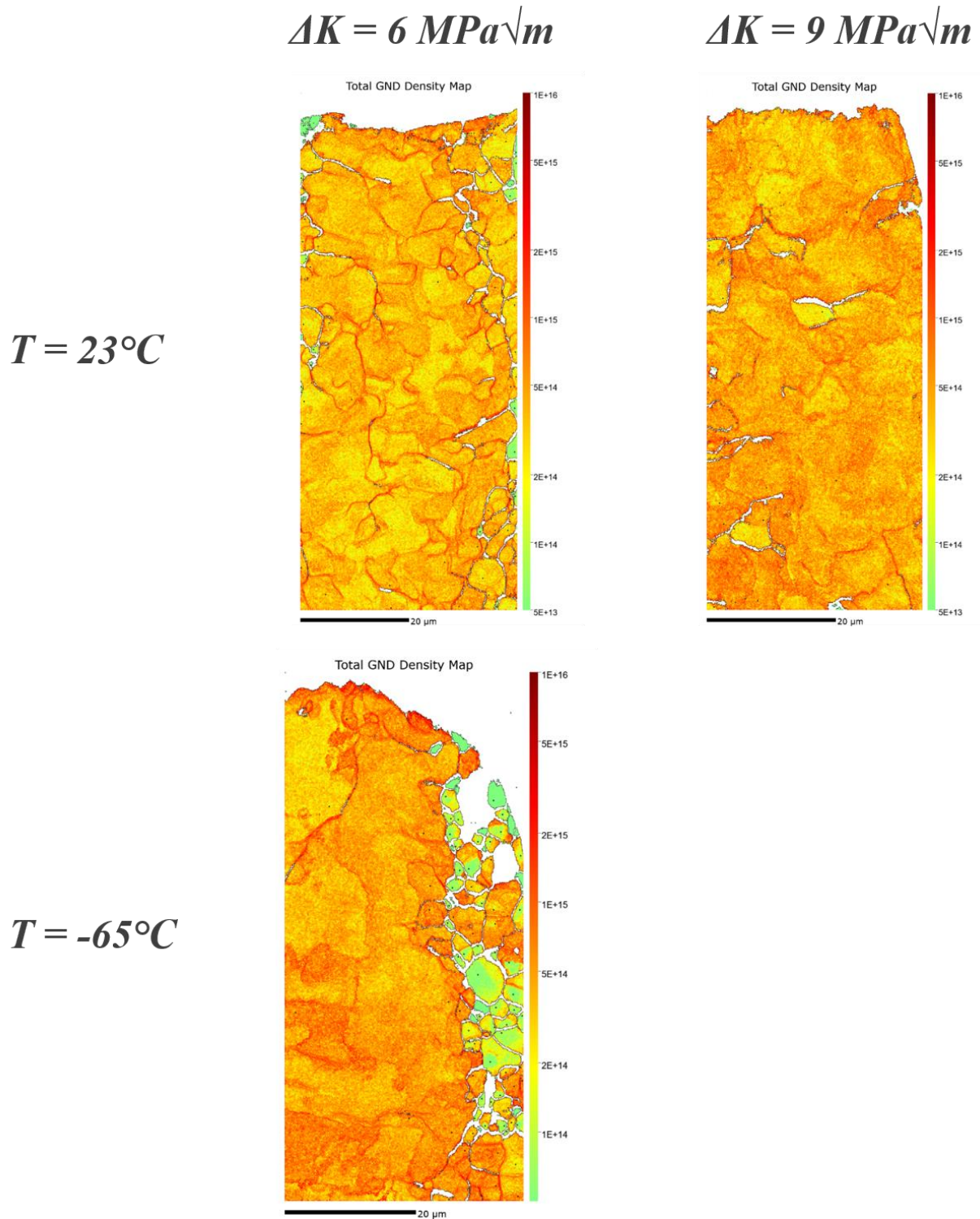
Figure 35 - GND density maps corresponding to the sub-surface crack wake regions exposed to a driving force of 6 or 9 MPa√m, a temperature of 23C or -65C, and a 0.027 Pa·s environment
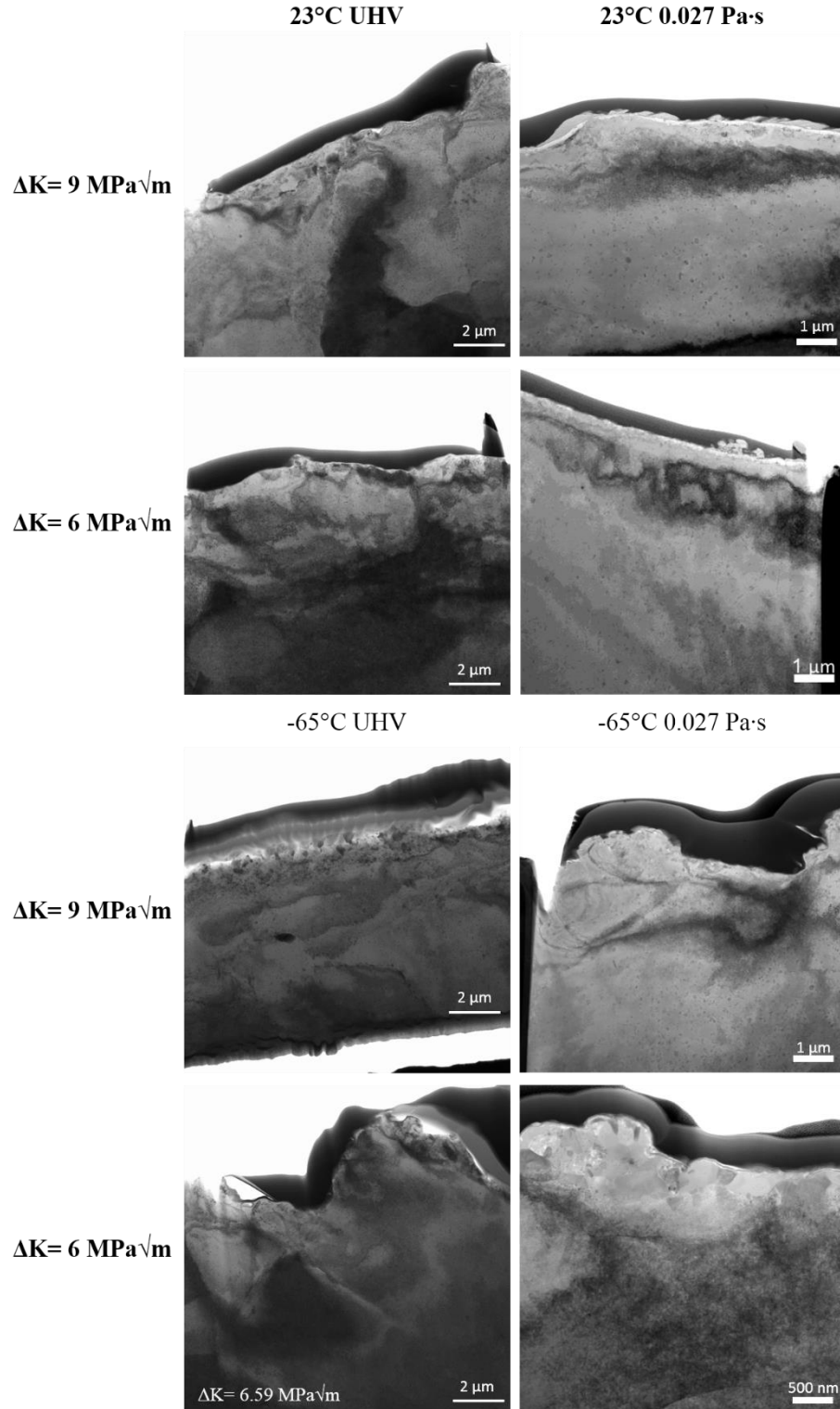
Figure 36 – TEM overview images of the sub-surface crack wake regions exposed to a driving force of 6 or 9 MPa√m, a temperature of 23C or -65C, and a 0.027 Pa·s or UHV environment.

23°C UHV **23°C 0.027 Pa·s**

ΔK= 9 MPa√m

ΔK= 6 MPa√m

-65°C UHV **-65°C 0.027 Pa·s**

ΔK= 9 MPa√m

ΔK= 6 MPa√m
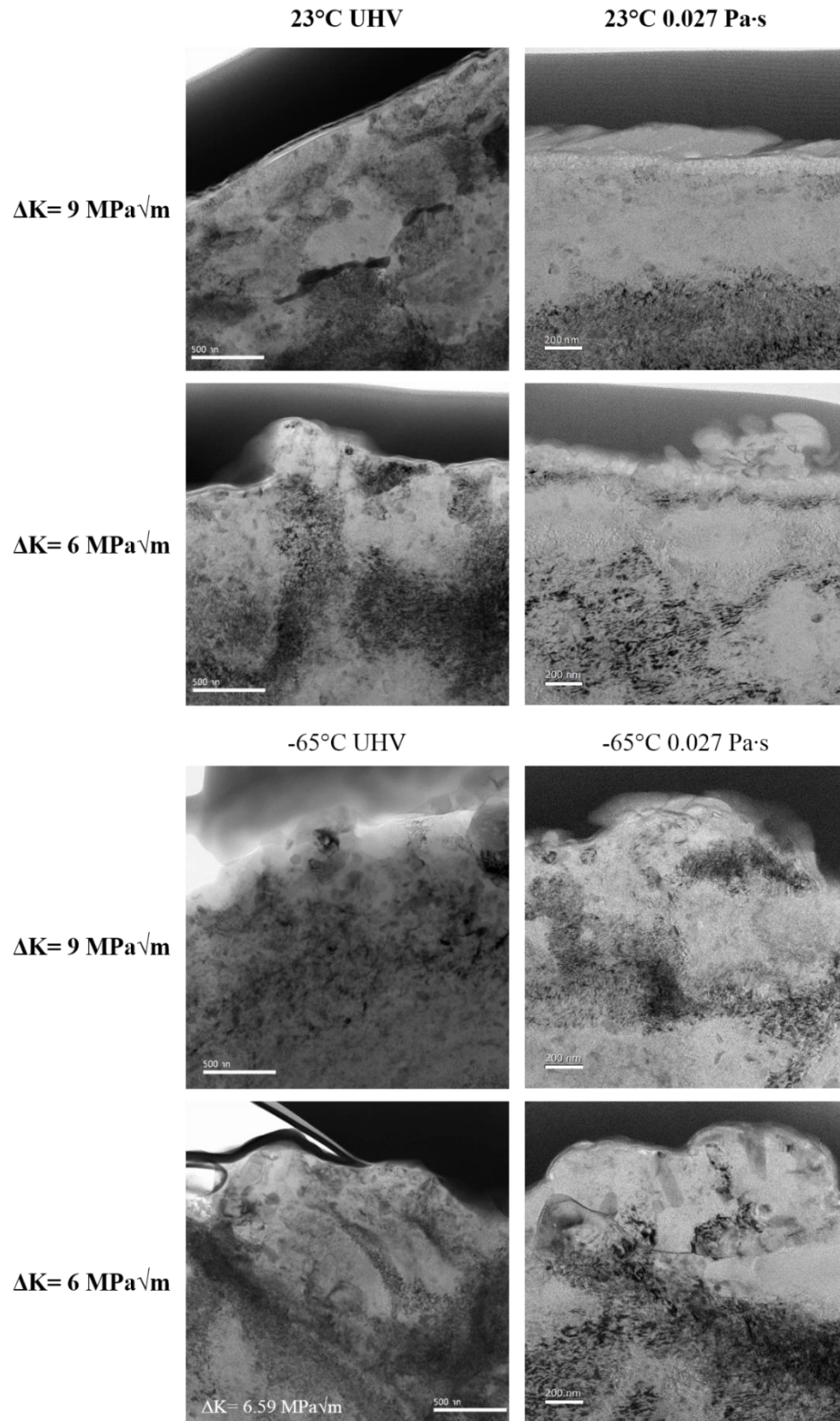
Figure 37 – TEM images of the sub-surface crack wake regions exposed to a driving force of 6 or 9 MPa√m, a temperature of 23C or -65C, and a 0.027 Pa·s or UHV environment.
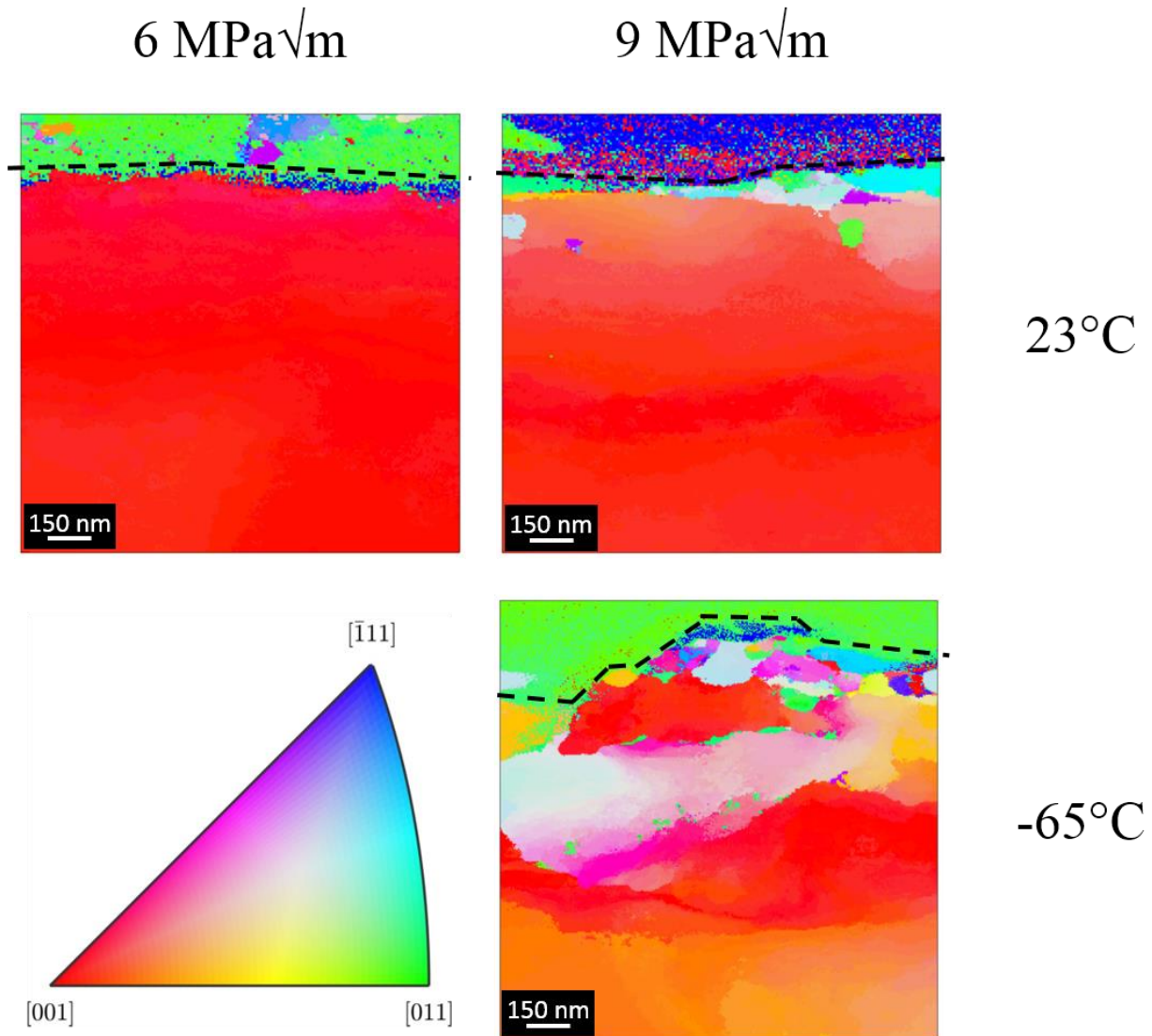
Figure 38 – PED images showing the amount of grain misorientation corresponding to the sub-surface crack wake regions exposed to a driving force of 6 or 9 MPa√m, a temperature of 23°C or -65°C, and a 0.027 Pa·s environment.

6.4. Discussion

The presented fatigue crack growth data as well as characterization of targeted areas of interest from specific fatigue experiments provided insights into the mechanisms responsible for the reduction of fatigue crack growth rates of AA7075-T651 at low temperatures. Specifically, this

study attempted to answer if the observed reduction in fatigue crack growth rates within high altitude environments is from a (1) Slower diffusion rate of atomic hydrogen within the aluminum alloy, (2) a temperature dependent evolution of the damage structure that is independent of the presence of hydrogen or lack thereof, or (3) a temperature dependent hydrogen-damage structure interaction. Based on these results, the following section will: (1) discuss the implications of the results of the constant ΔK loading protocol fatigue data specifically designed to provide insight into the impact of the slower diffusion rate of atomic hydrogen and (2) the implications of the results of the multi-scale characterization, specifically examining if observed changes in crack growth kinetics is accompanied by a different damage structure proximate to the crack wake surface. Differences in the damage structure could be used to postulate the mechanisms that would result in the observed changes in the local damage structure.

6.4.1. Implications of the fatigue crack growth experiments (Constant ΔK protocol)

The data for the crack growth rates is shown in Table 4 and was plotted in Figures 32 and 33. The main purpose of the constant ΔK experiments was to determine if slower diffusion rates of hydrogen at the lower temperatures was responsible for the observed slower crack growth rates of fatigue in high altitude environments. To determine this the frequency of the cyclic loading during fatigue is needed as a critical variable to decouple temperature dependent hydrogen diffusion and temperature dependent damage structure evolution. Beforehand, fatigue testing in a low temperature UHV environment was needed to determine if any frequency dependent fatigue behavior exists, especially given the strong temperature influence shown in chapter 3. Examination of the data shown in Figure 32 indicates an insignificant difference between the 1 Hz and 20 Hz segments in a -30°C UHV environment, with a calculated difference of 8.1E-7 mm/cycle. This is consistent with a study by Mayer et al., which examined frequency loading effects on the fatigue life of an aluminum alloy similar to AA7075 and found no statistically significant influence of cyclic frequency on the fatigue lifetimes at room temperature for both 100 Hz and 20 kHz experiments.[52] Although a direct comparison of the results are convoluted by the inclusion of the initiation period for fatigue life tests, it does however give credence to a lack of frequency dependence found in the current study. The lack of frequency dependence as shown in Figure 32 indicates at this driving force (6 MPa√m), temperature dependent dislocation behavior is not controlling the observed behavior changes due to high altitude environments. Therefore, at this

driving force frequency can be used as a decoupling variable to provide insights into temperature dependent hydrogen diffusion and temperature dependent hydrogen-damage structure evolution.

Figure 33 displays data of constant ΔK fatigue segments run in a -30°C 0.027 Pa·s environment using different frequencies ranging from 1 to 20 Hz. The trend observed in the data presented in Figure 33 shows an increasing crack growth rate correlating with an increase in frequency, which does not support slower H-diffusion as the governing factor of the damage process. Specifically, if temperature dependent hydrogen diffusion was the limiting factor, then the 1 Hz segment would be expected to have the fastest crack growth rate as there is an increased amount of time between the fatigue cycles enabling enhanced hydrogen diffusion to the front of the crack tip. Instead, the data conveys the opposite, thus highly unlikely temperature dependent hydrogen diffusion governs the observed differences in fatigue crack growth rates observed with high altitude environments. Since the P_{H2O} was adjusted accordingly with the change in frequency to maintain a constant P_{H2O}/f environment for all segments, a higher P_{H2O} was required at the higher frequency segments. As such, a possible explanation is the P_{H2O}/f parameter is not adequately capturing the severity of the environment at low temperatures. Over the frequency range used for this study the P_{H2O} was increased from 0.027 Pa at 1 Hz to 0.54 Pa at 20 Hz, thus the trend of increasing crack growth rate correlating with increasing P_{H2O} suggests the higher water vapor pressure is increasing the severity of the environment and is therefore responsible for the increase in crack growth rates. An additional explanation considered was the possibility of a significant change to the roughness of the crack wake surfaces created for each of the segments, which could hinder the water vapor molecules from reaching the center of the crack tip. However, further examination of the fracture surface of specimen 3 shown in Figure 39, qualitatively exhibits a similar roughness of the crack wake surface occurring with the 1 Hz segment and the 20 Hz segments. A detailed analysis of the implications and mechanisms governing this increase in growth rates with increasing frequency is outside the scope of this effort, but this finding does not compromise the observation that temperature dependent diffusion is not governing damage process.
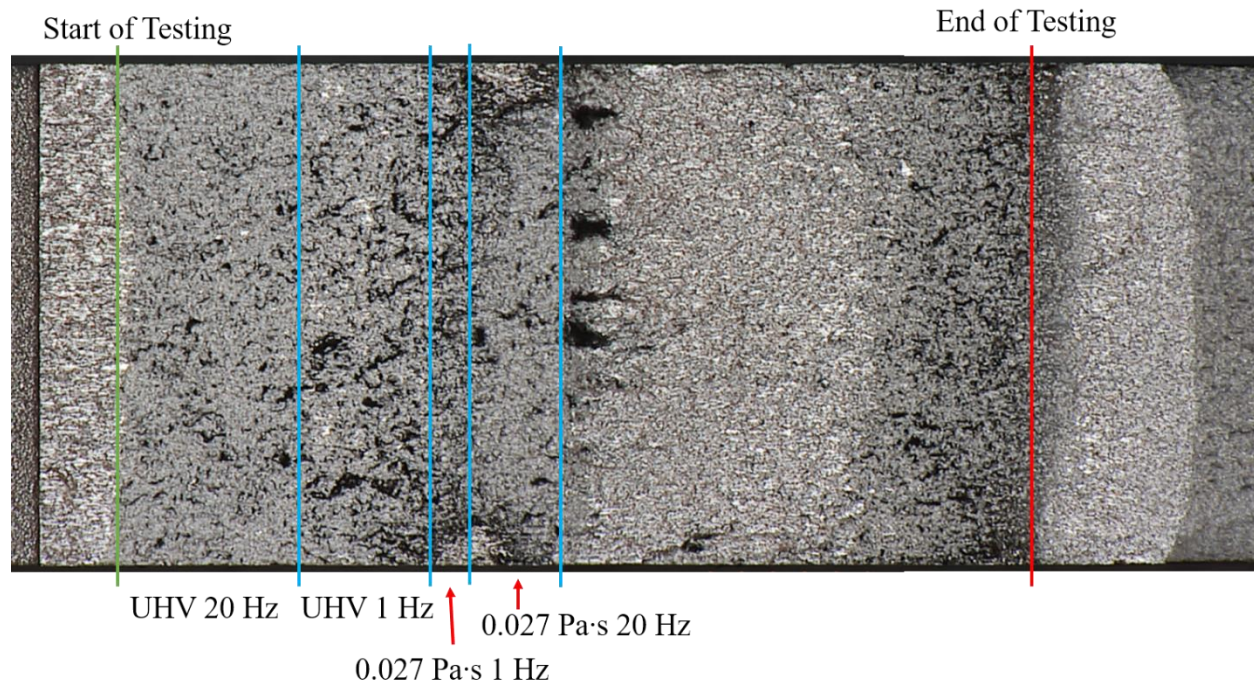
Figure 39 – A plot of the fatigue segments completed with a constant $\Delta K = 6$ MPa√m in a 0.027 Pa·s environment. A segment at each frequency was run at -30°C with the P_{H2O} adjusted accordingly to maintain the same P_{H2O}/f. The subsequent crack growth rate was recorded for each segment and the reported value was plotted to determine the relative difference between the data points.

6.4.2. Implications of the characterization of the fatigue crack growth experiments

The fatigue crack growth kinetic results from the K-shed protocols can be seen in Figures 12 and 34, which clearly demonstrates a strong impact from temperature on the fatigue process. Characterization of the deformation structure proximate to the fracture surface was focused at a $\Delta K = 9$ MPa√m, where behavior of all experiments appears to be independent of environment and a $\Delta K = 6$ MPa√m where behavior is significantly different among the different experiments, clearly influenced by the environment, particularly the low temperature.

HR-EBSD was performed on the target grains for both 23°C 0.027 Pa·s samples and the -65°C 0.027 Pa·s at a $\Delta K = 6$ MPa√m sample with the data output being in the form of geometrically necessary dislocations (GND) density maps. Examination of this data yielded two major findings; (1) the GND density maps show uniform GND density throughout the depth of the sample inside and out of the estimated cyclic plastic zone size making it impossible to discern fatigue deformation and residual deformation that existed previously in the material due to the rolling

process completed during the manufacturing of the plate. (2) The lack of discernable "hot spots" near the crack wake surface implies that the resolution of the HR-EBSD characterization technique is not sufficient enough to discern the deformation structure developed by the fatigue process from that created from the rolling process during the manufacturing of the AA7075-T651 plate. Further evidence of this exact finding was displayed in the TEM images taken from each of the samples characterized for this study shown in Figures 36 and 37. The images in Figure 36, show a unique area of deformation within the first 500 nm of the sample, which appears to be most prominent and severe with the 23°C 0.027 Pa·s environment. Higher magnification images seen in Figure 37, show a "layer" which formed in the first 500 nm in the sub-crack wake surface. Particularly, the 23°C UHV $\Delta K = 9$ MPa√m sample has a damage layer which appears similar to a damage structure known as Beilby layers, despite Beilby layers being a consequence of abrasion or a polishing processes caused by the combination of compression and shear forces on the surface.[55–57] The high shear strain associated with this damage process has been known to destroy fine precipitates and damage large ones, particularly the alloying elements of zinc and magnesium in precipitates dissolve into solid solution or form solute rich zones in the layer.[57] Albeit, the damage process of cyclic loading is different, it is conceivable that a highly localized intense shear strain could induce a similar reaction. Furthermore, as seen by only an addition of water vapor or more particularly hydrogen, the 23°C 0.027 Pa·s $\Delta K = 9$ MPa√m sample shown in Figure 37, suggests a dissolution of precipitates as well as the annihilation or recovery of the high density dislocation tangles occurring within this layer. Additionally, the first 100 nm have an appearance of an additional layer, which given the size and appearance could be nanocrystalline. In comparison, the images in the same figure of the 23°C UHV $\Delta K = 6$ MPa√m displays less similarity to Beilby layers, but this could be attributed to having less intense shear strain associated with being at a lower driving force. The TEM images of the 23°C 0.027 Pa·s $\Delta K = 6$ MPa√m sample in the same figure exhibits a similar layer around 500 nm thick devoid of precipitates, but has more areas of dislocation tangles present within the layer itself. However, the possibly nanocrystalline layer within the first 100 nm of the subsurface still appears at this lower driving force. PED performed on the 23°C samples shown in Figure 38, appears to confirm the existence of this smaller nanocrystalline layer as significant grain misorienation is observed and largely confined to this region further indicating the damage process is highly localized to the crack wake surface. Examination of the microstructure evolution near a fatigue crack tip, fatigued in an ambient environment has been

previously performed by Bai et al. on an under-aged AA2524 material, which observed a mixed process of dynamic recrystallization and strain-induced dissolution of Cu-Mg co-clusters attributed to the localization of plastic strain during cyclic loading.[58] Even though AA7075-T651 is a peak-aged material exhibiting a wavy slip nature, it has been claimed that additions of hydrogen in other materials ultimately manifest as an increased propensity for slip planarization.[23,59–63] TEM images of the -65°C UHV exhibit some similarity to the respective counterparts of the 23°C UHV, but the layer itself is less defined at the lower temperature insinuating some dependence of the damage structure evolution process on temperature independent of hydrogen contributions. This hindrance of the damage structure development at low temperature correlates with an observed cracking mechanism change occurring at higher driving forces with low temperatures as outlined in Chapter 3. Similarly, the -65°C 0.027 Pa·s samples show a defined layer around 500 nm thick, but at the lower temperature, the damage mechanism lacks the ability to clear most precipitates and dislocations tangles from the layer unlike the 23°C counterpart. Additionally, the layer's appearance is more globular with thick bulbous sections separated by thinner sections that are more reminiscent of observations made in the 23°C samples. This intermittent thickness of the layer could be an indication of how the damage structure changes with the loss of per cycle crack growth associated with these slower crack growth rates. PED performed on the -65°C 0.027 Pa·s $\Delta K = 9$ MPa√m and displayed in Figure 38, correlates with a more extensive region of strain associated with the cracking process than what was observed at the same driving force and environment at 23°C by significantly more grain misorientation being found deeper into the sample. Additionally, the possible nanocrystalline layer within the first 100 nm of the subsurface doesn't appear in the TEM images of the -65°C 0.027 Pa·s samples suggesting temperature is also inhibiting the damage structure evolution created with the addition of hydrogen. All of these observations suggests temperature is the dominating factor for fatigue behavior in high altitude environments of AA7075-T651.

6.5. Conclusions

The influence of high altitude environments on the fatigue behavior of AA7075-T651 was examined, specifically to develop a mechanistic understanding of the fatigue behavior responsible for the observed reduction in fatigue crack growth rates found with the combination of low temperatures and P_{H2O}. Proposed explanations of the observed behavior yielded questions that this

study sought to answer, which were; Is the observed further reduction in crack growth kinetics in high altitude environments from a (1) Slower surface reaction between the water molecules and aluminum needed to generate atomic hydrogen? (2) Significantly slower diffusion rate of atomic hydrogen within the aluminum alloy? (3) Temperature dependent evolution of the damage structure (independent of H)? (4) Temperature dependent hydrogen-damage structure interaction? Fatigue crack propagation experiments using a constant ΔK protocol at two different temperatures and environments and a decreasing ΔK protocol at two different target temperatures and environments suggested:

1. The temperature dependent diffusion rate of atomic hydrogen within AA7075-T651 does not appear to be the limiting factor responsible for the observed reduction in fatigue crack growth rates exhibited with high altitude environments.

2. Hydrogen appears to promote a recrystallization of the crack wake surface (about a 100 nm deep) and aids in the elimination of precipitates and dislocation tangles in the first 500 nm of the crack wake subsurface, which is more severe at higher temperature and driving forces.

3. The damage structure evolution occurring during the fatigue process in AA7075-T651 is strongly dependent on temperature independent of the presence of hydrogen.

4. The damage structure appears to be highly localized to the crack wake surface appearing similar to a damage structure known as Beilby layers.

5. The damage structure becomes more globalized and the Beilby layer type damage structure becomes less defined at lower temperatures.

6. The hydrogen-damage structure interaction also appears to be temperature dependent with the severity of the interaction lessening at the lower temperature.

6.6. Suggestions for future study

Generally, fatigue crack growth rates of aluminum in high exposure environments are believed to be affected by hydrogen embrittlement. As discussed in Chapter 1, exactly what the mechanisms are for hydrogen embrittlement in aluminum alloys are still debated as a number of mechanisms have been proposed, however further continuation could provide more valuable evidence to inform the mechanisms controlling hydrogen embrittlement in AA7075-T651. While the current work presented in this chapter suggests at least some aspect of the HELP mechanism

due to the presence of an enhanced and highly localized deformation layer within the first 500 nm of the subsurface as well as a possibly recrystallized layer within the first 100 nm of the surface. However, despite the lack of a recrystallized layer found within the samples fatigued in the UHV environment (no H), this evidence suggesting HELP is obfuscated by the fact that a similar highly localized, yet not as severe deformation layer was observed. Further examination similar to the one done in this chapter using a fatigue sample in a "high exposure" environment would provide clearer evidence as the crack growth rates reported in this chapter had indicated a clear enhancement over the intrinsic crack growth rates across a wide range of driving forces especially in the near-threshold regime. In addition, the performance of interrupted fatigue experiments stopped at the target driving force in combination with FIB to examine a distance in front of the crack the tip, near the crack tip as well as the crack wake would show the evolution of the fatigue damage before during and after the crack tip passes, thus providing further evidence to the cracking mechanisms in control of the hydrogen embrittlement process.

6.7. Acknowledgements

6.8. References

1.   Sanders, T. H. & Stanley, J. T. Review of Fatigue and Fracture Research on High-Strength Aluminum Alloys. *Am. Soc. Met.* 467–522 (1979).

2.   Chanani, G. R. *Fundamental Investigation of Fatigue Crack Growth Retardation in Aluminum Alloys*. (1976).

3.   Starke Jr., E. A. & Williams, J. C. Microstructure and the Fracture Mechanics of Fatigue Crack Propagation. in *Perspectives and Directions (20th Symposium)* (eds. Wei, R. P. & Gangloff, R. P.) 184–205 (American Society for Testing and Materials, 1989).

4.   Gangloff, R. P. Environment sensitive fatigue crack tip processes and propagation in

aerospace aluminum alloys. *Fatigue* **2**, 3401–3433 (2002).

5.   Burns, J. T. *et al.* Effect of water vapor pressure on fatigue crack growth in Al – Zn – Cu – Mg over wide-range stress intensity factor loading. *Eng. Fract. Mech.* **137**, 34–55 (2015).

6.   Bonakdar, A., Wang, F., Williams, J. J. & Chawla, N. Environmental Effects on Fatigue Crack Growth in 7075 Aluminum Alloy. *Metall. Mater. Trans. A* **43A**, 2799–2809 (2011).

7.   Wei, R. P. & Gao, M. Reconsideration of the Superposition Model for Environmentally Assisted Fatigue Crack Growth. *Scr. Metall.* **17**, 959–962 (1983).

8.   Pao, P. S., Gao, M. & Wei, R. P. Environmentally assisted fatigue-crack growth in 7075 and 7050 aluminum alloys. *Scr. Metall.* **19**, 265–270 (1985).

9.   Ruiz, J. & Elices, M. Effect of water vapour pressure and frequency on fatigue behaviour in 7017-t651 aluminium alloy plate. *Acta Mater.* **45**, 281–293 (1997).

10.   Gupta, V. K., Gangloff, R. P. & Agnew, S. R. Diffraction characterization of microstructure scale fatigue crack growth in a modern Al-Zn-Mg-Cu alloy. *Int. J. Fatigue* **42**, 131–146 (2012).

11.   Truckner, W. G., Staley, J. T., Bucci, R. J. & Thakker, A. B. *Effect of Microstructure on Fatigue Crack Growth of High-Strength Aluminum Alloys*. (1976).

12.   Lynch, S. P. Mechanisms of Fatigue and Environmentally Assisted Fatigue. *ASTM Int.* **675**, 174–213 (1979).

13.   Nix, K. J. & Flower, H. M. The micromechanisms of fatigue crack growth in a commercial Al-Zn-Mg-Cu alloy. *Acta Metall.* **30**, 1549–1559 (1982).

14.   Burns, J. T. *et al.* Effect of water vapor pressure on fatigue crack growth in Al-Zn-Cu-Mg over wide-range stress intensity factor loading. *Eng. Fract. Mech.* **137**, 34–55 (2014).

15.   Davidson, D. . & Lankford, J. The Effects of Aluminum Alloy Microstructure on Fatigue Crack Growth. *Mater. Sci. Eng.* **74**, 189–199 (1985).

16.   Ro, Y., Agnew, S. R. & Gangloff, R. P. Effect of environment on fatigue crack wake dislocation structure in Al-Cu-Mg. *Metall. Mater. Trans. A Phys. Metall. Mater. Sci.* **43**, 2275–2292 (2012).

17.   Piascik, R. S. & Gangloff, R. . Environmental fatigue of an Al-Li-Cu alloy: part I. Intrinsic crack propagation kinetics in hydrogenous environments. *Metall. Trans. A* **22**, 2415–2428 (1991).

18.   Gingell, A. D. B. & King, J. E. The effect of Frequency and Microstructure on Corrosion Fatigue Crack Propagation in High Strength Aluminum Alloys. *Acta Metall.* **45**, 3855–3870 (1996).

19.   Gangloff, R. P. *Corrosion fatigue crack propagation in metals*. (1990).

20.   Davidson, D. L. & Lankford, J. The Effects of Water Vapor on Fatigue Crack Tip Mechanics in 7075-T651 Aluminum Alloy. *Fatigue Fract. Eng. Mater. Struct.* **6**, 241–256 (1983).

21.   Ro, Y. J., Agnew, S. R., Bray, G. H. & Gangloff, R. P. Environment-exposure-dependent fatigue crack growth kinetics for Al-Cu-Mg/Li. *Mater. Sci. Eng. A* **468–470**, 88–97 (2007).

22.   Young Jr., G. A. & Scully, J. R. The Effects of Test Temperature, Temper, and Alloyed Copper on the Hydrogen-Controlled Crack Growth Rate of an Al-Zn-Mg-(Cu) Alloy. *Metall. Mater. Trans. A* **33A**, 1167–1181 (2002).

23.   Lynch, S. Hydrogen embrittlement phenomena and mechanisms. *Corros. Rev.* **30**, 105–123 (2012).

24.   Adminstration, N. O. and A. A. (NOAA), (NASA), N. A. and S. A. & (USAF), U. S. A. F. *U.S. Standard Atmosphere, 1976*. (1976).

25.   Burns, J. T., Jones, J. J., Thompson, A. W. & Locke, J. S. (Warner). Fatigue crack propagation of aerospace aluminum alloy 7075-T651 in high altitude environments. *Int. J. Fatigue* **106**, 196–207 (2018).

26.   Burns, J. T., Gupta, V. K., Agnew, S. R. & Gangloff, R. P. Effect of low temperature on fatigue crack formation and microstructure-scale propagation in legacy and modern Al-Zn-Mg-Cu alloys. *Int. J. Fatigue* **55**, 268–275 (2013).

27.   Cox, J. M., Pettit, D. E. & Langenbeck, S. L. Effect of Temperature on the Fatigue and Fracture Properties of 7475-T761 Aluminum. *ASTM Spec. Tech. Publ.* 241–256 (1985) doi:10.1520/stp32759s.

28. Moreto, J. *et al.* Environmentally-assisted Fatigue Crack Growth in AA7050-T73511 Al Alloy and AA2050-T84 Al-Cu-Li Alloy. *Mater. Res.* **18**, (2015).

29. Magda, D. J. Effect of Low Temperatures and Anisotropy on Fatigue Crack Behavior of Aluminum Alloys. (University of Utah, 1995).

30. Liu, M. D., Xiong, J. J., Liu, J. Z. & Tian, B. J. Modified model for evaluating fatigue behaviors and lifetimes of notched aluminum-alloys at temperatures of 25 °C and −70 °C. *Int. J. Fatigue* **93**, 122–132 (2016).

31. Liu, M. D. & Xiong, J. J. Fatigue crack growth testing and evaluation for aluminum alloys at temperatures of 25°C and −70°C. *J. Test. Eval.* **46**, 1698–1707 (2017).

32. Pettit, D. E. & van Orden, J. M. Evaluation of Temperature Effects on Crack Growth in Aluminum Sheet Material. *ASTM Spec. Tech. Publ.* 106–124 (1979) doi:10.1520/stp34909s.

33. Abelkis, P. R., Harmon, M. B., Hayman, E. L., Mackay, T. L. & Orlando, J. Low Temperature and Loading Frequency Effects on Crack Growth and Fracture Toughness of 2024 and 7475 Aluminum. *ASTM Spec. Tech. Publ.* 257–273 (1985) doi:10.1520/stp32760s.

34. Burns, J. T., Gupta, V. K., Agnew, S. R. & Gangloff, R. P. Effect of low temperature on fatigue crack formation and microstructure-scale propagation in legacy and modern Al–Zn–Mg–Cu alloys. *Int. J. Fatigue* **55**, 268–275 (2013).

35. Shlyannikov, V. N., Yarullin, R. R. & Ishtyryakov, I. S. Effect of temperature on the growth of fatigue surface cracks in aluminum alloys. *Theor. Appl. Fract. Mech.* **96**, 758–767 (2018).

36. Basinski, Z. S., Korbel, A. S. & Basinski, S. J. The Temperature Dependence of the Saturation Stress and Dislocation Substructure in Fatigued Copper Single Crystals. *Acta Metall.* **28**, 191–207 (1980).

37. Liaw, P. K., Fine, M. E., Kiritani, M. & Ono, S. The Effect of Temperature on the Fatigue Crack Propagation Rate in Aluminum. *Scr. Metall.* **11**, 1151–1155 (1977).

38. Burns, J. T., Jones, J. J., Thompson, A. W. & Warner-Locke, J. S. Fatigue crack propagation

of aerospace aluminum alloy 7075-T651 in high altitude environments. *Int. J. Fatigue* **106**, 196–207 (2018).

39. Meng, X., Lin, Z. & Wang, F. Investigation on corrosion fatigue crack growth rate in 7075 aluminum alloy. *Mater. Des.* **51**, 683–687 (2013).

40. Feltner, C. E. Dislocation arrangements in aluminum deformed by repeated tensile stresses. *Acta Metall.* **11**, 817–828 (1963).

41. Papazian, J. *et al.* DARPA/NCG structural integrity prognosis system. *DARPA* **HR0011-04**, (2009).

42. B209-14 Standard Specification for Aluminum and Aluminum-Alloy Sheet and Plate. *ASTM Int.* (2014) doi:https://doi.org/10.1520/B0209-14.

43. Burns, J. T., Larsen, J. M. & Gangloff, R. P. Driving forces for localized corrosion-to-fatigue crack transition in Al-Zn-Mg-Cu. *Fatigue Fract. Eng. Mater. Struct.* **34**, 745–773 (2011).

44. Payne, J., Welsh, G., Christ, R. J., Nardiello, J. & Papazian, J. M. Observations of fatigue crack initiation in 7075-T651. *Int. J. Fatigue* (2010) doi:10.1016/j.ijfatigue.2009.06.003.

45. E647-15e1. Standard Test Method for Measurement of Fatigue Crack Growth Rates. *ASTM B. Stand.* 1–49 (2016) doi:10.1520/E0647-15E01.2.

46. Donald, J. K. Introducing the compliance ratio concept for determining effective stress intensity. *Int. J. Fatigue* **19**, 191–195 (1997).

47. Donald, J. K., Bray, G. H. & Ralph, W. an Evaluation of the Adjusted Compliance Ratio Technique. 674–695 (1999).

48. Burns, J. T. & Gangloff, R. P. Effect of loading environment on fatigue crack formation and microstructurally small fatigue propagation in Al-Zn-Mg-Cu. *Metall. Mater. Trans. A* **44**, 2083–2105 (2012).

49. Harris, Z. D., Thompson, A. W. & Burns, J. T. Multiscale Assessment of Deformation Induced by Hydrogen Environment-Assisted Cracking in a Peak-Aged Ni-Cu Superalloy. *JOM* **72**, 1993–2002 (2020).

50. Thompson, A. W., Harris, Z. D. & Burns, J. T. Examination of focused ion beam-induced

damage during platinum deposition in the near-surface region of an aerospace aluminum alloy. *Micron* **118**, 43–49 (2019).

51. Jones, J. W. The effect of water vapor pressure in the fatigue crack propagation rates in aerospace aluminum alloys 7075-T651 and 2199-T86. (University of Virginia, 2015).

52. Mayer, H., Papakyriacou, M., R., P. & Stanzl-Tschegg, S. Influence of loading frequency on the high cycle fatigue properties of AlZnMgCu1.5 Aluminum alloy. *Mater. Sci. Eng. A* **314**, 48–54 (2001).

53. Wert, J. A., Huang, X., Winther, G., Pantleon, W. & Poulsen, H. F. Revealing deformation microstructures A variety of features broadly classed as deformation microstructure. *Mater. Today* **10**, 24–32 (2007).

54. Turkmen, H. S., Loge, R. E., Dawson, P. R. & Miller, M. P. On the mechanical behaviour of AA 7075-T6 during cyclic loading. *Int. J. Fatigue* **25**, 267–281 (2003).

55. Wang, S. S., Huber, D., Poplawsky, J. D., Colijn, H. & Frankel, G. S. The subsurface structure of abraded Al–Zn–Mg–Cu alloy. *Materialia* **16**, 101065 (2021).

56. Wang, S. S. *et al.* Accelerated precipitation and growth of phases in an Al-Zn-Mg-Cu alloy processed by surface abrasion. *Acta Mater.* **131**, 233–245 (2017).

57. Zhao, Z. & Frankel, G. S. On the first breakdown in AA7075-T6. *Corros. Sci.* **49**, 3064–3088 (2007).

58. Bai, S., Liu, Z., Zhou, X., Gu, Y. & Yu, D. Strain-induced dissolution of Cu-Mg co-clusters and dynamic recrystallization near a fatigue crack tip of an underaged Al-Cu-Mg alloy during cyclic loading at ambient temperature. *Scr. Mater.* **64**, 1133–1136 (2011).

59. Robertson, I. M. *et al.* Hydrogen Embrittlement Understood. *Metall. Mater. Trans. B* (2015) doi:10.1007/s11663-015-0325-y.

60. Ferreira, P. J., Robertson, I. M. & Birnbaum, H. K. Hydrogen effects on the character of dislocaitons in high-purity aluminum. *Acta Mater.* **47**, 2991–2998 (1999).

61. Wen, M., Fukuyama, S. & Yokogawa, K. Hydrogen-affected cross-slip process in fcc nickel. *Phys. Rev. B* **69**, (2004).

62. Robertson, I. M. The effect of hydrogen on dislocation dynamics. *Eng. Fract. Mech.* **68**,

671–692 (2001).

63.   Delafosse, D. Hydrogen effects on the plasticity of face centered cubic (fcc) crystals. in *Gaseous Hydrogen Embrittlement of Materials in Energy Technologies* 247–285 (2012). doi:https://doi.org/10.1533/9780857095374.2.247

Chapter 7 – Final Conclusions

The results of this dissertation indicate low temperatures found in high altitude environments have a strong influence on the fatigue behavior. Absent of other environmental influences, the decline in temperature lead to a precipitous decline in da/dN, which saturated around -50°C. Particularly, this decline in da/dN correlated with a transition in the cracking mechanism exhibited by the material between a flat transgranular cracking mechanism and a slip band cracking mechanism. The trend of decreasing temperature caused this transition in mechanism to occur at higher driving forces, with temperature influences on this transition appearing to lessen below -30°C. Evaluation of the subsurface damage structure using the developed multi-length scale characterization protocol, demonstrated the majority of damage structure caused by fatigue in this alloy was localized to the first ≈ 500 nm of depth, appearing similar in appearance only to Beilby layers, with low temperature as well as low driving force lessening the definition of this layer. When both main components of a high altitude environment were considered (low temperature and low water vapor pressure) the strong influence of low temperature was still prominent.

First, with fatigue cracking of AA7075-T651 in low water environments at 23°C a phenomenon known as TTR occurs with the application of intermediate driving forces. This TTR event was determined to be an intrinsic response of the material, which cannot be eliminated by a reduction of sample thickness or a change in the loading protocol from the traditional K-shed type to a K-rise type. Evaluation of the subsurface using the same multi-length scale characterization protocol exhibited additional damage features correlating with the presence of hydrogen, such as the clearing of precipitates and high density dislocation areas within the first ≈ 500 nm of depth and a potentially recrystallized layer appearing within the first ≈ 100 nm of depth. With the addition of low temperature, the impact from low levels of water vapor on the fatigue behavior was lessened, insinuating low water vapor levels may not need to be taken into consideration for

aerospace applications in high altitude environments. Further evidence of this was observed with the use of the multi-length scale characterization protocol, which revealed the prohibition of the main damage features correlating with the presence of hydrogen. Furthermore, fatigue experiments designed to decouple temperature dependent damage structure evolution from temperature dependent hydrogen diffusion limitations clearly demonstrated the fatigue behavior observed in low temperature environments was not controlled by diffusion limitations, furthering the likelihood of low temperature being the controlling factor of this observed behavior.

Appendix A – Examination of focused ion beam-induced damage during platinum deposition in the near- surface region of an aerospace aluminum alloy

Thompson, A. W., Harris, Z. D. & Burns, J. T. Examination of focused ion beam-induced damage during platinum deposition in the near-surface region of an aerospace aluminum alloy. *Micron* 118, (2019).

Appendix B – Multiscale assessment of deformation induced by hydrogen environment-assisted cracking in a peak-aged Ni-Cu superalloy

Harris, Z. D., Thompson, A. W. & Burns, J. T. Multiscale Assessment of Deformation Induced by Hydrogen Environment-Assisted Cracking in a Peak-Aged Ni-Cu Superalloy. *JOM* (2020). doi:10.1007/s11837-020-04107-6